ISSN number 0971 - 9709

The Journal of Indian Geophysical Union

AN OPEN ACCESS BIMONTHLY JOURNAL OF IGU

VOLUME 28, ISSUE 2, MARCH 2024

EDITORIAL OFFICE

Indian Geophysical Union, NGRI Campus, Uppal Road, Hyderabad- 500 007
Telephone: 91-4027012739, 27012332; Telefax:+91-04-27171564
Email: jigu1963@gmail.com, website: http://iguonline.in/journal/

The Journal with six issues in a year publishes articles covering
Solid Earth Geosciences; Marine Geosciences; and Atmospheric, Space and Planetary Sciences.
The Journal is Financially supported by MoES, Govt. of India.

Annual Subscription

Individual Rs -1000/- per issue and Institutional Rs- 5000/- for six issues
Payments should be sent by DD drawn in favour of "The Treasurer, Indian Geophysical Union", payable at Hyderabad,
Money Transfer/NEFT/RTGS (Inter-Bank Transfer), Treasurer, Indian Geophysical Union, State Bank of India, Habsiguda Branch,
Habsiguda, Uppal Road, Hyderabad- 500 007
A/C: 52191021424, IFSC Code: SBIN0020087, MICR Code: 500002318, SWIFT Code: SBININBBHO9.
For correspondence, please contact, Hon. Secretary, Indian Geophysical Union, NGRI Campus, Uppal Road,
Hyderabad - 500 007, India; Email: igu123@gmail.com; Ph: 040 27012332

ISSN: 0257-7968 (Clarivate Analytics)
ISSN: 0971-9709 (NISCAIR)
Approved as bimonthly ESCI journal by Clarivate Analytics
Cited in Indian Citation Index (ICI), New Delhi
Evaluated by NISCAIR, New Delhi
UGC Approved Journal

CONTENTS

Research Articles

Obituary

J. Ind. Geophys. Union, 28(2) (2024), 84-98

Modification of radiogenic heat production equation due to radioactive disequilibrium in rock samples from Gamma-Ray spectrometry

Olusegun O. Alabi[1*], Samuel O. Sedara[2], Deborah T. Ajah[1] and Iwa A. Akanni[1]
[1]Physics Department, Osun State University, Osogbo, Osun State, Nigeria
[2]Physics and Electronics Department, Adekunle Ajasin University, Akungba-Akoko, Ondo State, Nigeria
Corresponding author: olusegun.alabi@uniosun.edu.ng

ABSTRACT

Accurate Radioactive Heat Production (RHP) estimation is essential for determining geothermal potential and exploration. However, a mass defect due to Uranium Series Decay (USD) is a serious problem that has yet to be considered by previous RHP models in computing accurate RHP. The RHP is a petro-physical property that quantifies the heat generated by the decay of radioactive isotopes within rocks. However, there is a mass defect in the process due to series disequilibrium in U decay called Uranium Series Decay (USD) that affects the accurate estimation of the RHP, which was not considered by the two previous RHP models, established by Birch and Rybach in 1954 and 1976 respectively. This work aims to determine the performance level of the previous RHP models and consider the effect of USD on establishing an improved new RHP model with a better performance level for accurate estimation of RHP.

A revised data from gamma-ray spectrometry was used to compute the Beta and Alpha energies ($E_{\beta max}$) of decay schemes, mass defect ($E_{\Delta m}$) of radioelements, total absorbed energy (E_{abs}) per atom, numerical constants (B_i) and converted to the accepted RHP unit (μWm^{-3}) for each radionuclide. The modified RHP model (A_3) was evaluated and validated using error metrics like the Sum of Squared Error (SSE), Mean Absolute Error (MAE), Coefficient of Determination (R^2), and Root Mean Squared Error (RMSE) and radiometric data from seven different regions of Nigeria (Southwest-SW, Southeast-SE, Southsouth-SS, Northwest-NW, Northeast-NE, Northcentral-NC) and India. The performance of the improved model (A_3) was compared with Birch's (A_1) and Rybach's (A_2) RHP models.

The A_3 RHP model obtained was $RHP(\mu Wm^{-3}) = \rho(0.103C_U + 0.029C_{Th} + 0.061C_K)$, where C_U, C_{Th} and C_K are the concentration of U, Th and K in part per million (ppm) and ρ is the density of the rock sample(kgm^{-3}). It was observed that the A_1, A_2, and A_3 models have 47.8, 45.2, and 54.6 percent performance levels, respectively, which indicates that the A_3 model has better performance value than the A_1 and A_2 models. A_3 also returned a lower measure of errors in SSE, MAE, and RMSE than the A_1 and A_2 models in all the regions considered and this showed that the A_3 model performed better in the metrics analysis for all the regions.

The performance level of the existing models, used to estimate RHP by researchers in the geosciences was determined and a more accurate model with better performance was obtained by considering mass defect due to Uranium Series Decay (USD) in the RHP estimation using data from Nigeria and outside Nigeria.

Keywords: Radiogenic Heat Production, Uranium disequilibrium effect, Geological formation, Gamma-ray spectrometry, Performance metrics, Birch and Rybach heat production models

INTRODUCTION

Radioactive heat production (RHP) is a petro-physical property which quantifies the quantity of heat produced by the decay of radioactive isotopes within the rocks and minerals (Asfahani, 2018). It can be expressed in μWm^{-3} and depends on the amounts of radioelements of interest, which are potassium (K), uranium (U) and thorium (Th) contained in rocks and are relevant to internal terrestrial heat sources since they add to the heat created during the process of radioactive decay in rocks, which also reflects the geochemical conditions during rock formation (Asfahani, 2018; Fall et al., 2018). The space-time distribution of radionuclide has a large influence on the Earth's internal temperature field, and sometimes 30 to 40% of the ground heat flow density is generated by radionuclide. RHP is an important parameter for detailing the geothermal history of different geotectonic locations (Tabod et al., 1992; Valković, 2019). The origin of the heat sources differs for each region, and high heat flow regions show different heat transfer modes (Plomerova et al., 1993).

Birch (1954) formulated an empirical formula to calculate the RHP in rocks, which is generally conventional and widely used in many research works, and the equation is written as:

$$A_1(\mu Wm^{-3}) = \rho(0.097C_U + 0.035C_K + 0.026C_{Th}) \quad (1)$$

Rybach (1976) observed that since 1954, some factors like decay patterns, half-lives and mass alterations and differences had been reviewed based on data from the works of Hyde et al. (1964) and Brunee and Voshage (1964) which called for the review of the constants of the heat production after twenty two years of existence of the Birch's equation. The Birch formula was revised by Rybach (1976) who proposed the new expression as:

$$A_2(\mu Wm^{-3}) = \rho(0.0952C_U + 0.0348C_K + 0.0256C_{Th}) \quad (2)$$

where: ρ = dry density of rock (kg/m^3), C_K, C_U, C_{Th} = concentrations of K in %, uranium and thorium in ppm respectively. Rybach determined the decay energy $E_{\Delta m}$ from the mass changes of uranium and thorium from the initial radioisotopes and stable end products by considering the quantity of radiated α-particles (He^4).

Table 1. Radionuclide parameters based on data from Kocher (1980), Grupen (2010) and Clauser (2020).

Isotope	Mass balance	This work		f	Mass (u)	$T_{1/2}$ (yrs)
		$\sum E_{\beta max}$	$\sum E_{\alpha max}$			
U238	$m(U^{238}) - 8m(He^4) - m(Pb^{206})$	0.00	4.1940	0.992742	238.05678826	$4.5x10^9$
U235	$m(U^{238}) - 8m(He^4) - m(Pb^{206})$	0.00	4.3784	0.007204	235.043928	$7.04x10^8$
Th232	$m(U^{238}) - 8m(He^4) - m(Pb^{206})$	0.00	4.0045	0.9998	232.03805	$14x10^9$
K40	$m(K^{40}) - m(Ar^{40})$	0.4543	0.00	0.000177	39.0983	$1.25x10^9$

The decay energies and parameters for the radionuclide were used to derive the RHP constants from the data of Hyde et al. (1964) and Brunee and Voshage (1964), as shown in Table 1.

Limitations and uncertainties in the Birch's and Rybach's RHP equations

Many factors have been observed in the literature that affect the outcome of the estimation of RHP in rocks, which include geographical, atmospheric, spatial distribution, mass defects, and series disequilibrium effects. To tackle such incorrectness exemplifies a research area for supplementary progress and study. The above mentioned factors can thwart gamma-ray data collection from the field. It can also give an inaccurate calculation of RHP and this can result to radionuclide concentration which does not characterize the RHP that is being created by the rock (Dickson and Scott, 1997; McCay et al., 2014). Of particular interest in all these factors that affect the outcome of the estimation and accuracy of RHP in rocks, is the uranium series disequilibrium (USD) effect. This particular series decay disequilibrium effect always result in concentrations of radionuclides which does not reflect RHP generated by the rock (Sherman et al., 2007; McCay et al., 2014). The disequilibrium effects have always been known to occur during gamma-ray spectrometry, but not much of it has been quantitatively justified in many scientific research and studies (McCay et al., 2014; Manning et al., 2007). Gamma-rays can be applied to get the concentrations of radionuclide (K, U, Th) in rocks and these gamma-rays are not really liable for substantial amounts of the heat created. The method can be applied to evaluate concentrations of radionuclide in many geothermal fields and excavation sites (Faruwa et al., 2020; Cinelli et al., 2020). It can also be used to decide the nature and uranium migration (UM) rate in many crustal formations (Youssef et al., 2017; Pereira and Ferreira, 2018; Reis et al., 2020) especially RHP in crustal establishments that are related with heat-producing elements (RHPEs) which are radioactive (Hasterok and Webb, 2017; Clauser, 2020; Akingboye et al., 2021; Liao et al., 2023). It has an extensive collection of applications outside geothermal investigation, which include uranium probing (Yuan et al., 2023), sedimentary surface identification for exploration of oil and gas, radioactive pollution discovery (Cinar et al., 2017), mineral probing (Chandrasekaran et al., 2014), pure earth science discoveries (Ray et al., 2008; Sims et al., 2021), fracture and fissure unearthing linked with uranium concentrations elevation, which is caused by uranium movement in fluid in the subsurface (Grozeva et al., 2022) that can cause substantial problem for gamma-ray spectrometry investigation and explanation known as disequilibrium (Cai et al., 2015; Lefebvre et al., 2022; Grozeva et al., 2022). There are daughter product isotopes in the natural decay series which likewise have appropriately long half-lives that it is likely their equilibrium relationship (ratio) to their parent (initial) isotope can be altered by chemical and physical processes in nature (El Afandy et al., 2018). The leftover elements (isotopes) have very short half-lives and are continuously in radioactive equilibrium with their parent isotopes, but there is one exclusion, which is the ^{222}Rn with a very short half-life of 0.38x10 days which can escape from rocks due to its distinct feature being a gas (Nada and Aly, 2013).

Radioactive series disequilibrium

Over the years, radioactive disequilibrium in rocks has presented a difficult problem to geoscientists. The magnitude and frequency of disequilibria have been generally underestimated and the significance of disequilibrium in field and laboratory measurements has begun to be realized and few studies about disequilibrium in radioactive deposits have been published. Several radioactive materials or samples display radioactive disequilibrium for the reason that many geochemical practices affect their ore deposits (Ju et al., 2022; Veerasamy et al., 2023).

Uranium-series disequilibria can be classified into six basic types, which are based on geochemical history indicated by

radiochemical studies of representative samples. The first three types of disequilibrium have values of U in excess of eRa226. The last three types of disequilibrium have values of eRa226 in excess of U. Radioactive disequilibrium is a fairly complex phenomenon and an approach through multiple hypotheses are based on further interpretations provided by geological, geochemical and chemical evidence (Abdualhadi et al., 2018; Harmon, 2021). It can be observed that the dominancy of uranium contribution compared to K and Th to the heat production is a reflection of its high value of the numerical constants which is 0.097, which is higher and more than twice over the numerical constant of potassium and thorium which are 0.035 and 0.026 respectively. Though the alpha decay of uranium produces the greater part of the RHP (Birch, 1954) which implies that rocks with high ratio of U/Th will have promising RHP properties (Manning et al., 2007). Nevertheless, if the ratio U/Th is 0.25, then accumulatively uranium and thorium will give similar amounts of heat.

Even though the model of Rybach is reliant on the point that there is a fixed proportion between the end products (daughter) used for the estimation of the uranium and thorium equivalents (Rybach, 1976). However, these different daughter products have different movement properties whether as reducing or oxidizing conditions which implies that the end products possibly will be moved away from the rock over some period of time (Ivanovich and Harmon, 1992; Angileri et al., 2020) and this will result to disequilibrium which implies that there may perhaps be a greater or lesser thorium or uranium concentration than is specified by gamma-ray survey (Friedrichs et al., 2020).

There are certain end products which can be specially detached or remain comparative to the parent atom because of subsurface leaching (U235, U238, Th232). Such leaching can be that the identified radioactive decay may not be related to the quantity of concentrations of radionuclides (U and Th) in the rock (Sherman et al., 2007; Angileri et al., 2020). Some gases like radium and radon can also be a cause of disequilibrium due to their mobility and also being part of the decay series of uranium and thorium. The highly gaseous mobility state of radon gas could possibly cause disequilibrium and this is debatable if it is correct to make use of the full decay series for RHP estimation (Dickson and Scott, 1997). Although, uranium is the actual interest of disequilibrium effect since it is the principal contributor of heat to the RHP model compared to potassium or thorium and this dominancy is highlighted in the plot of the three major radionuclides (K-U-Th) against estimated RHP as seen in Figure 1. McCay et al. (2014) have discussed and identified various concerns about how to account for the incorrectness in the estimation of RHP produced by topography (Schwartz et al., 1992), distributional (Tyler et al., 1996) and series disequilibrium (Dickson and Scott, 1997; McCay et al., 2014) effects during gamma-ray surveying. Rosholt (1953) also proposed other different types of radioactive uranium series disequilibrium, which include daughter products deficiency (with correlation U > eRa226), daughter product deficiency time-related, Th230 deficiency, excess daughter product characterized by small uranium content, Ra226 excess and its direct daughter products, radium isotopes manifestation with very low or no U, Th230, Pa231 or Th232.

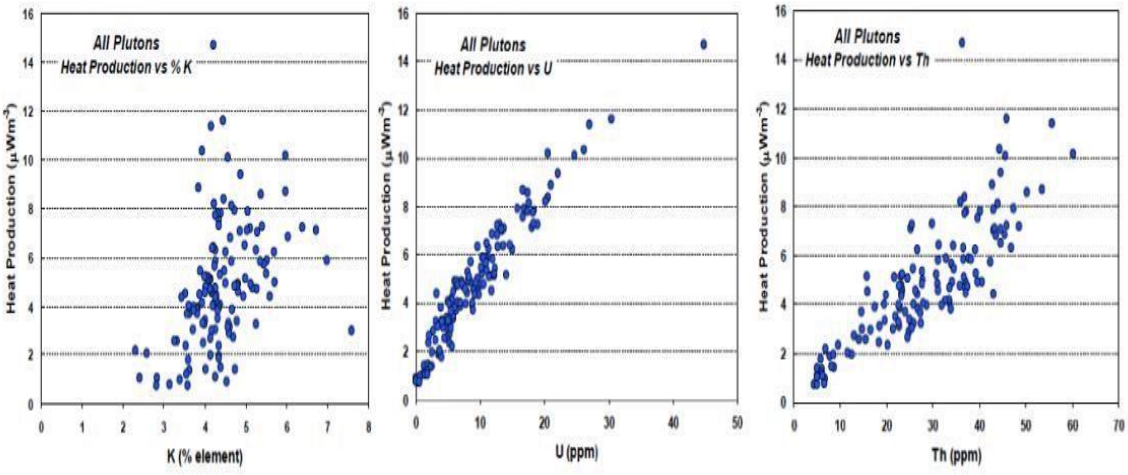

Figure 1. Plot of radioactive heat production (RHP) against K-U-Th concentrations using data from a Scottish case study (McCay et al., 2014)

The current research work reevaluated the numerical constants of the radionuclides based on decay schemes, half-life, mass changes and series disequilibrium effects from recent data to reflect the actual contribution of uranium's heat production to the total RHP. This is based on the gaps identified that affect the outcome of the estimation and accuracy of RHP in rocks. The gap identified in the series disequilibrium effect surrounding uranium and creating an environment that will actually reflect the actual contribution of the uranium to the RHP equation.

METHODOLOGY

Derivation of the revised heat production constants

In order to realize the aim and objectives of this work, some computations were carried out to get the revised heat production constants for the three radionuclides (K-U-Th) from recent data of decay patterns, half-lives and mass variances and alterations (Kocher, 1980; Fiorentini et al., 2005; de Meijer et al., 2006; Grupen, 2010; Clauser, 2020) using equations 3 and 4 (Table 2). The individual maximum Beta energies were summed up based on the decay schemes ($\sum E_{\beta max}$) and the total absorbed energy per atom is given by:

$$E_{abs} = E_{\Delta m} - 0.667 \sum E_{\beta max} \quad (3)$$

The RHP constants were calculated from the relation (Rybach, 1976):

$$B_i(cal/g, y) = f \frac{6.025 \cdot 10^{23}}{M} \frac{0.693}{T_{\frac{1}{2}}} u E_{abs}(MeV) \quad (4)$$

Where f = isotopic abundance, M =atomic mass number, $T_{1/2}$ = isotope half-life, i in years and u with a conversion factor of 1 MeV = 3.83×10^{-14} cal.

The RHP constants (B_i) are generally assumed to be in calories per unit time and radioactive isotope mass from equation 4 were converted and standardized to the universally accepted RHP unit of microwatt per meter cube (μWm^{-3}). The revised numerical constants estimated for this work from recent data are presented in Table 3, which were used to develop the new RHP equation. Secondly, the modified RHP model was validated using radiometric data from different regions as given in Table 4 and also compared with the existing RHP models of Rybach and Birch and a performance error metrics was applied to ascertain which model performed better of the three models against the observed model. The error metrics used are SSE, MAE, RMSE and R^2. The observed model for the work took cognizant of the disequilibrium factor of uranium numerical constant which was 0.388. This was arrived from the observation of McCay et al. (2014) for the ratio of U/Th which was 0.25 and this implies that 0.388 should be the actual numerical constant contribution of uranium. The decay energy of radionuclides was derived from the mass changes between parent and daughter products by accounting for the number emitted α-particles (He^4). This energy decay values include the emitted β-particles and ϒ-radiation contributions. For the β-emission, the amount of energy taken by neutrino must be accounted for through the addition of the individual maximum β-energies using the equation 3. The work flow for the methodology used in this work is shown in Figure 2.

The modified RHP and the existing RHP models were subjected to radiometric data available from the six regions of Nigeria and a region in India. The variations of the respective RHP models for each region was observed and compared. In general, the variations of contribution of radioactive elements across regions were determined and also the level of RHP across the regions. The Birch, Rybach, the new (or modified) and observed RHP (considering uranium series disequilibrium effect) models were symbolized as A_1, A_2, A_3 and A_4 respectively for easy identification. The modified RHP model was derived from the steps used in the derivation of the numerical constants of Rybach (1976) and Birch (1954) but used an updated and recent gamma spectrometry data (Kocher, 1980; Van Schumus, 1995; Grupen, 2010) of decay energies of the radionuclide based, which was compared with that of Rybach and Birch as shown in Table 3.

Table 2. Decay energies of radionuclide based on data from Fiorentini et al. (2005), de Meijer et al. (2006) and Clauser (2020)

Isotope	Rybach (1976)	This work	Rybach (1976)	This work		Rybach (1976)	Birch (1954)	This work
	$E_{\Delta m}$	$E_{\Delta m}$	$\sum E_{\beta max}$	$\sum E_{\beta max}$	$\sum E_{\alpha max}$	E_{abs}	E_{abs}	E_{abs}
U238	51.667	51.704	7.99	0.00	4.1940	46.34	47.40	51.7037
U235	46.392	46.403	1.71	0.00	4.3784	45.26	45.20	46.4034
Th232	42.793	42.649	5.71	0.00	4.0045	38.99	39.80	42.6487
K40	-	1.4896	-	0.4543	0.00	-	-	1.18658

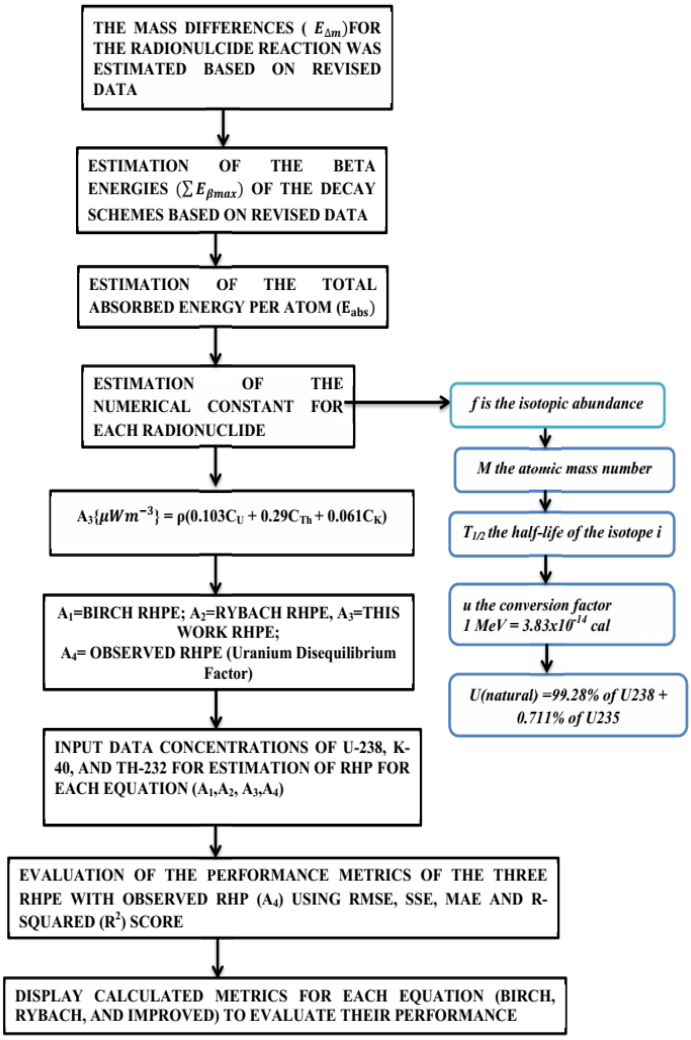

Figure 2. Flow chart indicating the methodology

Table 3. Reviewed heat production constants for this work compared with Rybach (1976) and Birch (1954).

Isotope	Rybach (1976) [Data from works of Hyde et al., (1964) and Brunee and Voshage (1964)]			Birch (1954)	RHP Numerical constants (B) (cal/g, y)			
	$E_{\Delta m}$ (MeV)	$\sum E_{\beta max}$ (MeV)	E_{abs} (MeV)	E_{abs} (MeV)	Birch (1954)	Rybach (1976)	This work (β-decay)	This work (α-decay)
U238	51.667	7.99	46.34	47.4	0.71	0.692	0.766	0.7247
U235	46.392	1.71	45.26	45.2	4.3	4.34	0.0323	0.0303
U(natural)					0.73	0.718	0.2099	0.1967
Th232	42.793	5.71	38.99	39.8	0.20	0.193	0.7606	0.7216
K(natural)					27x10^{-6}	26.2x10^{-6}	45.4x10^{-6}	57.02x10^{-6}

Table 4. Source of radiometric data from different regions as used in present study

Location	Rock types	Data source
Southwest Nigeria	Igneous, metamorphic	Joshua and Alabi (2012), Sedara (2020), Asere and Sedara (2020)
Southeast Nigeria	Igneous, metamorphic	Joshua et al. (2008)
South-south Nigeria	Igneous, metamorphic	Sokari et al. (2022), Bubu and Ononugbo, (2017)
Northcentral Nigeria	Igneous, metamorphic	Ojo et al. (2015)
Northeast Nigeria	Igneous, metamorphic	Ehinola et al. (2005), Yusuf (2016), Oyebanjo et al. (2016)
Northwest Nigeria	Igneous, metamorphic, sedimentary	Bisan (2011), Aisabokhae and Tampul (2020)
India	Igneous, metamorphic, sedimentary	Podugu et al. (2017)

Table 5. Summary of revised numerical constants

	Numerical constants of RHP Models			
Radionuclides	Birch (1954) (A_1)	Rybach (1976) (A_2)	This work (A_3)	USD Factor (A_4)
K	0.036	0.0348	0.061	0.036
U	0.098	0.0952	0.103	0.388
Th	0.268	0.0256	0.029	0.026
mean	0.13	0.05	0.06	0.15
stdev	0.12	0.04	0.04	0.21
min	0.04	0.03	0.03	0.03
max	0.27	0.10	0.10	0.39

RESULTS AND DISCUSSION

The RHP constants for natural uranium, thorium and potassium of Rybach (1976) were some percent lesser than that of Birch (1954). There were also slight differences in the values of $E_{\beta max}$ and $E_{\alpha max}$, which was based on the revision of the radionuclide data. After the values of $E_{\Delta m}$, $E_{\beta max}$, and E_{abs} were derived, the numerical constants for the respective radioelements was gotten too. The numerical constants for the three models were compared in terms of the percentage deviation. The percentage deviation of U-238 from the Rybach and Birch is 9.7% and 7.3%, respectively and that of the uranium (natural) is 5.6% and 4%, respectively from the model of this work Table.5 . This deviations are expected and of significant contribution to the outcome of the estimation of the numerical constants. The revised RHP constants are several percent higher (6.2% for U; 11.5 % for Th) than the values of Rybach (1976) and Birch (1954), except for potassium which is much higher (74.3%). The RHP equation arrived at for this work is:

$$A_3(\mu W m^{-3}) = \rho(0.103C_U + 0.029C_{Th} + 0.061C_K) \quad (5)$$

where ρ= density (kg/m^3) and A_3 is the RHP in $\mu W m^{-3}$

Comparison of the RHP Numerical constants and RHP models

The numerical constants of the radionuclides were arrived at using the earlier steps of Birch and Rybach models to get the new model A_3 but the data used were slightly different since the data were revised in decay series, mass defect, and disequilibrium. The Birch and Rybach models were derived based on data from Hyde et al. (1964) and Brunee and Voshage (1964) and the A_3 model was based on data for the parameters in the methodology section. The absorbed energies of the decay schemes,the total absorbed energy per atom and numerical constant for each radionuclide for the respective HPEs, were arrived at. Also the RHP models data were used to compute the RHP for each region as seen in Table 6.

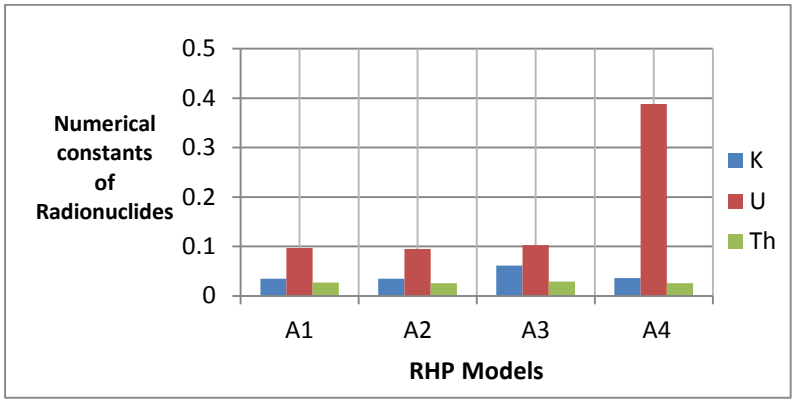

Figure 3. Comparison of numerical constants of radionuclide for the RHP models

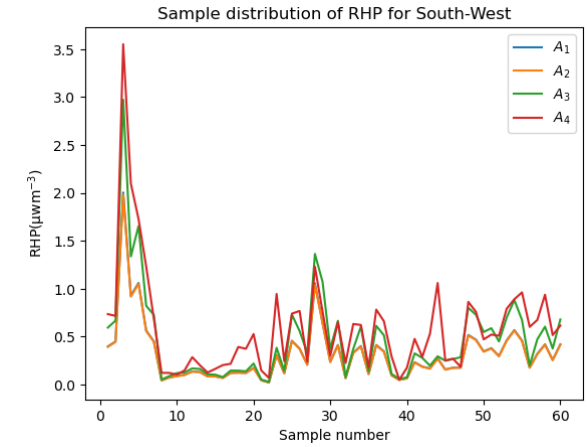

Figure 4. Distribution plot of the RHP models in the southwest region

The implications of the effect of the series disequilibrium in the RHP models have been identified. The new model have been able to cater for the disequilibrium effect though, it is difficult to actually evaluate accurately the intensity of contributing power of the respective radionuclides to the total RHP but we have been able to go further by providing a simplified estimate of this disequilibrium effect to the RHP. Using data from the literature and comparing the modified RHP model with the existing models to calculate the deviation from each model the radiometric data were subjected to the three RHP models (A_1, A_2, A_3) and was discovered that the total RHP for A_3 was the highest for all regions followed by A_1 and A_2 models respectively (A_3>A_1>A_2). This is due to result of the increase in the numerical constants of uranium and thorium in the new model as can be visualized in Figure 3. This analysis points out to the fact that the uranium's role is very vital to the heat contribution to the total RHP and the deviation of both uranium and thorium are highlighted in Table 5 and it shows that they are both vital in the contribution of heat to the total RHP. The high deviation of the disequilibrium from unity is of utmost concern since the ratio of the parent –daughter relation is 0.25 which is a factor to be considered for the disequilibrium effect. The numerical constant for uranium which is 0.0952 in the Rybach's model, was divided by the 0.25 factor in the discrepancies which gives 0.388. This value though shows the approximate or assumed value for which uranium should be contributing to the total RHP. This value is near to the value of 0.103 when compared with our new model (Table 5). A direct reflection of HP within southern regions of Nigeria and high surface heat flow naturally indicate high crustal radioactivity in comparison to the universal average (Neumann et al., 2000; McLaren et al., 2003). These high values of heat have been attributed to anomalous Heat production (Abraham et al., 2014; Sedara, 2020; Sedara and Alabi, 2021; Sedara, 2022). The average RHP predicted from the improved RHP model is only slightly higher than the other two models by Birch (1954) and Rybach (1976). This does not necessarily undermine our model since the many crustal models are carefully crafted from chemical

and deep crustal cross sections from geophysical restraints provided by other models of the crust and surface heat flow (Rudnick and Gao, 2003). Nevertheless, there may be many expectations and assumptions that may have been factored into the different thermal models across the globe, which may be incorrect (for example, Hasterok and Gard, 2016). Possibly, the improved RHP model from this work could be used to improve the estimation of RHP of crustal continental compositions.

The frequency distribution of the RHP models is displayed for Southwest (Figure 4), Southeast (Figure 5), South-south (Figure 6), Northeast (Figure 7), Northwest (Figure 8), Northcentral (Figure 9) and India (Figure 10) regions and it showed that the A_3 model came closest to the observed (actual) model in all the regions considered than the other two RHP models.

Table 6. RHP models with the observed model (A_4) on dataset for all the regions

	RHP Models (μWm^{-3})							
	A_1		A_2		A_3		A_4	
Region	range	mean	range	mean	range	mean	range	mean
SW	0.02-2.00	0.32±0.32	0.02-1.98	0.32±0.32	0.03-2.97	0.47±0.48	0.05-3.55	0.59±0.56
SE	0.90-8.65	2.65±1.54	0.88-8.54	2.61±1.52	1.01-11.55	3.01±1.87	1.71-17.82	5.93±3.68
SS	0.27-10.28	4.64±2.02	0.27-10.12	4.56±1.98	0.33-11.54	5.09±2.24	0.50-20.11	12.86±4.09
NE	0.86-6.26	2.55±0.72	0.85-6.16	2.51±0.71	0.96-6.96	2.81±0.78	1.90-14.99	6.64±2.16
NW	5.35-22.81	10.83±3.55	5.25-22.41	10.63±3.49	5.77-24.58	11.72±3.82	18.28-73.15	35.83±11.78
NC	0.15-0.41	0.30±0.06	0.15-0.40	0.29±0.06	0.16-0.44	0.32±0.06	0.51-1.48	1.02±0.20
IND	0.33-15.90	4.21±2.95	0.32-15.63	4.14±2.90	0.42-17.36	4.80±3.25	0.81-50.58	9.44±7.60

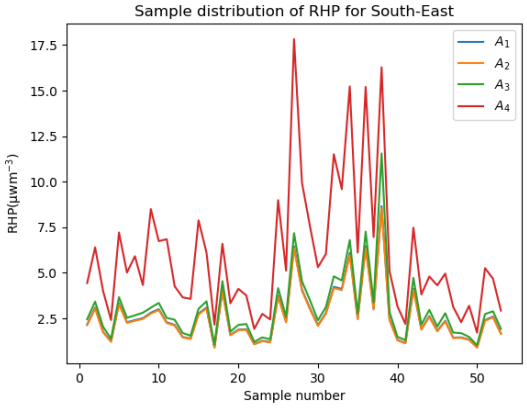

Figure 5. Distribution plot of the RHP models in the Southeast region

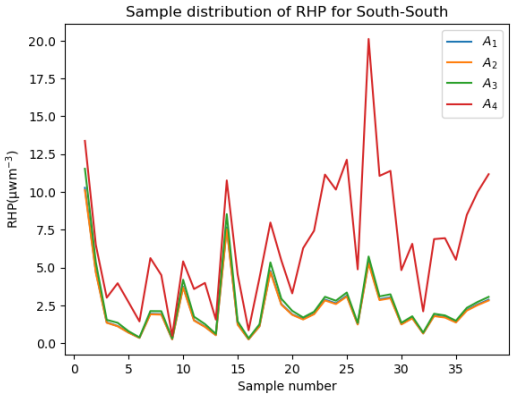

Figure 6. Distribution plot of the RHP models in the South-south region

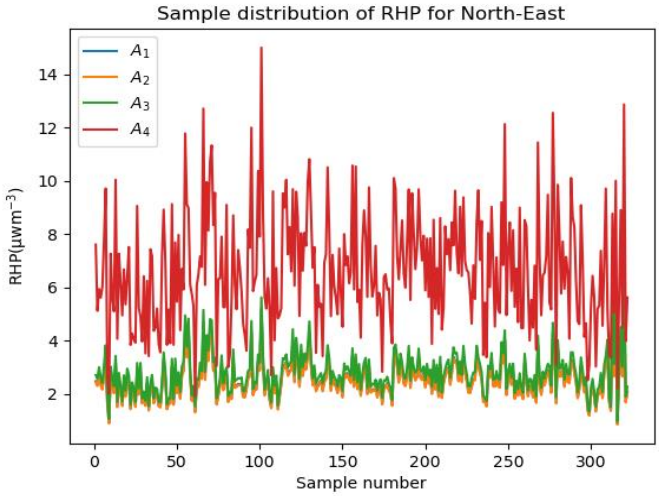

Figure 7. Distribution plot of the RHP models in the Northeast region

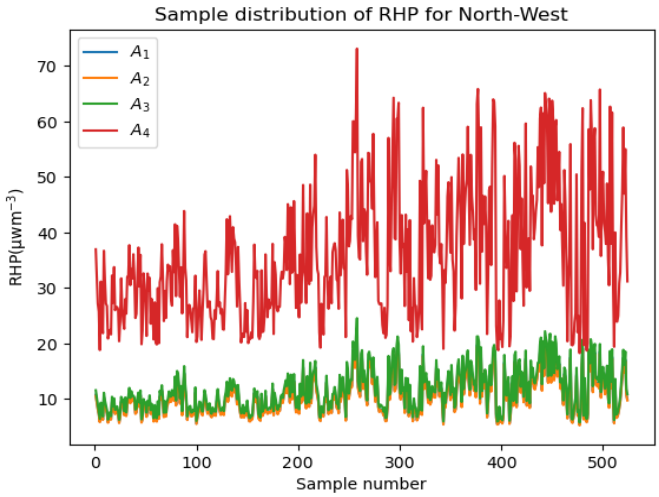

Figure 8. Distribution plot of the RHP models in the Northwest region

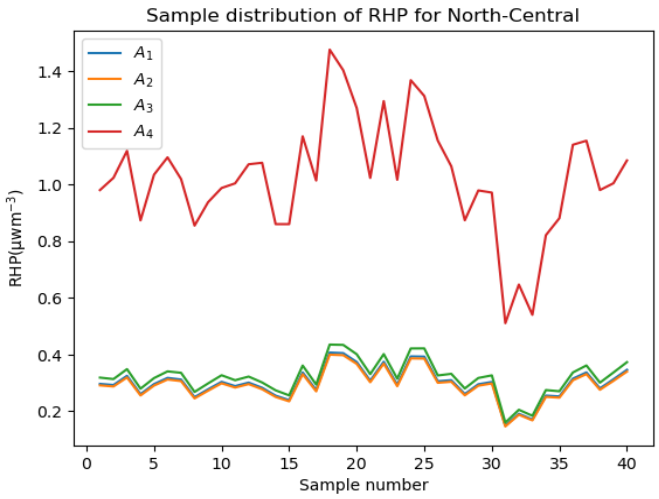

Figure 9. Distribution plot of the RHP models in the Northcentral region

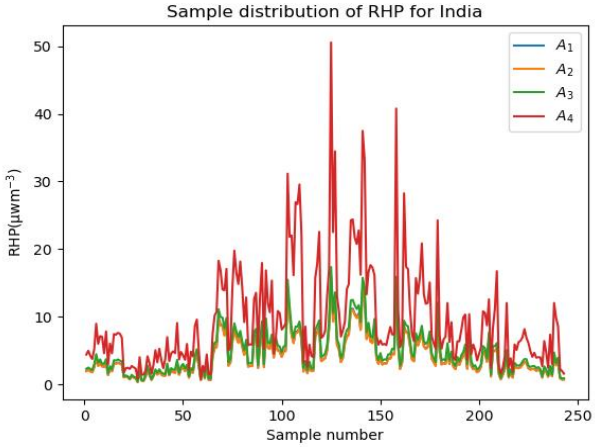

Figure 10. Distribution plot of the RHP models in the India region

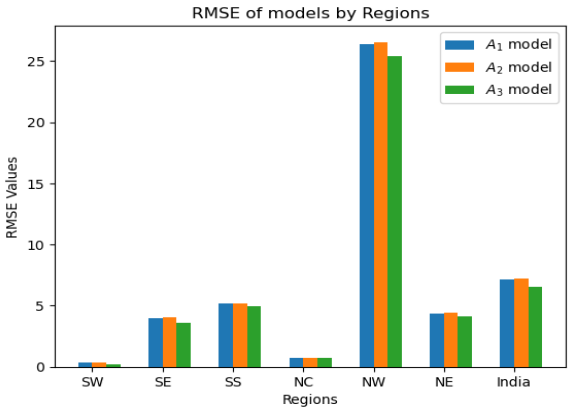

Figure 11. RMSE metrics of the RHP models across all the regions

Performance metrics and evaluation of RHP models

This study tested four performance error metrics on the RHP models and the performance were evaluated by matching with observed RHP model (A_4) which accommodated the disequilibrium factor of uranium. The metrics used to evaluate the performance are:

(1) Root-mean-square error (RMSE) which is expressed as:

$$RMSE = \sqrt{MSE} = \sqrt{\frac{1}{N}\sum_{i=1}^{N}(y_i - \hat{y})^2} \quad (6)$$

Where $\hat{y}$=the actual, y_i=the predicted, N=the number of outputs.

(2) Mean absolute error (MAE) which can be expressed as:

$$\mathrm{MAE} = \frac{1}{n}\sum_{i=1}^{n}|X_i - Y_i| \quad (7)$$

(3) Squared correlation (R^2) which can be expressed as:

$$R^2 = \left(\frac{\sum_{i=1}^{n}(X_i - \overline{X})(Y_i - \overline{Y})}{\sqrt{\sum_{i=1}^{n}(X_i - \overline{X})(Y_i - \overline{Y})}}\right)^2 \quad (8)$$

where X= the average of X_i and Y=the average of Y_i.

(4) Sum of Squares Error (SSE) given as:

$$SSE = \sum_{i=1}^{n}(X_i - \bar{X})^2 \quad (9)$$

Where n= the number of observations, X_i =the value of the ith observation and $\bar{X}$ =the mean of all observations. Dimensional differences were eliminated to improve the generalization ability of models (Zhou et al., 2020).

Table 7 shows the performance metrics of the models with the observed model and it was observed that the improved equation (A_3) gave a lower RMSE (Figure 11), lower MAE (Figure 12), lower SSE (Figure 13) and higher R^2 value (Figure14) than Birch (A_1) and Rybach (A_2) models. So a higher R (coefficient of correlation) value shows how well they correlate. The lower the RMSE/SSE/MAE, the better the equation fits the observed.

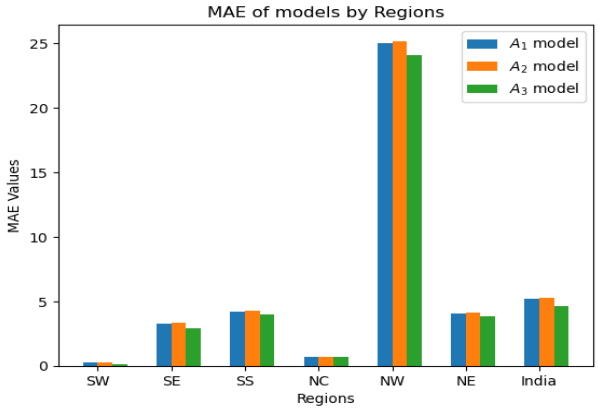

Figure 12. MAE metrics of the RHP models across all the regions

Table 7. Performance metrics of RHP models with the observed model (A_4) on dataset for all the regions

Regions	RHP Models	Root Mean Squared Error (RMSE)	Mean Absolute Error (MAE)	Sum of Squared Error (SSE)	Coefficient of Correlation (R)	Coefficient of Determination (R^2)
India	Birch (A_1)	7.13687	5.23292	12377.2	0.95355	0.90926
India	Rybach (A_2)	7.21663	5.30013	12655.4	0.95327	0.90873
India	Improved (A_3)	6.54931	4.64241	10423.1	0.94785	0.89842
Northcentral	Birch (A_1)	0.73978	0.725	21.8913	0.97537	0.95135
Northcentral	Rybach (A_2)	0.74523	0.73037	22.2149	0.97518	0.95099
Northcentral	Improved (A_3)	0.71778	0.70328	20.6086	0.97234	0.94545
Northeast	Birch (A_1)	4.37818	4.09213	6172.24	0.88329	0.7802
Northeast	Rybach (A_2)	4.42193	4.13509	6296.21	0.8825	0.77881
Northeast	Improved (A_3)	4.12659	3.8339	5483.27	0.86745	0.75247
Northwest	Birch (A_1)	26.3504	25.0054	363836	0.98285	0.966
Northwest	Rybach (A_2)	26.5514	25.1969	369409	0.98273	0.96577
Northwest	Improved (A_3)	25.4167	24.1062	338510	0.9811	0.96255
Southeast	Birch (A_1)	3.97267	3.28615	836.45	0.95645	0.91479
Southeast	Rybach (A_2)	4.01983	3.32858	856.43	0.95591	0.91377
Southeast	Improved (A_3)	3.5656	2.92244	673.814	0.93012	0.86513
South-south	Birch (A_1)	5.16102	4.21669	1012.17	0.71035	0.50459
South-south	Rybach (A_2)	5.2015	4.2573	1028.11	0.70914	0.50288
South-south	Improved (A_3)	4.98144	3.98527	942.961	0.6867	0.47156
Southwest	Birch (A_1)	0.38128	0.26963	8.72236	0.94988	0.90228
Southwest	Rybach (A_2)	0.38563	0.27313	8.92269	0.94953	0.90161
Southwest	Improved (A_3)	0.23244	0.15553	3.24166	0.9362	0.87647

The A_3 has the best performance in all the metrics compared with the observed model. The A_3 model gave a higher R^2 value and lower RMSE, MAE, SSE values which is an indicator of best performance. In general, the improved model (A_3) performed well and better than the other two RHP models (Birch and Rybach) in all the regions. The error metric was done for the RHP models with the observed model for all the regions to check the variations of the errors across the regions. The correlation between the RHP models and observed model with R^2 values is in the range of 47-97% across the regions. The RMSE values were high and ranged between 23 and 27. The A_3 RHP model has the best performance in all the metrics compared with the observed model. The A_3 model gave a highest R^2 and R values in all the regions and lowest values of RMSE, MAE, and SSE in all the regions. In summary, this is an indicator of best performance and as a result, a higher R^2 value and lower SSE, MAE and RMSE values shows best performance (Table 7)

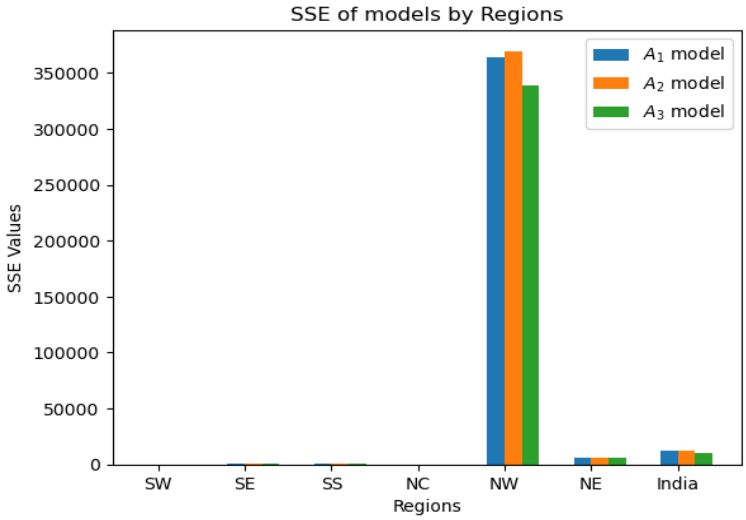

Figure 13. SSE metrics of the RHP models across all the regions

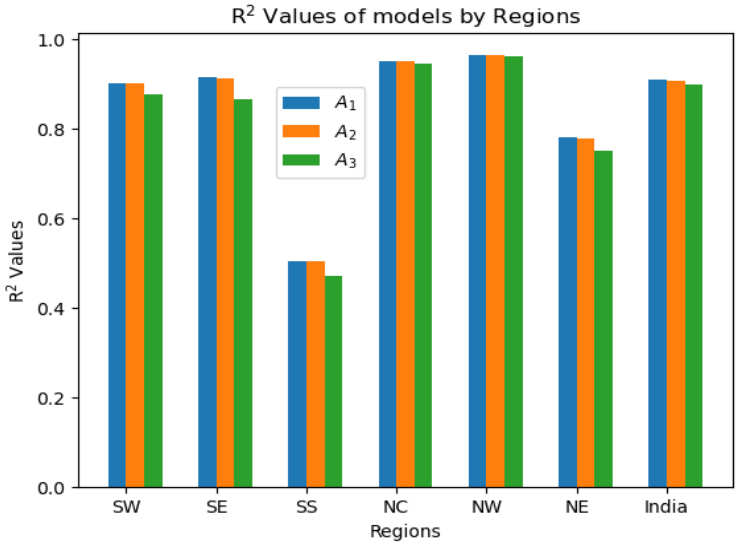

Figure 14. R-squared metrics of the RHP models across all the regions

CONCLUSIONS

In this study, we modified an existing RHP model which accommodated the series disequilibrium factor to reduce the disequilibrium factor error. The model was validated and tested with primary and secondary source data. The new RHP model performed better than the existing RHP models in error metrics returning a higher R^2 value and lower MAE, SSE and RMSE values with the observed model in all regions considered which is an indicator of best performance and as a result a higher R^2 value shows how well they correlate. Similarly, the RHP values tend to increases for the improved model and all the same also a significant relationship is apparent between the improved model (A_3) and the other models (A_1 and A_2).

It was discovered that the RHP values of rocks varies regionally and formation dependent. But, it is challenging to characterize these trends directly to only physical procedure because of the densities of formations, fluid variation and evolution which can upset different samples. These correlations may not likely be linked but they can be used for the estimation of average RHP on a local basis or state. The accuracy of the RHP measurement will continue to improve with exposure time and the accuracy of the interpretation and its uncertainties depends on the reviewed available data. In this work, we have identified the different influences that lead to RHP estimation which are not characteristic of the underlying rock RHP and can also thwart the collection of accurate radiometric data in the field and measuring such inaccuracies represents an area for further improvement for

geothermal applications. The resulting exercise serves as a useful improvement in the accuracy of estimating RHP which was quantitatively accounted for during this study.

1. The RHP models brings A_3 as the highest contribution (24.6 μWm^{-3}) with A_1 (22.8 μWm^{-3}) and A_2 (22.4 μWm^{-3}) for the NW region followed by the IND, SE, SS, NE, SW and NC regions in that order. The RHP models are in the order A_3>A_1>A_2 for all regions. Overall, A_3 return the highest RHP values across all regions.
2. The new model is given as:
   $A_3(\mu Wm^{-3}) = \rho(0.103C_U + 0.061C_K + 0.029C_{Th})$
   which minimize the error in the estimation of RHP because of its nearness to the observed disequilibrium factor.
3. The A_3 RHP model gave a higher R^2 value and lower RMSE, MAE, SSE values than the other two models which is an indicator of best performance. This performance was done for all the regions and it reflected same in the entire region considered.
4. The new RHP model (A_3) performed well in all the regions in Nigeria and outside Nigeria. This shows that the new RHP model is not geological-formation dependent.

ACKNOWLEDGMENT

The authors will like to appreciate the Department of Earth Sciences, Adekunle Ajasin University for the use of gamma ray spectrometer and acquisition of the primary radiometric data utilized for this work and also thank other sources of the secondary radiometric data used for this work. The authors will like to appreciate the reviewers for their suggestions and comments to make the work more robust and interesting.

Author Credit Statement

OOA developed the concept and design this work. DTA wrote the codes for the work. SOS and IAA did the analysis and interpretation of the data as well as writing and editing of the manuscript. In general OOA supervised and validated the work.

Compliance with Ethical Standards

The authors declared that they have no conflict of interest and adhere to copy right norms

Data Availability Statement

The data will be available on reasonable request

REFERENCES

Abdualhadi, S.A., Mauz, B., Joss, S.D.T. and Nolan, P.J., 2018. Detecting and quantifying uranium-series disequilibrium in natural samples for dosimetric dating applications. Radiation Measurements 114, https://doi.org/10.1016/j.radmeas.2018.04.011

Abraham, E.M., Lawal, K.M., Ekwe, A.C., Alile, O., Murana, K.A. and Lawal, A.A., 2014. Spectral analysis of aeromagnetic data for geothermal energy investigation of Ikogosi Warm Spring - Ekiti State, southwestern Nigeria. Geothermal Energy, 2(6), 1-21 https://doi.org/10.1186/s40517-014-0006-0.

Aisabokhae, J. and Tampul, H., 2020. Statistical variability of radiation exposures from Precambrian basement rocks, NW Nigeria: Implication on radiogenic heat production. Scientific African, 10, 577. https://doi.org/10.1016/j.sciaf.2020.e00577

Akingboye, A.S., Ogunyele, A.C., Jimoh, A.T., Adaramoye, O.B., Adeola, A.O. and Ajayi, T., 2021. Radioactivity, radiogenic heat production and environmental radiation risk of the Basement Complex rocks of Akungba-Akoko, southwestern Nigeria: insights from in situ gamma-ray spectrometry. Environ. Earth Sci., 80, 228. https://doi.org/10.1007/s12665-021-09516-7

Angileri, A., Sardini, P., Beaufort, D., Amiard, G., Beaufort, M.F., Nicolai, J., Siitari-Kauppi, M. and Descostes, M., 2020. Mobility of daughter elements of 238U decay chain during leaching by In Situ Recovery (ISR): New insights from digital autoradiography, J. Environmental Radioactivity, 220–221,106274, https://doi.org/10.1016/j.jenvrad.2020.106274.

Asere, A.M. and Sedara, S.O., 2020. Determination of Natural Radioactivity Concentration and Radiogenic Heat Production in Selected Quarry Sites in Ondo State, Nigeria. NIPES J. Sci. Technology Res., 2(3), 256 - 271

Asfahani, J., 2018. Heat production estimation by using natural gamma-ray well-logging technique in phosphatic khneifis deposit in Syria. Appl. Radiation and Isotopes, 145, 209-216

Birch, F., 1954. Heat from radioactivity. In Nuclear Geology; Wiley: New York, NY, USA, pp. 148-174.

Bisan, Y., 2011. Ground Radiometric Survey of Kufena, Zaria, Northwest Nigeria. M.Sc thesis, The Postgraduate School, Ahmadu Bello University, Zaria, Nigeria

Brunne, C. and Voshage, H., 1964. Massenspektrometrie. Thiemig, Miinehen (1964)

Bubu, A. and Ononugbo, C. P., 2017. Radiogenic Heat Production Due to Natural Radionuclides in the Sediments of Bonny River, Nigeria. J. Scientific Res. and Reports 17(6), 1-9, Article no.JSRR.39159, DOI: 10.9734/JSRR/2017/39159

Cai, P., Shi, X., Hong, Q., Li, Q., Liu, L., Guo, X. and Dai, M., 2015. Using 224Ra/228Th disequilibrium to quantify benthic fluxes of dissolved inorganic carbon and nutrients into the Pearl River Estuary. Geochim. Cosmochim. Acta, 170, 188-203.

Chandrasekaran, R., Ravisankar, G., Senthilkumar, K., Thillaivelavan, B., Dhinakaran, P., Vijayagopal, S.N., Bramha, B. and Venkatraman, N., 2014. Spatial distribution and lifetime cancer risk due to gamma radioactivity in Yelagiri Hills, Tamilnadu, India. Egyptian J. Basic and Appl. Sci., 1(1) 38-48.

Cinar, H., Altundas, S., Çelik, N. and Maden, N., 2017. In situ gamma ray measurements for deciphering of radioactivity level in the Sarihan pluton area of northeastern Turkey. Arabian J. Geosci., 10 (19). https://doi.org/10.1007/s12517-017-3225-4.

Cinelli, G., Brattich, E., Coletti, C., De Ingeniis, V., Mazzoli, C., Mostacci, D., Sassi, R. and Tositti, L., 2020. Terrestrial gamma dose rate mapping (Euganean Hills, Italy): comparison between field measurements and HPGe gamma spectrometric data. Radiat. Eff. Defect Solid 175, 54–67. https://doi.org/10.1080/10420150.2020.1718131.

Clauser, C., 2020. Radiogenic heat production of rocks. In: Gupta, H.K. (Ed.), Encyclopedia of Solid Earth Geophysics. 2nd ed., Springer, Dordrecht, preprint. Encycl Earth Sci Ser 7p. https://doi.org/ 10.1007/978-3-030-10475-7_74-1.

De Meijer, R. J., Smith, F. D., Brooks, F. D., Fearick, R. W., Wörtche, H. J. and Mantovani, F., 2006. Towards Earth Antineutrino Tomography (EARTH). Earth, Moon and Planets, 99(1-4), 193-206.

Dickson, B. and Scott, K., 1997. Interpretation of aerial gamma-ray surveys-adding the geochemical factors. AGSO J. Aust. Geol. Geophys., 17, 187–200.

Ehinola, E.A., Joshua, E.O., Opeloye, S.A. and Ademola, J.A., 2005. Radiogenic heat production in the cretaceous sediment of Yola arm of Nigeria Benue. Through: Implications for thermal history and hydrocarbon generation. J. Applied Sci., 5, 696-701.

El Afandy, A.H., Fawzy, K.M., Assran, H.M., Zeid, E.K. and El Shayip, J.B., 2018. Radioactivity and geochemical characteristics of post collision granites, west Wadi Murrah area, South Eastern Desert, Egypt. J. African Earth Sci., 146, 78-94.

Fall, M., Baratoux, D., Ndiaye, P.M., Jessell, M. and Baratoux, L., 2018. Multi-scale distribution of Potassium, Thorium and Uranium in Paleoproterozoic granites from eastern Senegal. J. African Earth Sci., 148,30-51.

Faruwa, A.R., Qian, W., Agbele, A., Babinisi, A. and Yekeen, B., 2020. Airborne radiometric mapping for natural radiation assessment over Okitipupa southeast belt of the bituminous sand feld of Nigeria. Radiat. Protect. Dosim. 192.https://doi.org/10.1093/rpd/ncaa188.

Fiorentini, G., Lissia, M., Mantovani, F. and Vanucci, R., 2005. Geo-neutrinos: A new probe of Earth's interior. Earth Planet. Sci. Lett., 557, 139-146.

Friedrichs, B., Schmitt, A.K., McGee, L. and Turner, S., 2020. U–Th whole rock data and high spatial resolution U–Th disequilibrium and U–Pb zircon ages of Mt. Erciyes and Mt. Hasan Quaternary stratovolcanic complexes (Central Anatolia). Data in Brief, Volume 29, 105113. https://doi.org/10.1016/j.dib.2020.105113.

Grozeva, N.G., Radwan, J., Beaucaire, C. and Descostes, M., 2022. Reactive transport modeling of U and Ra mobility in roll-front uranium deposits: Parameters influencing 226Ra/238U disequilibria. J. Geochem. Expl., 236, 106961, https://doi.org/10.1016/j.gexplo.2022.106961.

Grupen, C., 2010. Introduction to Radiation Protection, Graduate Texts in Physics, DOI 10.1007/978-3-642-02586-0, Springer-Verlag Berlin Heidelberg 2010

Harmon, R.S., 2021. Introduction and Overview, Editor(s): David Alderton, Scott A. Elias, Encyclopedia of Geology (Second Edition), Academic Press, 2021, Pages 1-12,ISBN 9780081029091, https://doi.org/10.1016/B978-0-12-409548-9.12017-2.

Hasterok, D. and Gard, M., 2016. Utilizing thermal isostasy to estimate sub-lithospheric heat flow and anomalous crustal radioactivity. Earth Planet. Sci. Lett., 450, 197- 207.

Hasterok, D. and Webb, J., 2017. On the radiogenic heat production of igneous rocks. Geosci. Frontiers, 8(5), 919-940.

Hyde, E.K., Perlmanand, I. and Seaborg, G.T., 1964. The Nuclear Properties of the Heavy Elements. Il Detailed Radioactive Properties, Prentice "Hall, Englewood Cliffs, N.J..

Ivanovich, M. and Harmon. R.S., 1992. Uranium-series disequilibrium: applications to earth, marine, and environmental sciences. Oxford Clarendon Press, Oxford, New York. Oxford University Press, 2ND Edition.

Joshua, E. O., Ehinola, O. A., Akpanowo, M. A. and Oyebanjo, O. A., 2008. Radiogenic Heat Production in Crustal Rock Samples of Southeastern Nigeria. European J. Scientific Res., 23(2), 305-316

Joshua, E.O. and Alabi, O.O., 2012. Pattern of Radiogenic Heat Production in Rock Samples of Southwestern Nigeria. J. Earth Sciences and Geotechnical Engineering, 2(2), 25-38

Ju, Y., Ryu, J., Drake, H., Im, H.S. and Baik, M., 2022. Long-term change in uranium migration processes in highly eroded granite, demonstrated by uranium series disequilibrium in fracture-filling materials. Appl. Geochemistry, 148, 105530, https://doi.org/10.1016/j.apgeochem.2022.105530.

Kocher, D. C., 1980. A Radionuclide Decay Data Base - Index and Summary Table. Prepared for the U. S. Nuclear Regulatory Commission Division of Safeguards, Fuel Cycle, and Environmental Research Under Interagency Agreement DOE 40-550-75 NRC FIN No. B0188. Prepared by the Oak Ridge National Laboratory Oak Ridge, Tennessee 37830. Operated By Union Carbide Corporation for the Department Of Energy

Lefebvre, P., Le Pape, P., Mangeret, A., Gourgiotis, A., Sabatier, P., Louvat, P., Diez, O., Mathon, O., Hunault, M., Baya, C., Darricau, L., Cazala, C., Bargar, J.R., Gaillardet, J. and Morin, G., 2022. Uranium sorption to organic matter and long-term accumulation in a pristine alpine wetland. Geochim. Cosmochim. Acta, 338, 322-346

Liao, D., Feng, D., Luo, J. and Yun, X., 2023. Relationship between radiogenic heat production in granitic rocks and emplacement age. Energy Geoscience, 100157, https://doi.org/10.1016/j.engeos.2023.100157.

Manning, D., Younger, P., Smith, F., Jones, J., Dufton, D. and Diskin, S., 2007. A deep geothermal exploration well at Eastgate, Weardale, UK: A novel exploration concept for low-enthalpy resources. J. Geol. Soc., 164, 371–382

McCay, A.T., Harley, T.L., Younger, P.L., Sanderson, D.C.W. and Cresswell, A.J., 2014. Gamma-ray spectrometry in geothermal exploration: State of the art techniques. Energies, 7, 4757–4780

McLaren, S., Sandiford, M., Hand, M., Neumann, N., Wyborn, L. and Bastrakova, I., 2003. The Hot South Continent: Heat Flow and Heat Production in Australian Proterozoic Terranes. Vol. 22 of Special Pub. Geological Society of Australia, pp. 151-161

Nada, A. and Aly, H.A.S., 2013. The effect of uranium migration on radionuclide distributions for soil samples at the El-Gor area, Sinai, Egypt. Applied Radiation and Isotopes, 84, 79-86.

Neumann, N., Sandiford, M. and Foden, J., 2000. Regional geochemistry and continental heat flow: implications for the origin of the South Australian heat flow anomaly. Earth Planet. Sci. Lett., 183, 107-120.

Ojo, E. O., Shittu, H. O., Adelowo, A. A., Ossai, B. N. and Emefiene, C. B., 2015. The Model of Radiogenic Heat Production in the Federal Capital Territory (FCT), Abuja, Nigeria. Int. J. Modern Phys. and Applications, 1(5), 200-204.

Oyebanjo, O.M., Ajayi, T. R. and Tchokossa, P., 2016. Radiogenic heat and hydrocarbon generation potential of sediments, Gongola Basin, Nigeria. Petroleum Exploration and Development, 43(3), 411. DOI:10.11698/PED.2016.03.11

Pereira, B.M. and Ferreira, F.J.F., 2018. Recognition of gold mineralization favorability zones through airborne gamma-ray spectrometry and magnetometry in Brusque and Botuvera´ region, southern Brazil. Braz. J. Geophys., 36, 361–374.

Plomerova, J., Babuška, V., Dorbath, C., Dorbath, L. and Lillie, R.J., 1993. Deep lithospheric structure across the Central African shear zone in Cameroon.Geophys.J.Int., 115(2), 381-390

Podugu, N., Ray, L., Singh, S. P. and Roy, S., 2017. Heat flow, heat production, and crustal temperatures in the Archaean Bundelkhand craton, north-central India: Implications for thermal regime beneath the Indian shield. J. Geophys. Res., Solid Earth, 122, doi:10.1002/2017JB014041.

Ray, L., Roy, S. and Srinivasan, R., 2008. High Radiogenic Heat Production in the Kerala Khondalite Block, Southern Granulite Province, India. Int. J. Earth Sci., 97, 257–267.

Reis, A.S., Ma, J.B.C. and Seer, H.J., 2020. Insights into tectonic reactivation and landscape development processes at the Paran´ a Basin border using integrated geomorphometric and radiometric analyses. Braz. J. Geol. 50 (4), e20190018. https://doi.org/10.1590/2317-4889202020190128.

Rosholt, J. N., 1953. Natural radioactive disequilibrium of the uranium series. US Geological Surv. Bull., 1084-A, 1953

Rudnick, R. and Gao, S., 2003. Composition of the continental crust. In: Rudnick, R. (Ed.), Treatise on Geochemistry: The Crust, vol. 3. Elsevier, pp. 1- 64. Ch. 1.

Rybach, L., 1976. Radioactive heat production: A physical property determined by the chemistry of rocks. In: Stems, R.G.J. (Ed.), Wiley-Interscience, New York, USA, pp. 309-318

Schwartz, G., Klingelé, E. and Rybach, L., 1992. How to handle rugged topography in airborne gamma-ray spectrometry surveys. First Break, 10, 11-17

Sedara, S.O., 2020. Modeling Heat flow from Radiogenic Heat properties of some common rock samples and its significance to geothermal modeling. Science & Technology, 6(22), 71-82

Sedara, S.O., 2022. Geophysical Analysis of Thermo-physical Properties of Rocks in Ikogosi field for Geothermal Energy Prospect. Turkish J. Geosci. 3(1), 39-48. https://doi.org/10.48053/turkgeo.1112911

Sedara, S.O. and Alabi, O.O., 2021. Geothermal prospect scaling of Ikogosi warm spring using combined geophysical methods. J. Ind. Geophys. Union, 25(5), 55-70

Sherman, H.M., Gierke, J.S. and Anderson, C.P., 2007. Controls on spatial variability of Uranium insandstone aquifers. Ground Water Monit. Remed., 27, 106-118

Sims, K.W.W., Stark, G, J. and Reagan, M. K., 2021. An Essential Quaternary Clock for Earth System Sciences: An Overview of the Theory and Applications of U and Th Decay Series Isotopes for the Dating of Young Igneous and Sedimentary Rocks, Editor(s): David Alderton, Scott A. Elias, Encyclopedia of Geology (Second Edition), Academic Press, 2021, Pages 76-100, https://doi.org/10.1016/B978-0-08-102908-4.00167-3.

Sokari, S. A., Gbarato, O. L. and Ononugbo, C. P., 2022. Radiogenic Heat Production Due to Natural Radionuclides in Soil and Sediments of Coastal Communities of Okrika Local Government Area of Rivers State, Nigeria. Asian J. Res. and Reviews in Phys., 6(1), 14-20, Article no.AJR2P.83222

Tabod, C.T., Fairhead JD, Stuart, GW, Ateba B, and Ntepe, N., 1992. Seismicity of the Volcanic Line, 1982-1990.Tectonophysics, 2112, 303-320

Tyler, A., Sanderson, D.C., Scott, E.M. and Allyson, J., 1996. Accounting for spatial variability and fields of view in environmental gamma ray spectrometry. J. Environ. Radioact., 33, 213–235.

Valković, V., 2019. Radioactive nuclides in nature, Editor(s): Vlado Valković, Radioactivity in the Environment (2nd edition), Elsevier, Pages 1-29. https://doi.org/10.1016/B978-0-444-64146-5.00001-X.

Van Schmus, W.R., 1995. Natural radioactivity of the crust and mantle T.J. Ahrens (Ed.), Global Earth Physics, A Handbook of Physical Constants, vol. 1 (1995), 10.1029/RF001p0283 AGU Reference Shelf 1

Veerasamy, N., Kasar, S., Murugan,R., Inoue, K., Natarajan, T., Ramola,R.C., Fukushi,M. and Sahoo, S.K., 2023. 234U/238U disequilibrium and 235U/238U ratios measured using MC-ICP-MS in natural high background radiation area soils to understand the fate of uranium. Chemosphere. 323, ,138217. https://doi.org/10.1016/j.chemosphere.2023.138217.

Youssef, M.A.S., Sabra, M.E.M., Abdeldayem, A.L., Masoud, A.A. and Mansour, S.A., 2017. Uranium migration and favorable sites of potential radioelement concentrations in Gabal Umm Hammad area, Central Eastern Desert, Egypt. NRIAG J. Astronomy and Geophys., 6(2), 368-378. https://doi.org/10.1016/j.nrjag.2017.10.004.

Yuan, L., Cai, P., Jiang,X., Geibert, W., Cheng, Y. and Chen, Y., 2023. Precise measurement of 226Ra/230Th disequilibria in deep-sea sediments by high-sensitivity ICP-MS. Chem. Geol., 620, 121351, https://doi.org/10.1016/j.chemgeo.2023.121351.

Yusuf, D.B., 2016. Ground Radiometric Investigation in the Southern Part of the Kerri–Kerri Formation, Gombe State, Northeastern Nigeria. PhD thesis, School of Postgraduate Studies, Ahmadu Bello University, Zaria, Nigeria

Zhou, S., Chu, X., Cao, S., Liu, X. and Zhou, Y., 2020. Prediction of the ground temperature with ANN, LS-SVM and fuzzy LS-SVM for GSHP application. Geothermics, 84 (January), 101757.

Received on: 18-1-2024 ; Revised on: 02-3-2024; Accepted on: 04-03-2024

J. Ind. Geophys. Union, 28(2) (2024), 99-107

Comparison of characteristics associated with super cyclonic storm 'Amphan' using numerical model WRF-ARW analysis and ERA5 reanalysis

Arun Kumar[1], Sushil Kumar[2*], Nagendra Kumar[3], Nitin Lohan[4] and R. Bhatla[5]

[1,3]Department of Mathematics, M.M.H. College, Ghaziabad 201001, India.
[1,2,4]Department of Applied Mathematics, Gautam Buddha University, Greater Noida 201312, India.
[5]Department of Geophysics, Institute of Science, Banaras Hindu University, Varanasi 221005, India.
[*]Corresponding author: sushil.kumar@gbu.ac.in

ABSTRACT

The numerical simulation is performed to study the super cyclonic storm (SuCS) 'Amphan' by using the advanced research weather research and forecasting (WRF-ARW) model with 9 km resolution and in single domain while running WRF Pre Processing System (WPS) over the Bay of Bengal (BoB). The super cyclonic storm (SuCS) 'Amphan' originated over south Andaman Sea, which touched southeast BoB on 13th May 2020. The super cyclonic storm (SuCS) 'Amphan' underwent rapid intensification into a very severe cyclonic storm (VSCS) on 17th May 2020 and subsequently converted into extremely severe cyclonic storm (ESCS) on 18th May 2020 and finally into a super cyclonic storm (SuCS) around 1200 UTC of 18th May 2020 till next 24 hours, before weakening into ESCS and laid down as a low-pressure region over north Bangladesh and neighbourhood around mid-night of 21st May 2020. In this study, high resolution advanced research weather research and forecasting (WRF-ARW v4.1.2) with the combination of the Yonsei University (YSU) planetary boundary layer (PBL), Kain-Fritsch (KF) cumulus convection, and Ferrier microphysics scheme, is used for the simulation of SuCS 'Amphan'. Spatial distribution of wind, potential vorticity (PV), and vertical integrated moisture transport (VIMT) are analysed for the intensity and the behaviour of the characteristics of SuCS 'Amphan'. Fifth generation of European center for medium-range weather forecast (ECMWF) atmospheric reanalysis of global climate (ERA5) resolves the atmosphere with 137 levels from the surface at the height of 80 km. ERA5 gives hourly estimations of a big number of atmospheric variables and covers the Earth on a 31 km grid. ERA5 observations are used for the validation of WRF-ARW model results. It is observed that spatial distribution of wind and vertical integrated moisture transport (VIMT), are well matched with the observations. The study is a prelude for sensitivity analysis and data assimilation using four-dimensional variational data assimilation (4DVAR) technique.

Keywords: WRF-ARW Model, Tropical cyclone, Bay of Bengal, Super Cyclonic Storm (SuCS) Amphan, ERA5 Reanalysis.

INTRODUCTION

The Bay of Bengal (BoB) and Arabian sea (AS) are contributing almost seven percent of entire tropical cyclones (TCs) around the world (IMD Atlas, 2008). According to Indian Meteorological Department (IMD), tropical cyclones (TCs) over Bay of Bengal (BoB) are more frequently occurring than tropical cyclones (TCs) over Arabian sea (AS) (WMO, 2008). Every year tropical cyclones (TCs) are originating in North Indian Ocean (NIO) ranging in various categories and some of them are very much harmful for loss of life and economy of the larger area of Indian states. These tropical cyclones (TCs) are influenced by the bathymetry, and dynamical characteristics over North Indian Ocean (NIO), socio economic conditions, and dense population. The non-landing tropical cyclones (TCs), in general, are more frequent than landfalling tropical cyclones (TCs) over the Bay of Bengal. 8 cases of 10 highly severe tropical cyclones (TCs) that occurred in different part of world were from the Bay of Bengal (BoB) and Arabian sea (AS) (IMD Atlas, 2008). The simulation of the tropical cyclones (TCs) using mesoscale model is a necessary aspect to analysis of various parameters associated with the prediction of tropical cyclones (TCs). Therefore, the advanced research weather research and forecasting (WRF-ARW) model is used to study various parameters. The WRF-ARW model refers to the weather research and forecasting (WRF) model with the advanced research weather research and forecasting (WRF) dynamical core. This version of the weather research and forecasting (WRF) model uses a more advanced set of equations and algorithms for atmospheric simulations, allowing for high-resolution and accurate weather forecasting. The comparison of the results WRF-ARW model and fifth generation of European center for medium-range weather forecast (ECMWF) atmospheric reanalysis of global climate (ERA5) reanalysis datasets are also shown in this study. Various global and mesoscale models e.g WRF-ARW model and, fifth generation of European center for medium-range weather forecast (ECMWF) atmospheric reanalysis of global climate (ERA5) reanalysis datasets, have been developed to improve at least 48 hours tropical cyclones TCs track prediction, intensity, and precipitations (Gupta, 2021). Many attempts have been made to improve performance of the model through nested domains, improving initial and boundary conditions (IBCs), and physical parameterizations, etc. Ooyama, (1969) simulated the life of tropical cyclones and discussed the basic mechanism of tropical cyclones (TCs). A cumulus parameterization (CP) scheme is studied to parametrize the convection in the models. Cumulus convection is an important factor in the progress and strengthening of tropical cyclones (TCs) (Anthes, 1977). Kain and Fritsch, (1990) have studied the dependency of cumulus parameterization (CP) scheme on the rate of sub grid

precipitation, latent heat release and redistribution of the thermodynamic and dynamic variables. Weisman et al., (1997) found that cumulus parameterization (CP) can be turned off if grid resolution is less than 4 km. They also showed that microphysics scheme can be allowed to resolve cloud and precipitation. In the last twenty-five years, it is observed that all weather forecasting activities are mostly dependent on numerical weather prediction (NWP) models to deliver progressive data of strength and their track due to changing TCs, statistical models and synoptical procedures (Mohanty and Gupta, 1997; Gupta, 2006; Chen et al., 2013; Mohapatra et al., 2013 a,b; Hegde et al., 2016; Routrey et al., 2019). Simulation of tropical cyclone 'Phalin' using WRF model was studied by Kumar et al., (2016). Singh et al., (2021) have studied an enormously severe cyclonic storm (SCS) over the BoB using WRF-ARW model.

Increasing model horizontal resolutions has been shown in several studies to have a favourable effect on tropical cyclone (TC) intensity forecast accuracy (Zhang et al., 2011; Gopalakrishnan et al., 2012). It is therefore anticipated that the forecast of tropical cyclone (TC) structure, and intensity will be improved by the use of a high-resolution modelling system. However, majority of these studies' initial and boundary conditions come from datasets like the Global Forecast System (GFS; $0.5^o \times 0.5^o$ resolution), ECMWF Reanalysis Interim/ERA5 ($0.25^o \times 0.25^o$resolution), and NCEP Final analysis (FNL; $1^o \times 1^o$ resolution). The WRF-ARW model is available with different high-resolution. Therefore, it is critical to assess how well WRF-ARW model output data performs in forecasting severe tropical cyclones over the Bay of Bengal region.

Shenoy et al. (2021) have found that the best configuration for tropical cyclone forecasting over the Bay of Bengal is the combination of the Yonsei University (YSU) planetary boundary layer (PBL), Kain-Fritsch (KF) cumulus convection, and Ferrier microphysics scheme. The sensitivity studies show that the Kain-Fritsch (KF) cumulus parameterization yields the least errors in track (position and time) and intensity predictions when combined with the Yonsei University (YSU) planetary boundary layer (PBL) scheme and Ferrier (new eta) microphysics. Thus, the YSU-KF-Ferrier combo shows precise track and intensity forecasting (Shenoy et al., 2022). In this paper, an experiment is conducted using WRF-ARW model along with the combination of the Yonsei University (YSU) planetary boundary layer (PBL), Kain-Fritsch (KF) cumulus convection, and other fixed suitable options of model's configuration, for SuCS 'Amphan'. The main aim of this paper is to analyse the wind, potential vorticity (PV), and vertical integrated moisture transport (VIMT) for the intensity and the behaviour of the characteristics of SuCS 'Amphan'. The Comparison of SuCS 'Amphan' using WRF model output data parameters with ERA5 model output parameters is also shown.

SUPER CYCLONIC STORM – 'AMPHAN'

SuCS 'Amphan' was shaped over the south Andaman Sea and adjoined south east BoB on 13th May 2020. It started concentrating into a deep depression (DD) over south east BoB on 16th May 2020. It further converted into a severe cyclonic storm (SCS) on 17th May 2020 morning, very severe cyclonic storm (VSCS) on 17th May 2020 afternoon, extremely severe cyclonic storm (ESCS) on 18th May 2020 morning and super cyclonic storm (SuCS) around afternoon of 18th May, 2020.

It intensified into a SuCS and SuCS maintained strength over west central Bay of Bengal (BoB) for almost 24 hours. Around afternoon of 19th May, SuCS started weakening in an ESCS over west central BoB. Therefore, ESCS weakened while crossing west Bengal-Bangladesh coasts as VSCS around Sunderbans during 1530 - 1730 UTC of 20th May with extreme nonstop wind speed 155-165 kmph, gusting to 185 kmph. It laid down over West Bengal as a VSCS on 20th May night. It was very near to Kolkata during this time interval. It kept on moving towards northeast and weakened into SCS over Bangladesh on 20th May mid night. It further weakened into CS on 21st May morning, converted into deep depression (DD) over Bangladesh around 21st May noon in the evening of the same day and into a depression (D) over northern Bangladesh. Around midnight on 21st May, 2020, it further weakened and laid down as a clearly defined low pressure region over north Bangladesh and the surrounding area.

DATA USED

The present study focuses over Bay of Bengal (BoB) region restricted between 78°E-103°E longitude and 4°N-26°N latitude and 9-km horizontal grid resolution (Figure 1). A single domain is used for the model simulation of length 126 hours of the above-mentioned region. The National Centres for Environmental Prediction (NCEP) operational analysis with $1^o \times 1^o$ horizontal resolution is used for initial conditions and boundary conditions to simulate the SuCS 'Amphan.' The Global Forecast System (GFS) is a numerical weather prediction model run by the NCEP. It provides global weather forecasts out to 16 days in advance, covering a wide range of meteorological parameters such as temperature, humidity, wind speed, and precipitation.

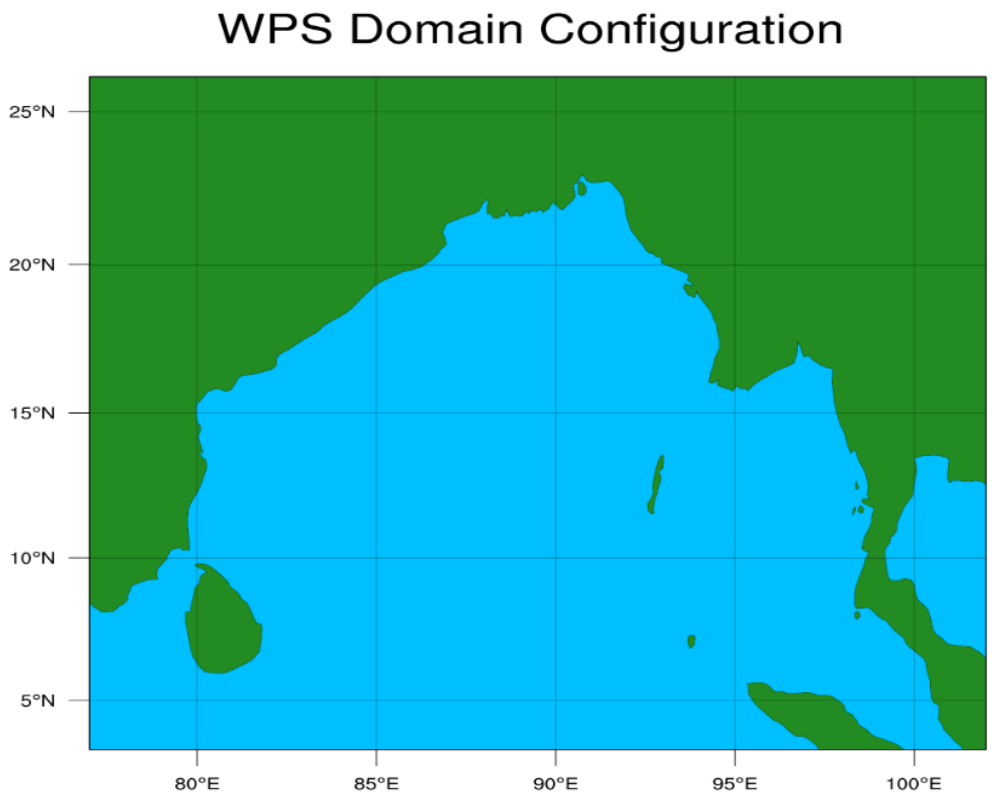

Figure 1. Advanced research weather research forecast (WRF-ARW) model domain for super cyclonic storm (SuCS) 'Amphan' study.

The lateral boundary conditions are downloaded from the NCEP (GFS) forecast fields at every 6 hours interval. ERA5 datasets are used for the validation of the parameters obtained from the model integration. The European Centre for Medium-Range Weather Forecasts (ECMWF) has developed a reanalysis dataset known as ERA5. It provides hourly data with high resolution (around 31 kilometres worldwide) for many different atmospheric variables, such as temperature, humidity, wind speed, precipitation, and surface pressure. In order to ensure accuracy and consistency, ERA5 integrates information from satellites, weather stations, and other sources using sophisticated numerical models and data assimilation techniques. It improves on ERA-Interim, its predecessor, by utilizing better model physics and higher-quality data. To maximize accuracy, configuration entails defining the model resolution, time intervals, parameterization schemes, and assimilation processes.

METHODOLOGY

Non hydrostatic advanced research weather research and forecasting (WRF-ARW) model version 4.1.2 is used for this study. The model is planned to focus on finer horizontal grid lengths of very less kilometres or less with nested domains for prediction and simulation of different good-scale atmospheric phenomena (John et al., 2004; Skamarock et al., 2005)**.** Eulerian mass dynamical core is used to consider the terrain hybrid sigma-pressure vertical coordinates. Runga Kutta 2nd and Runge Kutta 3rd order schemes are applied for time integration and 2nd to 6th order schemes are applied for advection. The model has various parametrization of physical processes, a data assimilation packages, and number of various physics schemes. It has various options for convective parameterization schemes, planetary boundary layer schemes, and microphysics schemes. The detailed model configuration of this study for the SuCS 'Amphan' simulation is given in Table 1.

Vertical integrated moisture flux Q can be expressed as

$$Q = \frac{1}{g}\int_{0}^{p_s} qVdp$$

where V is wind vector, q is specific humidity, p_s is surface pressure, and g is gravitational constant. For vertical integrated moisture transport (VIMT), vertical integration of this equation is carried out from surface pressure (in hPa) to 300 hPa since specific humidity have negligible effect above this level and is not a part of ERA5 reanalysis datasets (Kalnay et al., 1996).

Table 1. Model configuration used in WRF-ARW model

Model Configuration	*Configuration*
	Bay of Bengal
Dynamics	Nonhydrostatic
Model domain	4°N-26°N, 78°E-103°E
Domain center	15°N and 89.5° E
Horizontal resolution	9km
Map projection	Mercator
Grid scheme in horizontal	Arakawa C-grid
Time step	40s
Vertical coordinates	Hydrostatic pressure vertical coordinate with 51 pressure levels
Time integration schemes	3rd order R-K Scheme
Spatial differencing scheme	Center differencing (6th order)
Micro physics	Ferrari (5)
Radiation schemes (ra_lw_physics & ra_sw_physics)	RRTM Scheme for long wave/ Dudhiya for short wave
Surface layer parameterization (sf_surface_physics)	Thermal diffusion scheme
Planetry boundary layer physics (bl_pbl_physics)	Yonsei University (YSU)
Cumulus scheme (cu_physics)	Kain Fritsch Scheme

RESULTS AND DISCUSSION

The results obtained using advanced research weather research and forecasting (WRF-ARW) model with 9 km resolution in a single domain over Bay of Bengal (BoB) are discussed below. The parameters viz spatial distribution of wind, potential vorticity (PV), and vertical integrated moisture transport (VIMT) are analysed and validated with fifth generation of European center for medium-range weather forecast (ECMWF) atmospheric reanalysis of global climate (ERA5) reanalysis datasets.

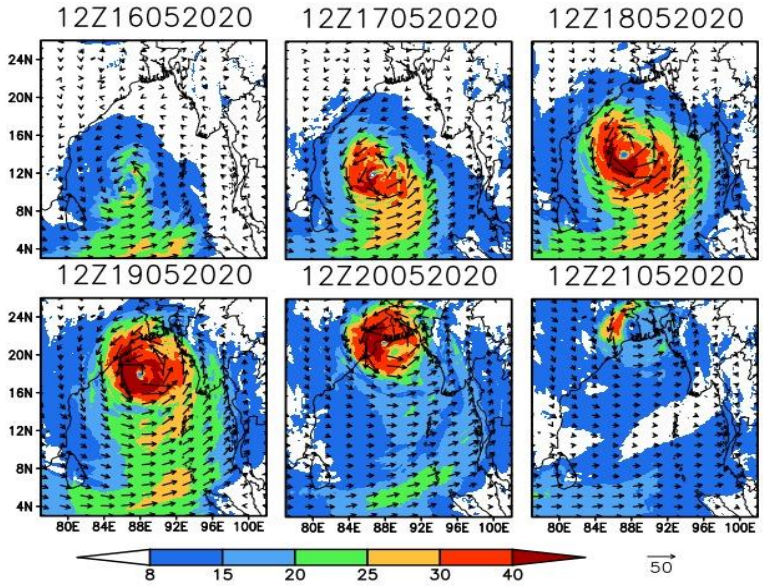

Figure 2. Pattern of wind flow (m/s) at 850 hPa from pre- to post- landfall (16 May 2020 - 21 May 2020) using advanced research weather research forecast (WRF-ARW) model experiment data.

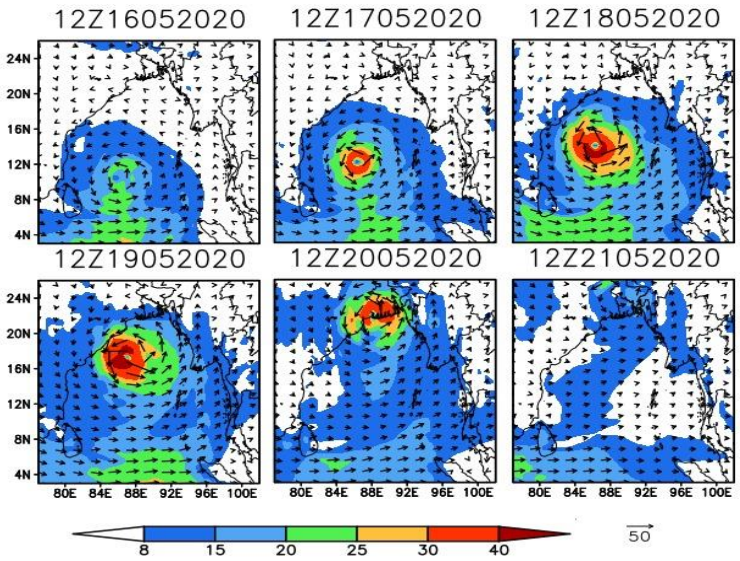

Figure 3. Pattern of wind flow (m/s) at 850 hPa from pre- to post- landfall (16 May 2020-21 May 2020) using ERA5 data.

Simulation of wind

Wind plays an important role in the dynamics of a tropical cyclone. Accurate wind pattern forecast is essential to minimise damage. Figure 2 depicts the low-level wind flow distribution (in m/s) at 850 hPa as simulated by the WRF-ARW model for SuCS 'Amphan'. Figure 3 depicts the low-level wind at 850 hPa from ERA5 reanalysis datasets. In Figure 2, the model-simulated wind flow pattern, valid for 1200 UTC of May 16-21, 2020, based on the initial and boundary conditions at 1200 UTC on May 16, 2020. The model depicts a well-organized cyclonic circulation, characterized by strong winds encircling the center. Notably, the model accurately captured the maximum wind speed, reaching approximately 50 m/s, which closely matched with the ERA5 reanalysis datasets maximum wind speed. From all the figures, it is observed that the wind flows concentrated into DD of cyclone on 16th May 2020 1200 UTC, SCS converted into VSCS on 17th May 1200 UTC, VSCS converted into SuCS on 18th May 1200 UTC, SuCS weakening into an ESCS on 19th May noon, just before crossing west Bengal- Bangladesh coasts on 20th May 1200 UTC, and DD over Bangladesh on 21st May 2020.

It is observed from both data sets that the circulation of wind started on 16th May 2020 and moved towards west Bengal with higher magnitude of wind till 19th May 2020 and then started weakening around afternoon of 19th May. It can also be observed from Figure 2 that cyclone eye started developing on 17th May 2020 and started moving towards north eastwards. Cyclone eye is fully developed on 18th - 19th May 2020, with maximum speed around 50 m/s and touched west Bengal nearby Kolkata. Cyclone eye keeps moving towards Bangladesh and started weakening during 20th -21st May. In this analysis, the pattern of wind observed from ERA5 re-analysis is quite similar to wind observed from model, but the intensity of wind is lower than the model wind intensity. WRF-ARW captures high speed of wind than ERA5. It may be because of low resolution of ERA5.

Potential vorticity analysis

The analysis of potential vorticity (PV) at 500 hPa from WRF-ARW and ERA5 reanalysis datasets during 16th May 2020 to 21st May 2020 is shown in Figures 4 and 5 respectively. The gradual increase of intensity of the PV is noticed from initial phase to established phase around inner region of the SuCS 'Amphan'. The distribution of high value of PV (greater than and equals to 3.0 PVU where, 1PVU equals to 10^{-6} K. $m^2.kg^{-1}.s^{-1}$) is captured by WRF-ARW model in SuCS 'Amphan' inner region. The maximum PV region intensified the movement of cyclonic structure. At the same time, near the southwest portion of the cyclonic disorder, the low PV is noticed. This dynamical discrepancy provides a perfect condition for a powerful moisture fluxes carriage (Figure 6) from domain region into the internal storm's core neighbourhood. The analysis showed visible band type shaped PV near the storm. Therefore, potential vorticity (PV) value rises till 19th May 2020 afternoon. Similar pattern of PV is also foreseen near the SuCS 'Amphan' by the ERA5 reanalysis datasets during cyclone cycle, although, the intensity of this pattern is low in ERA5 reanalysis datasets.

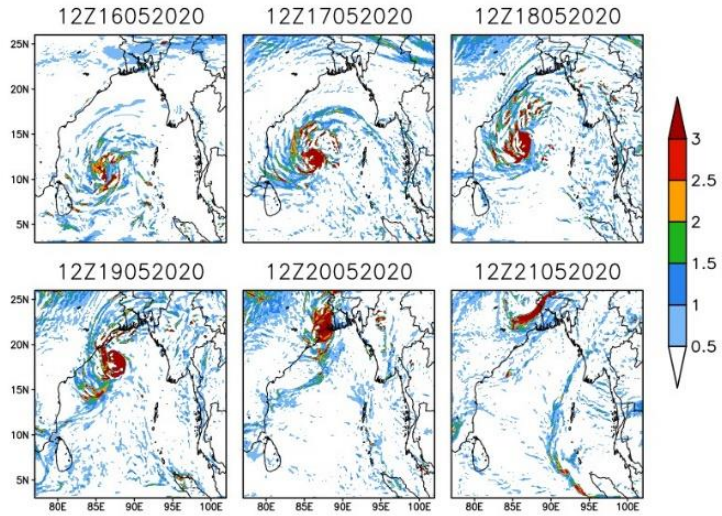

Figure 4. Potential vorticity at 500 hPa from pre- to post- landfall (16 May 2020–21 May 2020) using advanced research weather research forecast (WRF-ARW) model experiment data.

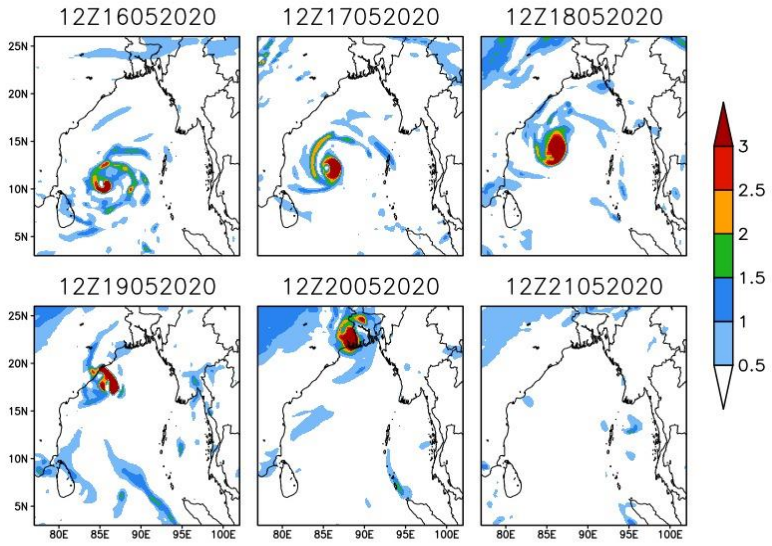

Figure 5. Potential vorticity at 500 hPa from pre- to post- landfall (16 May 2020–21 May 2020) using ERA5 data.

Vertical integrated moisture transport (VIMT)

Figures 6 and 7 depict the spatial spreading of vertical integrated moisture transport (VIMT) and VIMT magnitude (kg. m^{-1}. s^{-1}) from WRF-ARW output and ERA5 reanalysis datasets during 16th May 2020 to 21st May 2020. A wide role in the tropical cyclone (TC)'s development and intensity is contributed by the latent heat (Hill and Lackmann, 2009; Huang et al.,2014; Makarieva et al., 2017; Fujiwara et al., 2017).

Latent heat is often transferred by moisture transport in th e SuCS 'Amphan' system. In WRF-ARW on 16th May at 1200 UTC (Figure 7), at the initial phase of the tropical cyclone (TC) system, the moist northeast flowing around the Indian ocean is clearly observed. From 16th May 2020 1200 UTC to 19th May 2020 1200 UTC (Figure 7), the eastward transportation of humidity is progressive over Bay of Bengal (BoB) north east region. The moisture in north-eastward is constantly mixing near SuCS 'Amphan' over domain region. Hence, the system is well connected with the increased moisture so that this increment in moisture results a moisture conveyor belt (MCB) formation over the region. A well-marked low pressure (WML) system was established on 17th May 1200 UTC as reported by ERA5 reanalysis datasets.

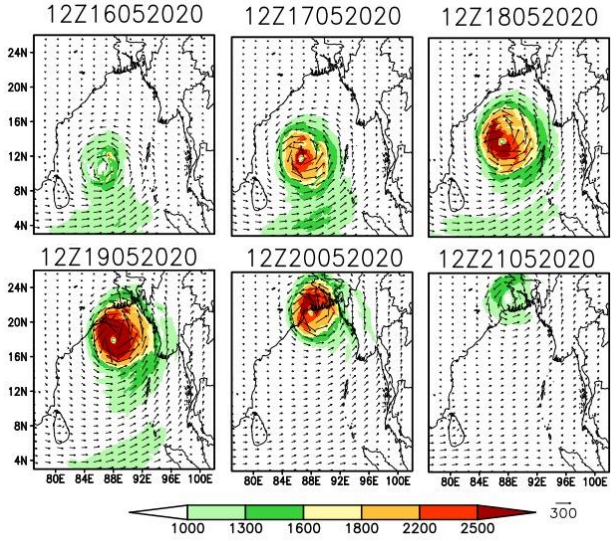

Figure 6. Vertical integrated moisture transport (VIMT) at different stages from pre- to post- landfall (16 May 2020–21 May 2020) using advanced research weather research forecast (WRF-ARW) model experiment data.

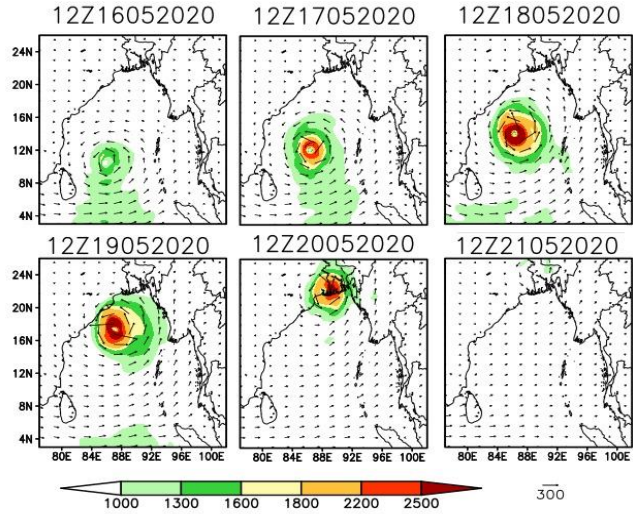

Figure 7. Vertical integrated moisture transport (VIMT) at different stages from pre- to post- landfall (16 May 2020–21 May 2020) using ERA5 data.

In the Figure 7, on 19th May, 2020 1200 UTC the WML system is observed. The intensity of storm from DD to CS started increasing during the period 16th to 17th May, 2020 (Figure 7) and moved north-eastward over the northeast Bay of Bengal (BoB) adjoining Bangladesh. The cyclonic storm (CS) moved over the north-eastward region. In the inner area of the cyclonic arrangement, there is a large-scale transportation of moisture from the ocean by moisture conveyor belt (MCB). This large-scale moisture transport increased the intensity of the tropical cyclones (TCs) as more than 550 kg. $m^{-1}.s^{-1}$ absolute value of moisture fluxes is taken back by the moisture conveyor belt (Fujiwara et al., 2017; Kudo et al., 2014; Takakura et al., 2018). The progress of the SuCS 'Amphan' is steady and shown in all the model analysis (Figure 6). The absolute value of VIMT and MCB pattern of WRF-ARW model are significantly matched with the ERA5 reanalysis (Figure 7; 18th – 20th, 2020). The model forecasts are successfully reproduced above mentioned characteristics observed in the ERA5 reanalysis datasets.

The shape and development of the SuCS 'Amphan' are also observed on 17th -18th May, 2020 and both are also very clearly matched with ERA5 reanalysis datasets. The model predicted moisture conveyor belt (MCB) time evolution considerably fine. Hegde et al. (2016), Fujiwara et al. (2017) and Makarieva et al. (2017**)** simulated similar features of VIMT through regional atmospheric models over South

China sea and Indian ocean. The moisture conveyor belt (MCB) development is an important aspect for the moisture import inside system core from the remote oceans. This development of moisture conveyor belt (MCB) subsequently increases the latent heat which cause the increase in storm intensity. The storm intensification progressd consequent to additional moisture conveyor belt (MCB) development. The absolute value of VIMT of the SuCS 'Amphan' is more than 950 kg. $m^{-1}.s^{-1}$ and it is higher than the ERA5 reanalysis datasets over SuCS 'Amphan' surrounding and inner region. Therefore, the time evolution of large-scale vapour transportation is predicted well by the high resolution WRF-ARW model during SuCS 'Amphan' initial stage.

CONCLUSIONS

This study investigated the predictive ability in terms of different parameters viz, spatial distribution of wind, potential vorticity (PV), and vertical integrated moisture transport (VIMT) of advanced research weather research and forecasting (WRF-ARW) model, during the developing features connected with the super cyclonic storm (SuCS) 'Amphan' over BoB from 16^{th} – 21^{st} May, 2020. The wind field using model simulation at 850 hPa shows that cyclonic rotation increases with the increase in simulation lengths. The model simulated wind field shape is quite matched with the ERA5 re-analysis shape during the simulation length. The intensity of model simulated potential vorticity (PV) growing around the inner part of super cyclonic storm (SuCS) 'Amphan' from initial stage of SuCS 'Amphan' to intense stage of SuCS 'Amphan'. The small value of PV is observed in the north east part of the SuCS 'Amphan'. The storm's features are well matched with ERA5 datasets with high PV values, and it keeps tropical cyclone (TC) initial strength and structure during the evolved stage. We also observed response between intensity of the super cyclonic storm (SuCS) 'Amphan' during pre-landfall and moisture transportation over the region of model through vertical integrated moisture transport (VIMT) distribution. It is found from WRF-ARW model results that the moist flows over BoB region are increased with formation of SuCS 'Amphan' and moisture conveyor belt (MCB), formed due to these moist flows over model domain. The intensity of the SuCS 'Amphan' increased due to big scale transportation of moisture inside region of cyclone from the ocean through moisture conveyor belt (MCB). The moisture conveyor belt (MCB) pattern and magnitude of VIMT over Indian ocean are almost correlated with ERA5 reanalysis datasets. The results obtained from WRF-ARW model are in agreement with the previous results from ERA5 reanalysis datasets. It is concluded that the advanced research weather research and forecasting (WRF-ARW) model, can predict all stages of the super cyclonic storm (SuCS) 'Amphan.' Simulations of more tropical cyclones (TCs) with sensitivity analysis and the obtained results, required validation with different source of observations for the support of the conclusions of the present study.

ACKNOWLEDGEMENTS

The authors would like to thank Department of Mathematics, M.M.H. College, Ghaziabad, UP, India, Department of Applied Mathematics, Gautam Buddha University, Greater Noida, UP, India and NCMRWF, Noida, UP, India to provide a good environment, library facility, and their technical support for this research. Authors would like to thank the reviewer for their valuable comments. Additionally, the authors would like to extend their appreciation for the infrastructure support received through the Science and Engineering Research Board, Government of India's sponsored project (SUR/2022/ 005506-G). One of the author NK would like to acknowledge IUCAA, Pune.

Author Credit Statement

Mr. Arun Kumar, and Dr. Sushil Kumar carried out all the experiments, conceptualise it and designed the study, besides data acquisition, analysis, interpretation of data and writing of the paper. Prof. Nagendra Kumar substantially contributed in conceptualisation and revision of the manuscript. Mr. Nitin Lohan customized the model and analysed the results., Prof. Rajeev Bhatla analysed the results.

Data Availability

ERA5 is a gridded hourly data which is available on pressure level at

https://cds.climate.copernicus.eu/cdsapp#!/dataset/reanalysis-era5-pressure levels?tab=overview and ERA5 hourly data on single level is available on

https://cds.climate.copernicus.eu/cdsapp#!/dataset/reanalysis-era5-single evels?tab=overview. In this research, access to NCEP data was facilitated through the following site https://rda.ucar.edu/datasets/ds351.0/dataaccess/.

Compliance with Ethical Standards

The authors declare that they have no conflict of interest and adhere to copy right norms.

REFERENCES

Anthes, R. A., 1977. Hurricane model experiments with a new cumulus parameterization scheme. Monthly Weather Review, 105(3), 287–300.

Chen, G., Yu, H., Cao, Q. and Zeng, Z., 2013. The performance of global models in TC track forecasting over the western North Pacific from 2010 to 2012. Tropical Cyclone Research Review, 2(3), 149–158.

Fujiwara, K., Kawamura, R., Hirata, H., Kawano, T., Kato, M. and Shinoda, T., 2017. A positive feedback process between tropical cyclone intensity and the moisture conveyor belt assessed with Lagrangian diagnostics. JGR Atmospheres, 122, 12502–12521.

Gopalakrishnan, S. G., Goldenberg, S., Quirino, T., Zhang, X., Marks, F., Yeh, K. S. and Tallapragada, V., 2012. Toward improving high-resolution numerical hurricane forecasting: Influence of model horizontal grid resolution, initialization, and physics. Weather and Forecasting, 27(3), 647-666.

Gupta, A., 2006. Current status of tropical cyclone track prediction techniques and forecast errors. Mausam, 57, 151–158.

Gupta, A., 2021. Current status of tropical cyclone track prediction techniques and forecast errors. Mausam, 57, 151-158.

Hegde, A. K., Kawamura, R. and Kawano, T., 2016. Evidence for the significant role of sea surface temperature distributions over remote tropical oceans in tropical cyclone intensity. Climate Dynamics, 47, 623–635.

Hill, K.A. and Lackmann, G. M., 2009. Influence of Environmental Humidity on Tropical Cyclone Size. Monthly Weather Review, 137, 3294–3315.

Huang, H. L., Yang, M. J. and Sui, C. H., 2014. Water budget and precipitation efficiency of Typhoon Morakot (2009). J. Atmospheric Sci., 71(1), 112–129.

IMD Atlas, 2008. Tracks of storms and depressions in the Bay of Bengal and Arabian sea. India Meteorological Department, New Delhi, India.

John, M., Dudhia, J., Gill, D., Henderson, T., Klemp, J. et al., 2004. The Weather Research and Forecast Model: Sofware Architecture and Performance. Conference: 11th ECMWF Workshop on the Use of High Performance Computing In Meteorology, 25, 156-168.

Kain, J. S. and Fritsch, J. M., 1990. A One-Dimensional Entraining/Detraining Plume Model and Its Application in Convective Parameterization. J. Atmospheric Sci., 47(23), 2784-2802.

Kalnay, E., Kanamitsu, M., Kistler, R., Collins, W., Deaven, D., Gandin, L. and Iredell, M., 1996. The NCEP/NCAR 40-Year Reanalysis Project. Bull. American Meteorological Society, 77(3), 437-472.

Kudo, T., Kawamura, R., Hirata, H., Ichiyanagi, K., Tanoue, M. and Yoshimura, K., 2014. Large-scale vapor transport of remotely evaporated seawater by a Rossby wave re sponse to typhoon forcing during the Baiu/Meiyu season as revealed by the JRA-55 reanalysis. JGR Atmospheres, 119(14), 8825–8838.

Kumar, S., Routray, A., Tiwari, G., Chauhan, R. and Jain, I., 2016. Simulation of Tropical Cyclone 'Phailin' Using WRF Modeling System. Tropical Cyclone Activity over the North Indian Ocean, Springer, 291-300.

Makarieva, A. M., Gorshkov, V. G., Nefiodov, A. V., Chikunov, A. V., Sheil, D., Donato Nobre, A. and Li, B. L., 2017. Fuel for cyclones: the water vapor budget of a hurricane as dependent on its movement. Atmospheric Res., 193, 216–230.

Mohanty, U. C. and Gupta, A., 1997. Deterministic methods for prediction of tropical cyclone tracks. Mausam, 48(2*)*, 257-272.

Mohapatra, M., Bandyopadhyay, B. K. and Nayak, D. P., 2013a. Evaluation of operational tropical cyclone intensity forecasts over north Indian Ocean issued by India meteorological department. Natural Hazards, 68, 433–451.

Mohapatra, M., Nayak, D. P., Sharma, R. P. and Bandyopadhyay, B. K., 2013b. Evaluation of official tropical cyclone track forecast over north Indian ocean issued by India meteorologycal department. J. Earth Syst. Sci., 122, 589–601.

Ooyama, K., 1969. Numerical Simulation of the Life Cycle of Tropical Cyclones. J. Atmospheric Sci., *26*(1), 3-40.

Routray, A., Dutta, D., and George, J. P., 2019. Evaluation of track and intensity prediction of tropical cyclones over North Indian Ocean using NCUM globalmodel. Pure Appl. Geophys., 176, 421–440.

Shenoy, M., Raju, P. V. S. and Prasad, J., 2021. Optimization of physical schemes in WRF model on cyclone simulations over Bay of Bengal using one-way ANOVA and Tukey's test. Scientific Reports, 11(1), 2045-2322.

Shenoy, M., Raju, P.V.S., Prasad, V.S. and Hari Prasad, K.B.R.R., 2022. Sensitivity of physical schemes on simulation of severe cyclones over Bay of Bengal using WRF-ARW model. Theoretical and Appl. Climatology, 149, 1-15. doi:10.1007/s00704-022-04102-8

Singh, K. S., Albert, J., Prasad K.B. and Alam, P., 2021. Numerical simulation of an extremely severe cyclonic storm over the Bay of Bengal using WRF modelling system: influence of model initial condition. Modeling Earth Systems and Environment, 7(4), 2741-2752.

Skamarock, W.C., Klemp, J. B., Dudhia, J., Gill, D. O., Barker, D. M., Wang, W. and Powers, J. G., 2005. A description of the advanced research WRF version 2. NCAR technical note.

Takakura, T., Kawamura, R., Kawano, T., Ichiyanagi, K., Tanoue, M. and Yoshimura, K., 2018. An estimation of water origins in the vicinity of a tropical cyclone's center and associated dynamic processes. Climate Dynamics, 50, 555–569.

Weisman, M. L., Skamarock, W. C. and Klemp, J. B., 1997. The Resolution Dependence of Explicitly Modeled Convective Systems. Monthly Weather Rev., 125(4), 527-548.

WMO. Technical Document, 2008. Tropical cyclone operational plan for the Bay of Bengal and the Arabian Sea. Document No. WMO/TDNo. 84, 1.

Zhang, X., Quirino, T., Yeh, K. S., Gopalakrishnan, S., Marks, F., Goldenberg, S. and Aberson, S. H., 2011. Improving hurricane forecasts with high-resolution modeling. Computing in Science and Engineering, 13(1), 13-21.

Received on: 3-8-2023 ; Revised on: 25-2-2024; Accepted on: 28-2-2024

J. Ind. Geophys. Union, 28(2) (2024), 108-118

Identification of potential zones for artificial recharge of groundwater using GIS overlay technique in granitic terrain of Bommala Ramaram and Bhudhaan Pochampally watersheds, Yadadri Bhuvanagiri district, Telangana state (India)

G. Praveen Kumar[1] and Sreenu Kunsoth[2*]
[1]Central Groundwater Board, Ministry of Jal Shakti, Faridabad, Haryana- 121001, India
[2]Department of Geology, University College of Science, Osmania University, Hyderabad-500007, India
* *Corresponding author*: sreenukunsoth@osmania.ac.in

Abstract

The study area encompasses an area of 657 Sq. km, along the eastern peri-urban boundary of Greater Hyderabad Municipal Corporation. It is traversed by Musi River in the southern region. The area is underlain by granitic rocks of Archaean age, which have negligible to poor primary porosity while secondary structures like joints, fractures, shears and faults give rise to secondary porosity. The climate of the area is tropical to semiarid with normal annual rainfall of 730 mm. Excess pumping of groundwater for irrigation purposes, has imposed stress on the ground water resources in the northern parts of the study area, where deeper water levels are recorded up to 44 mbgl. Based on the post-monsoon water levels, the average unsaturated thickness estimated 3 mbgl is 5 m. which has a storage capacity of 60 MCM. Effective management of aquifer recharge is becoming an increasingly imperative in the context of water resource management strategies. In this study, Artificial recharge zones have been delineated through the integration of various thematic layers in the GIS environment. Weighted Index Overlay Analysis (WIOA) in spatial analysis is a simple and straight forward method for a combined analysis of multi-class layers. The study involves the mapping of potential zones and finding out various key frameworks influencing selection of suitable structures for artificial recharge of groundwater in granitic terrain using Geographical Information System (GIS) overlay technique. Based on the present study, the area is classified into three different categories of potential zones for artificial recharge namely, high favourable zone, moderate favourable zone and least favourable zone. The high favourable zone occupies 29% of the study area mostly in the northern part, while moderate favourable zones occupy 63% and low favourable zone, 8% occupying hilly areas in both the watersheds

Key Words: GIS, Potential zones, Artificial recharge, Archean granite, Bommala Ramaram, Bhudhaan Pochampalli, Bibinagar (Bhuvanagiri Yadadri district)

INTRODUCTION

With more than 70% of India's population dependent on agriculture, overexploitation of groundwater is an important factor leading to groundwater depletion. Nowadays, groundwater is being depleted not only in India but worldwide, and there is no adequate compensation for it. Therefore, this scarce situation indicates the importance of groundwater resources and its management in a water deficit region. Hence, it is essential to adopt important practices for groundwater augmentation for agricultural, industrial and domestic purposes. Artificial recharge is an effective technique for augmenting groundwater resources. The saturated zone of groundwater present below the Earth surface is termed as aquifer. Generally, aquifers are porous and permeable Identifying potential zones for artificial recharge of groundwater is an important aspect thus becoming increasingly important in water resource management strategies (Gale, 2005). Present study area is devoid of perennial water sources like rivers, lakes etc.

STUDY AREA

The study area includes two watersheds namely, Bommala Ramaram and Bhudhaan Pochampally in Yadadri Bhuvanagiri district, Telangana state (Figure 1) which lies between 17° 14´ 51´´ - 17° 41´ 34´´ N and 78° 40´ 05´´- 78° 55´ 49´´E. The area is located along the eastern peri-urban boundary of Greater Hyderabad Municipal Corporation (GHMC), extending far over 657 Sq.km.

GEOLOGY AND LITHOLOGY

The area under study forms a part of the eastern Dharwar craton located within the state of Telangana. It consists granitoid rocks of the Peninsular Gneissic Complex which are generally massive, occasionally foliated and rarely gneissic. The rocks are leucocratic showing light grey to greyish pink in colour. The rock types occurring in the study area are broadly classified into three groups (Janardhan Rao, 1965; Janardhan Rao and Sitaramayya, 1968). Peninsular granites form first two groups of rocks which include grey and pink varieties of granites and intrusive dolerite dykes comprise the third group (Figure 2). The variations in the granites are quite clear having two major types. Each one of them shows several minor variations which are mainly due to mineralogical composition, textural identities, coarse to medium grained fabric and enclaves. Aplites, pegmatites, epidote veins and quartz veins are also responsible for lithological variations. The dolerite dykes varies both in width and length. All these variations exert considerable influence on weathering and consequent evolution of land forms. Black soils covering majority of the area may have been derived from grey granites.

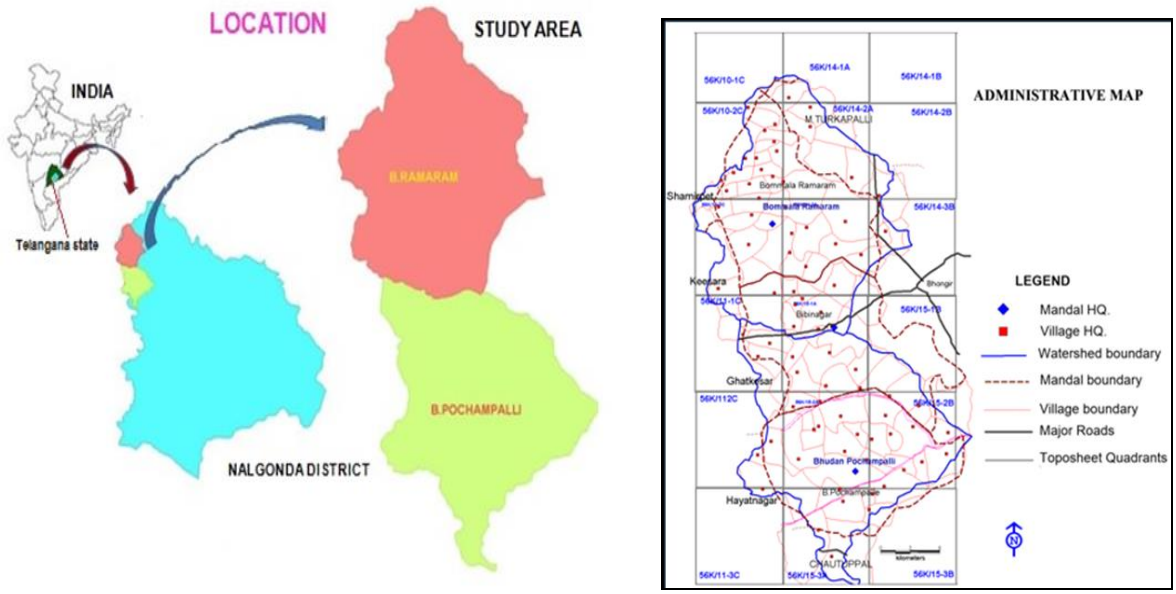

Figure 1. Location map of the study area

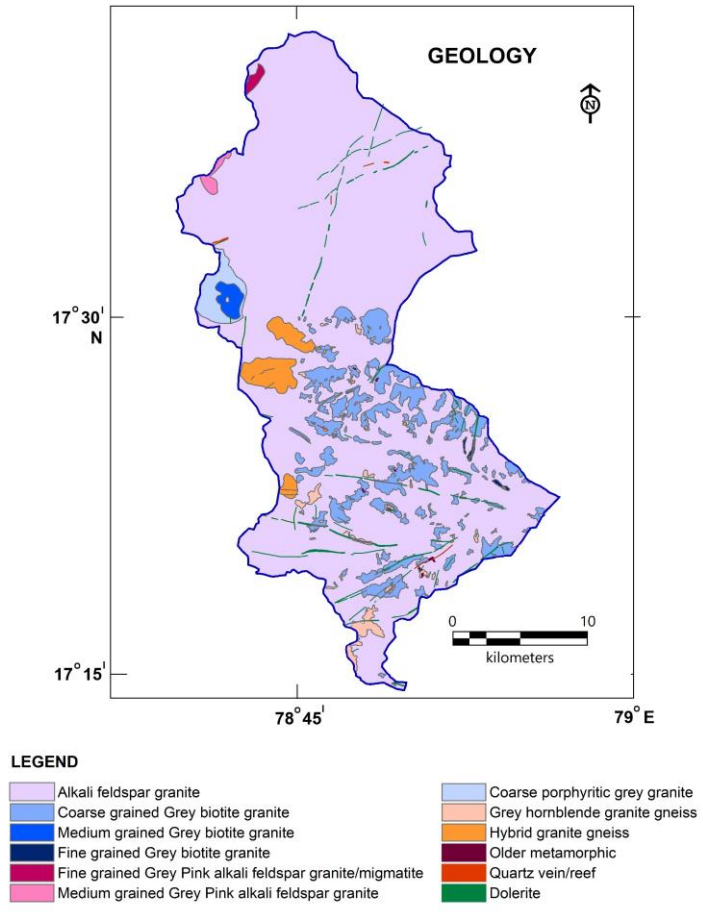

Figure 2. Geology of the study areas covering Bommala Ramaram and Bhudaan Pochampalli watersheds in Yadadri Bhuvanagiri district, Telangana state

Stratigraphic succession

The stratigraphic sequence in the study area ranges from Archaean to recent, as given in Table 1

Structural Features

The rock formations in the study area are devoid of primary porosity. Secondary structures like faults, joints, cleavage fractures, lineation and foliation serve as means for induced porosity for groundwater. The granitic rocks exhibit three sets of criss-cross joints, cut at right angles to each other. The trend of main structural features is NNW-SSE and the alignment of bed rock exposures mainly follows the same trend. The two trends NNW-SSE and E-W are well displayed in the study areas (Figure 3).

HYDROGEOLOGY

The principal water bearing formation in the area is granite. The depth, degree and the lateral extent of weathering in these rocks varies widely from place to place. The weathered thickness varies from 3.0 m. to 25.0 m. The depth to water level varies from 1.05 m to 44.50 mbgl with an average of 16.10 mbgl in pre-monsoon (May) and 0.5 m to 34.82 mbgl with an average of 7.15 mbgl in Post-monsoon (November) (Figures 4 and 5). Shallow (<5 mbgl) are mostly seen in the southern parts of the study region falling in Bhudaan Pochampalli watershed and deeper water levels (> 20 mbgl) are mostly seen in the northern parts in Bommala Ramaram watershed.

Table 1. Lithology of the study Area (Janardhan Rao and Sitaramayya, 1968).

Lithology	*Stratigraphic sequence*	*Stratigraphic horizon*
Weathered zone	Recent	Soils and alluvium
Quartz reefs	Pleistocene	Quartz veins, xenoliths and enclaves
Dykes	Archaean unclassified crystalline rocks	Porphyritic type, fine grained type leucocratic type, mesocratic type melanocratic type, coarse grained to fine grained gneissic type.
Pink granites		
Grey granites		
Basic enclaves		
Peninsular Gneissic Complex		

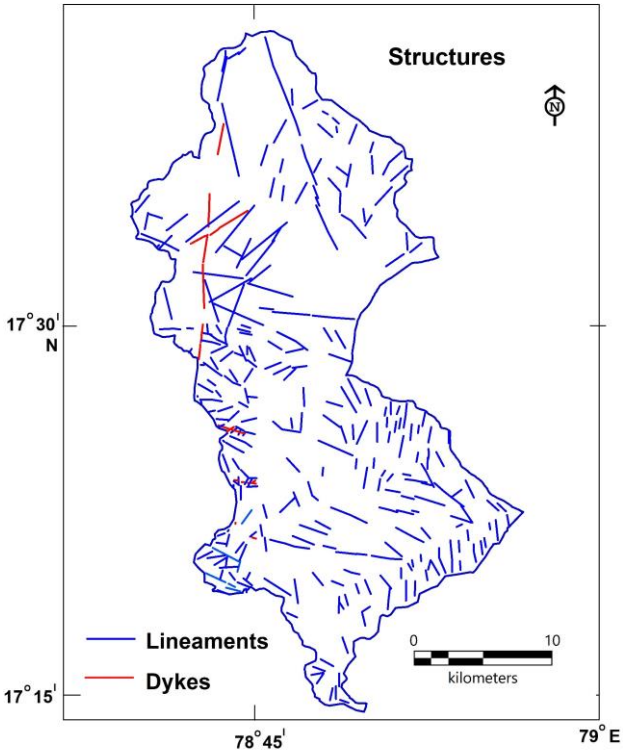

Figure 3. Structural features in the study areas covering Bommala Ramaram and Bhudaan Pochampalli watersheds of Yadadri Bhuvanagiri district, Telangana state

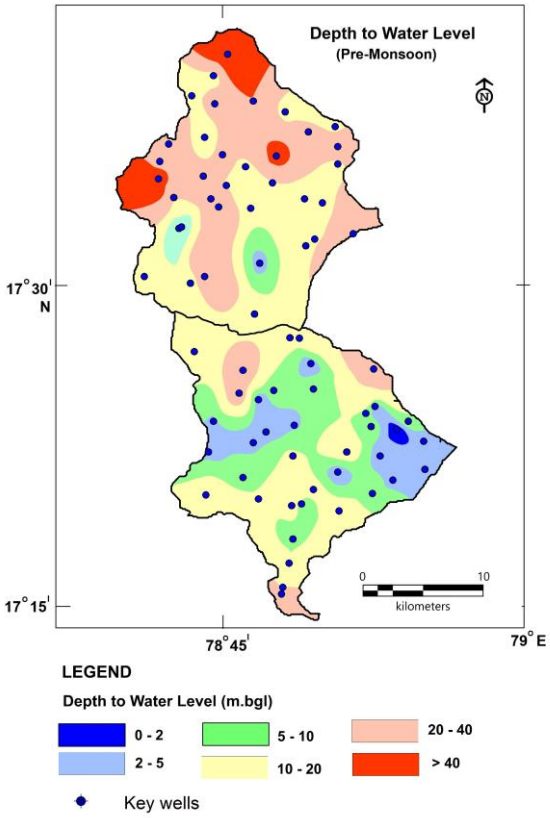

Figure 4. Pre-monsoon depth to water level

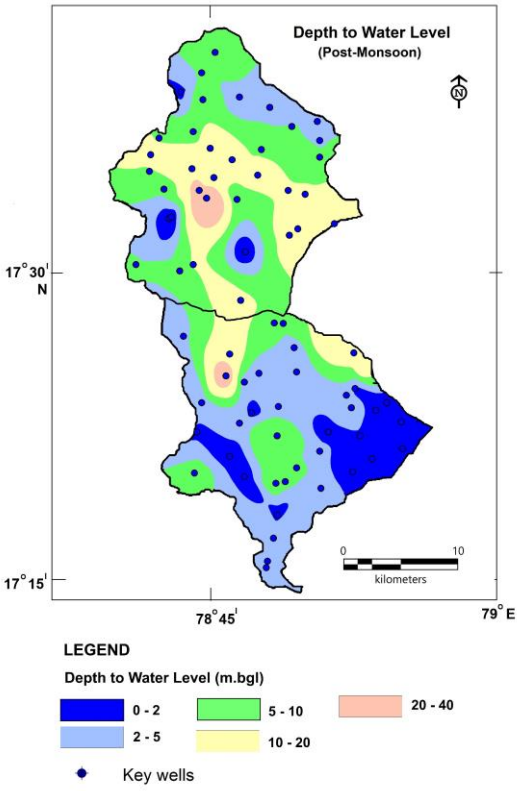

Figure 5. Post-monsoon depth to water level

METHODOLOGY

The methodology for the present research includes fieldwork, data generation of thematic layers and integration of geological and hydrological parameters of the study area by weighted overlay analysis for identifying suitable artificial recharge zones. Landsat-8 image was used to prepare lineament, geomorphology and land use/cover map. Drainage density and slope map is developed from ASTER DEM. Thematic layers are edited in raster format and weightage is assigned to each thematic layer map. The thematic layers are integrated through weighted overlay analysis and the output map generated with potential zones for artificial recharge of groundwater.

FEASIBILITY OF ARTIFICIAL RECHARGE

To understand the feasibility of artificial recharge, unsaturated volume of aquifer is estimated by multiplying the area with specific yield and unsaturated thickness (post-monsoon water levels below 3m). The average unsaturated thickness of the aquifer is 5.0 m. The unsaturated volume calculated with 2% specific yield is 60 MCM (45 MCM in Bommala Ramaram and 15 MCM in Bhudaan Pochampalli). The quantity of groundwater available between 0 to 3 mbgl is 2.0 MCM. Based on the unsaturated thickness, 93% of villages in Bommala Ramaram and 61% of villages in Bhudaan Pochampalli watersheds, have scope for artificial recharge and in remaining villages, due to shallow groundwater condition the scope for artificial recharge does not exist (Figure 6).

RESULTS AND DISCUSSION

Delineation of potential zones for artificial recharge

Artificial recharge zones are identified based on integration of the thematic layers in the GIS environment. Weighted Index Overlay Analysis (WIOA) in spatial analysis is a simple and straight forward method for a combined analysis of multi-class layers. Consideration of relative importance between the parameters leads to a better representation of actual ground situation (Chaudhary, 1999). The potential zones for artificial recharge of groundwater are controlled by various factors. Each factor is assigned with a weight depending on its influence on the storage and transmission of groundwater. The area which is categorized as excellent for an artificial recharge zone, possess high storability, deep water table and good water holding capacity for constructing an artificial recharge structure. Eight thematic layers which include geomorphology, slope, soil, drainage density, lineament density, land use/land cover, geology, and groundwater level, are used to identify recharge potential zones. The different units in each theme are assigned a knowledge-based hierarchy of ranking. The parameter wise weightages and ranking of different units of each parameter are given in Table 2.

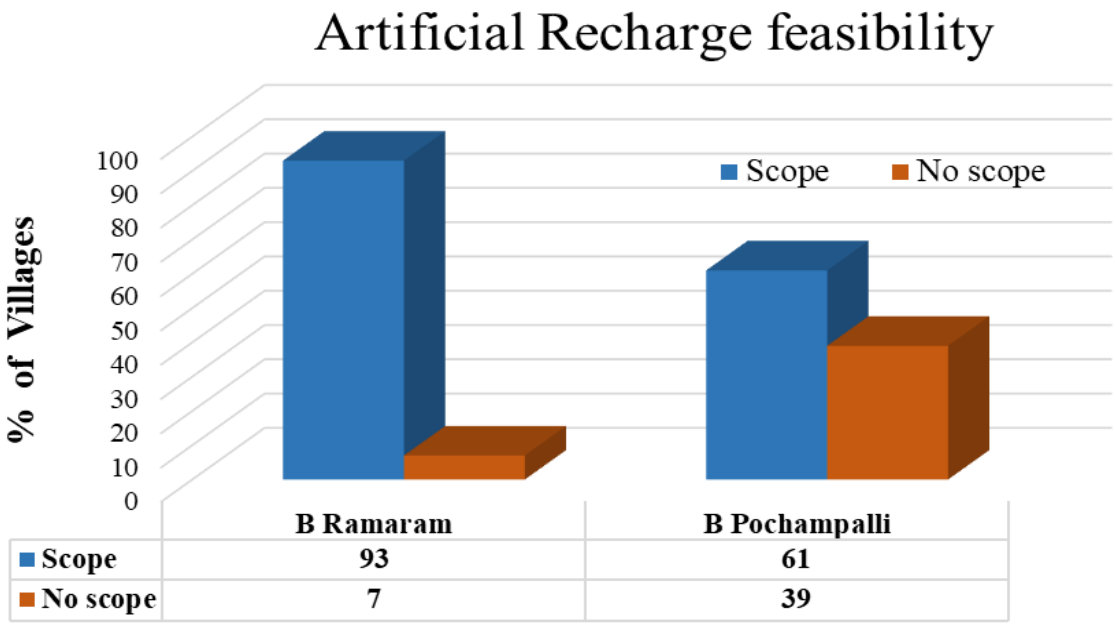

Figure 6. Watershed wise artificial recharge feasibility

Table 2. Assigned weightage and ranking for the delineation of potential zones for artificial recharge in the study area

Layer	*Theme*	*Weightage*	*class*	*Ranking*
1	Geomorphology	30	Flood plain	25
			Pediplain	15
			Structural hills	5
2	Slope	30	0 - 2 %	10
			2 % - 5 %	6
			5 % - 10 %	4
			10 % - 15 %	0
			> 15 %	0
3	Soil	10	Loamy soil	20
			Clayey soil	10
			Rocky outcrop	5
4	Drainage density	5	0 - 2	30
			2 - 4	15
			>4	5
5	Lineament density	20	0 - 1	3
			1 - 2	7
			2 - 3	10
6	Land use/land cover	5	Agricultural land	20
			Buildup land	5
			Forest	10
			Waste land	10
			Water bodies	1
7	Geology	15	Granite	13
8	Depth to water level	20	0 - 4	0
			4 - 8	10
			>8	20

(i) Geomorphology

Lithology and the geomorphology of the area play a prominent role in groundwater recharging (Elango and Mohan, 1997) as the geomorphological units are highly helpful for selecting such sites (Ghayoumian et al., 2007). The study area is classified into various landforms based on geomorphology, such as pediplains, pediments, valley fills, inselbergs etc. These landforms act as groundwater storage reservoirs and some of them act as recharge and run-off zones (Jai Sankar et al., 2001). 63% of the area is covered by pediplains followed by 33% pediment and inselbergs (Figure 7). The parameter wise weightages assigned to geomorphologic units are given in Table 3.

(ii) *Slope*

The slope of an area controls the retention period of surface and ground water within a topographic unit. The steep gradients (>10%) in the runoff zones, such as hill slopes, have very little possibility of infiltration which are suitable only for water conservation measures like gully plugging, bench terracing or contour trenching, aimed at slowing down surface runoff and thereby causing more infiltration. Moderate topographic slopes (1% to 10%) usually occur on valley sides, downward of piedmont foothill regions. These areas are suitable for locating recharge basins and percolation ponds. The broad valley floors occurring along the major rivers may typically have gentle to very gentle gradients, movement of both surface and ground water is sluggish and retention time, in general is high in such areas. Artificial recharge through percolation ponds, recharge pits, trenches and recharge basins are normally feasible (Figure 8).

(iii) *Soil*

Various factors such as the depth of soil profile, its texture, mineral composition and organic content control the infiltration capacity of different kind of soils. Areas having a thin soil cover are easily drained and permit more infiltration when compared to areas with thick soil cover in

the valley zones. Soils having coarser texture due to higher sand-silt ratios, have markedly higher infiltration capacity as compared to clay-rich soils, which are poorly permeable. The role of soil depends on various factors in groundwater recharge, it is given a lower weight, (Saraf and Choudhury, 1998) (Figure 9).

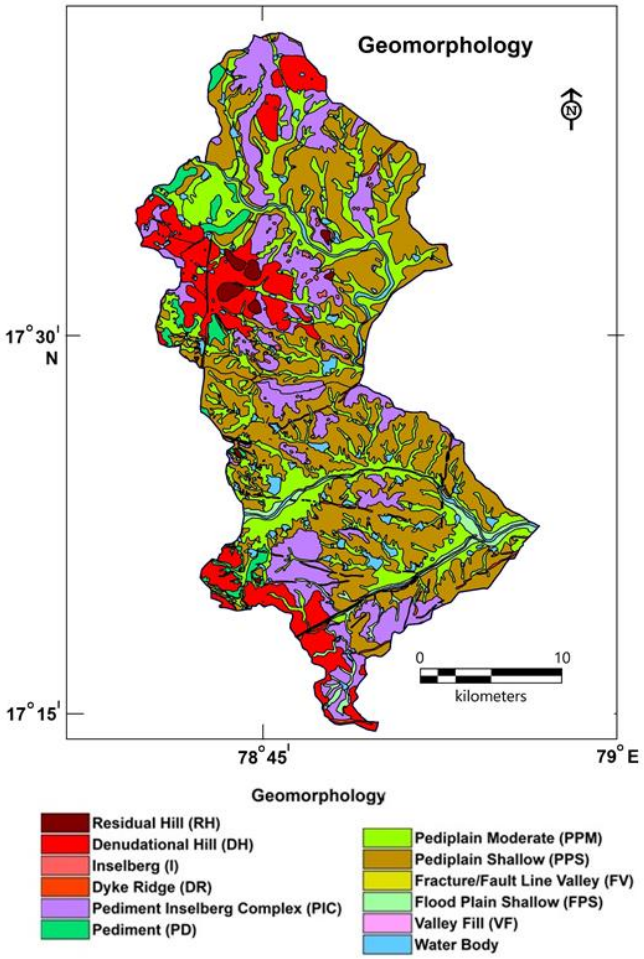

Figure 7. Geomorphological map of the Bommala Ramaram and Bhudaan Pochampalli watersheds in Yadadri Bhuvanagiri district, Telangana state.

Table 3. Assigned geomorphology weightage

Description	*Weight*	*Value*
Pediment	5	150
Linear ridge	5	150
Residual hill	5	150
Denudation hill	5	150
Pediplain	15	450
Channel bar	25	750
Channel fill	25	750
Flood plain	25	750

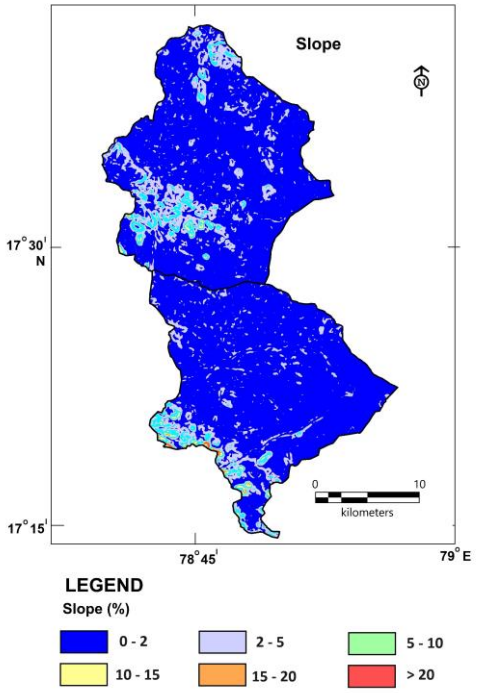

Figure 8. Slope map of the Bommala Ramaram and Bhudaan Pochampalli watersheds in Yadadri Bhuvanagiri district, Telangana state

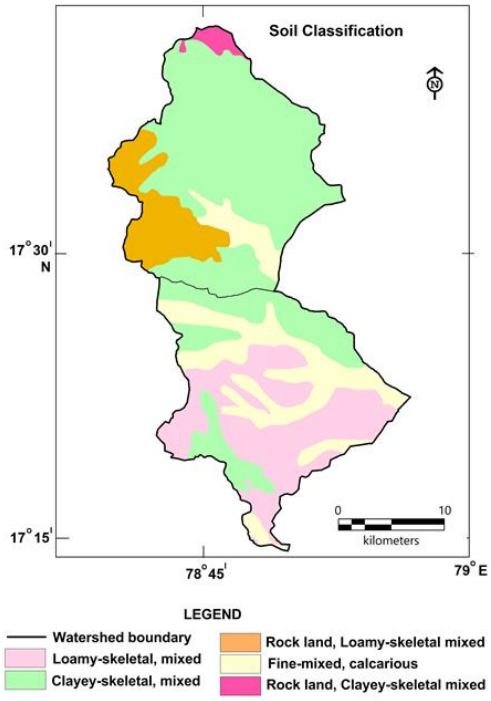

Figure 9. Soil map of the Bommala Ramaram and Bhudaan Pochampalli watersheds in Yadadri Bhuvanagiri district, Telangana state

(iv) ***Drainage density***

Drainage density is defined as the stream length per unit area in a watershed (Horton, 1945). The measurement of drainage density provides useful numerical measure of landscape dissection and runoff potential. On a highly permeable landscape, with small potential for runoff, the

drainage densities are less than 1 km per sq.km. However, in impermeable areas, the drainage densities are very high due to high runoff (Figure 10).

(v) *Lineament density*

Lineament density can be used for the quantitative evaluation of relationships between lineaments and the occurrence of groundwater. A lineament map exhibits a fault-aligned valley, a series of fault or fold-aligned hills, a straight coastline or a combination of these features. Shear zones and igneous intrusions such as dykes can also give rise to lineaments. In high lineament density areas, more chances of hydraulic interconnectivity between different aquifers may exist (Figure 11).

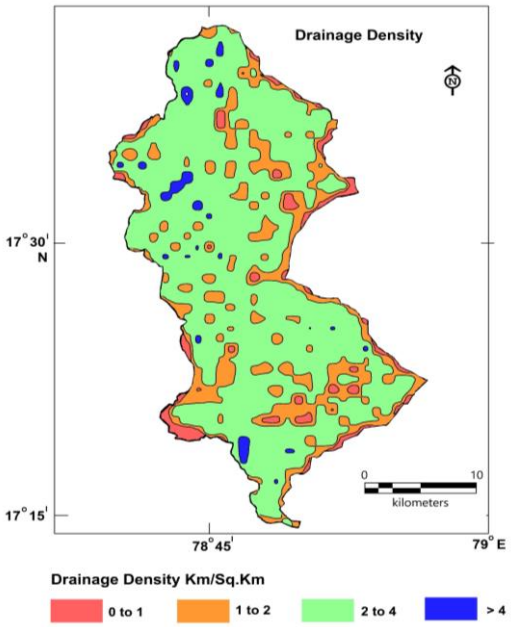

Figure 10. Drainage density map of the Bommala Ramaram and Bhudaan Pochampalli watersheds in Yadadri Bhuvanagiri district, Telangana state

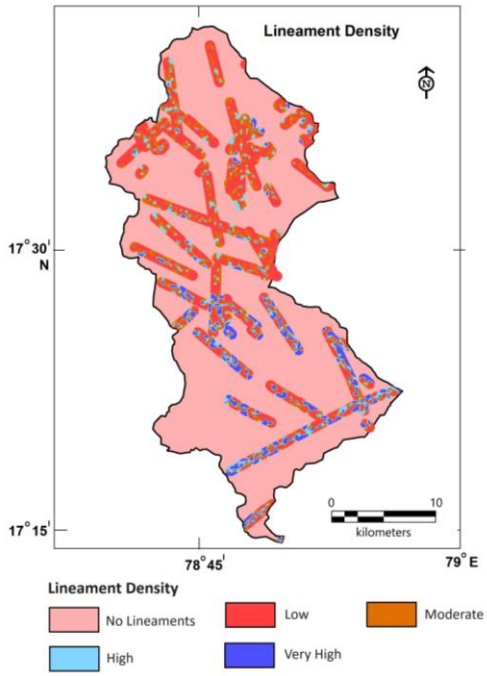

Figure 11. Lineament density map of the Bommala Ramaram and Bhudaan Pochampalli watersheds in Yadadri Bhuvanagiri district, Telangana state

(vi) ***Land use/land cover***

The land use and extent of the vegetation also controls the infiltration capacity of soils. Barren valley slopes are poor retainers of water as compared to grass lands and forested tracts. These areas not only hold water on the surface longer, but also facilitate seepage during the rainy seasons through the root systems. Similarly, ploughed fields facilitate more infiltration as compared to barren fields (Figure 12).

(vii) ***Geology***

The granites in the study area have negligible to poor primary porosity, Secondary structures like joints, fractures, shears and faults give rise to secondary porosity. Weathering and denudation aided by secondary openings and structural weak planes, add to the porosity and permeability of rock mass.

(viii) ***Depth to water level***

Areas having deeper water levels and declining water level trends are given higher priority for identification of area feasible for artificial recharge. Areas having shallow water levels/rising water level trends are not considered for inclusion in artificial recharge plan. The deep-water level is given the highest weightage because it provides ample space for recharge. The maps indicating the depth to water level is shown in Figures 4 and 5.

Artificial recharge potential zones

Figure 13 shows the final prepared map based on the present study, exhibits three different categories of potential zones for artificial recharge. The artificial recharge sites are classified as high favourable zone, moderate favourable zone and least favourable zone. The high favourable zone for artificial recharge occupies 29% of the studied area, mostly in central part of Bommala Ramaram watershed, while moderate favourable zones occupy 63% of the area and low favourable zone 8% of the area occupying hilly areas in both the watersheds.

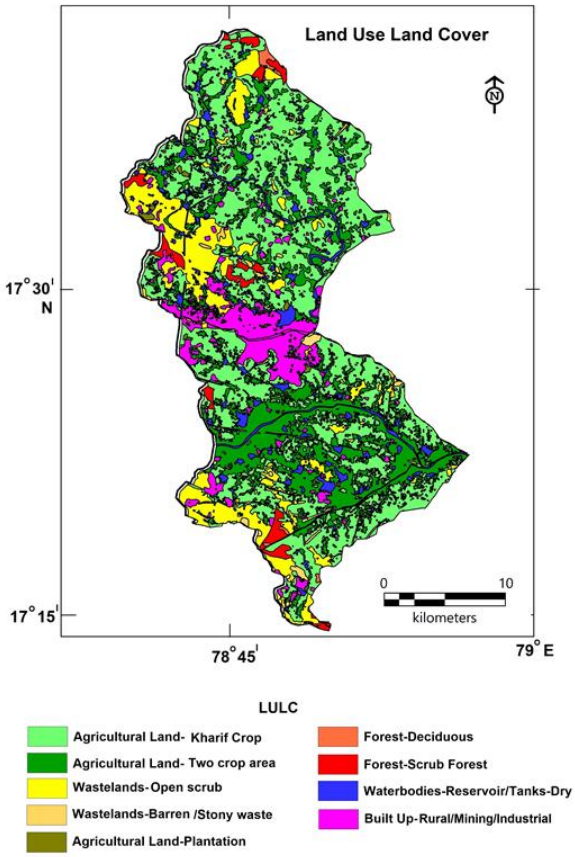

Figure 12. Land use and land cover map of Bommala Ramaram and Bhudaan Pochampalli watersheds in Yadadri Bhuvanagiri district, Telangana state.

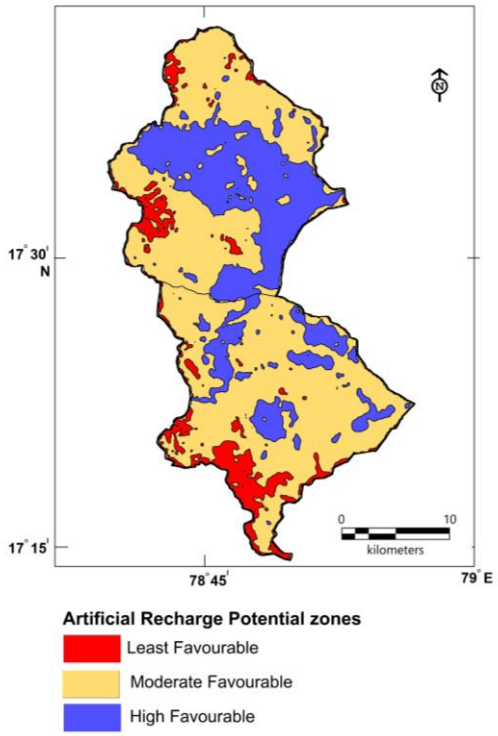

Figure 13. Artificial recharge potential zones in the Bommala Ramaram and Bhudaan Pochampalli watersheds in Yadadri Bhuvanagiri district, Telangana state

Acknowledgements

Authors thanks the Regional Director, Central Ground Water Board, Southern Region, Hyderabad for providing the data and support to complete this work.

Author Credit Statement

Study conception and design: G. Praveen Kumar. Data collection: G. Praveen kumar. Analysis, interpretation of results and draft manuscript preparation: G. Praveen kumar and Sreenu Kunsoth.

The authors reviewed the results and approved the final version of the manuscript.

Data Availability

Data supporting this study are included within the article.

Compliance with Ethical Standards

The authors declare no conflict of interest and adhere to copywrite norms

References

Choudhury, P.R., 1999. integrated remote sensing and GIS techniques for groundwater studies in part of Betwa basin, Ph.D. Thesis (unpublished), Department of Earth Sciences, University of Roorkee, India.

Elango K. and Mohan S.,1997. Technical report on effectiveness of percolation ponds. Indian Institute of Technology, Chennai, pp. 5-10.

Gale, I., 2005. Strategies for Managed Aquifer Recharge (MAR) in Semi-Arid Areas, UNESCO, IHP, HP/2005/GW/MAR, 30 p.

Ghayoumian, J., Mohseni Saravi, M., Feiznia, S., Nouri, B. and Malekian, A., 2007., Application of GIS techniques to determine areas most suitable for artificial groundwater recharge in a coastal aquifer in southern Iran. J. Asian Earth Sci., 30(20), 364-374

Horton, R., 1945. Erosional development of streams and their drainage basins hydrophysical approach to quantitative morphology. Bull. Geol. Soc. Am., 56, 275-370.

Ja Sankar, G., Jagannadha Rao, M., Prakasa Rao, B.S. and Jugran, D.K., 2001. Hydrogeomorphology and Remote Sensing applications for ground water exploration in Agnigundala Mineralised belt, Andhra Pradesh, India. J. Indian Soc. Remote Sensing, 29(3),165-174.

Janardhan Rao, Y.J., 1965. The origin of Hyderabad granites. A new interpretation. J. Ind. Geo. Sci. Assn., 5, 111-118.

Janardhan Rao, Y.J., and Sitaramaiah, S., 1968. The Pink alaskites of Ghatkesar area, Hyderabad district, A.P. J. Osmania University (Science) Golden Jubilee Vol., pp. 75-98.

Saraf, A. K. and Choudhury, P.R., 1998. Integrated Remote Sensing and GIS for Groundwater Exploration and Identification of artificial recharge sites. Int. J. Remote Sensing, 19(10), 1825-1841.

Received on: 26-12-2023 ; Revised on: 15-02-2024; Accepted on: 16-02-2024

J. Ind. Geophys. Union, 28(2) (2024), 119-130

Effect of land use and land cover changes on surface temperature: a case study from Chalisgaon (Jalgaon district, Maharashtra), India

Nilesh S. Patil[1], Bhavesh D. Patil[1]*, V. J. Patil[2], S. N. Patil[1], A. K. Kadam[1], Mayuri A. Patil[1]
[1]School of Environmental and Earth Sciences, Kavayitri Bahinabai Chaudhari North Maharashtra University, Jalgaon-425001, India
[2]Annasaheb G. D. Bendale Mahila Mahavidyalaya, Jalgaon, Maharashtra-425001, India
***Corresponding author:** bdpatil.r@nmu.ac.in

ABSTRACT

This study examines the relationship between Land Surface Temperature (LST) and Land Use and Land Cover (LULC) through a combination of ground-based, satellite-based, and re-analytical products. It focuses on the most recent changes in land surface temperature between 1991 and 2021 in the Chalisgaon Taluka of Maharashtra State, India. The results demonstrate that LULC changes have a significant impact on the climate through a range of mechanisms. There appears to be a connection between the changes in LULC spatial pattern with change in LST and Normalised Difference Vegetation Index (NDVI). The error matrix is calculated for the assessment of the accuracy of classified land use land cover images. This analysis confirms that the most substantial alterations are related to changes in plant cover, as reflected by the alterations in LULC classes as well as in NDVI. The Built-up area covered 0.91% in 1991, but grew to 6.48% in 2021 compared to 1991. Between 1991 and 2021, the study region's vegetation and agricultural land area declined by 2.64%. It was discovered that there has been a quick transition from vegetation to built-up area. The mean LST ranges were amplified dramatically from 35.05° C to 46.22° C from 1991 to 2021, largely due to the growing build-up zone and decrease vegetation The study found that the growth of urban landscapes and associated rise in human activities, as well as shifting of agricultural patterns, LULC related changes to surface temperature, and regional climate feedback across this region, warrants further research. The finding of the present study will be useful for city planner and developers as baseline information for achieving the sustainable development of the area.

Keywords: Remote Sensing, Land Use and Land Cover (LULC), Land Surface Temperature (LST), Normalised Difference Vegetation Index (NDVI), Chalisgaon (India)

INTRODUCTION

One of the most crucial aspects of the interaction between the land surface and the environment is the land surface temperature (LST). A variety of factors, including the amount of vegetation, hydrological components, glacier melting, water stress, topography, soil, groundwater, and anthropogenic structures, affect the earth's land surface and direct subsurface, therefore can be influenced by the distribution of LST. Land Use Land Cover Pattern (LULC) does have an impact on LST (Cristobal et. al., 2008; Li et. al., 2013; Ahmed et. al., 2020; Shimod et. al., 2023; Pande et. al., 2023). It depends on the earth's surface's local and global water and energy balance. It describes the evolution of surface energy over time. This is a critical indicator for evaluating a developed region, vegetation, and global warming. Currently, the LST is a major environmental problem (Lambin et. al., 2003; Rozenstein et. al., 2014; Tyagi et. al., 2023; Molnárová et. al., 2023). Because it is a fundamental factor in the physics of land surface processes, land surface temperature (LST) is an essential climatic indicator, connected to climate change and an indication of the energy balance at the surface. Crop health has been harmed over time by a variety of environmental and climate changes, including unpredictable rainfall, extreme heat stress, changing land surface temperature (LST), and population shifts from rural to urban regions (Kimuku and Ngigi, 2017; Nilesh et al., 2022; Rajesh and Pande, 2023; Thanabalan et al., 2023). Due to the ozone hole, growing greenhouse gas concentrations, and other factors, temperatures are rising everywhere in the world. In order to mitigate the effects of global climate change, scientists must concentrate their efforts on studying the LST. Therefore, it is imperative to conduct further study in this field.

Thermal remote sensing has been used in recent experiments to calculate the LST. The changes in land use and land cover (LULC) have a substantial impact on ecological services. They also have an impact on human variables including environmental and governmental planning (Southworth, 2004; Sahana et. al., 2016; Athick et. al., 2019; Gaur and Singh, 2023). Land use change and its impact on land surface temperature (LST) are identified using remote sensing and geographic information system (GIS) approaches. Land surface temperature map was created for the Yardang area of the Lut Desert (Iran) using remote sensing and Landsat thermal data (Alavipanah et. al., 2007; Buyadi et. al., 2013; Brema et. al., 2023; Gadekar et. al., 2023; Shahfahad et. al., 2023; Shang et. al., 2023). The exact methodologies they used to estimate the dynamism of land use changes on average surface temperature for a specific case study in Kenya were discussed in detail. Several studies have also shown that environmental factors influence land use and land cover changes (Cheema and Bastiaanssen, 2010; Ragin, 2014; Kayet and Pathak, 2015; Das and Sarkar, 2019; Tan et al., 2020; Chu et. al., 2022).

Similarly, the normalized difference vegetation index (NDVI) has a great ability to express itself across yearly and seasonal fluctuations in natural vegetation cover activity and vegetation's response to climatic changes (Zaidi et al., 2017; Hussain, 2018; Keerthi and Chundeli, 2023). The NDVI values are connected to the biological activities of the plant, and fluctuations in the NDVI indicate the many biological processes happening in plants (Aredehey et al., 2018; Tetali et al., 2022). The NDVI value, which measures the condition of vegetative cover, makes it simple to define daily fluctuations in LST (Xu et al., 2016). Additionally, the NDVI aids in the study of diverse vegetation phenology cycles on a global and regional scale (Olmanson et al., 2016; Ullah et al., 2019, 2023; Naga Rajesh et al., 2023). NDVI can be used to observe the vegetation's response to climatic change, seasonal plant processes, and the quality of the vegetation cover (Forkel et al., 2013; Mohammed et al., 2019; Ray et al., 2023; Adeyeri et al., 2023). The efficiency of plant covers at the landscape scale is studied using NDVI, which is a useful tool. Evapotranspiration and precipitation are connected to plant cover productivity (Gilani et al., 2015; Khan et al., 2019). Geographic information systems (GIS) and remote sensing have risen in importance for evaluating and assessing changes in land use, land cover, and land surface temperature. Remote sensing and Geographical Information Systems also have the capacity to map and identify changes in LULC and land surface temperature (Aboelnour and Engel, 2018; Malik et al., 2020). Urban biodiversity, ecosystems, and public health were all severely harmed by the rise in LST (Kafy, et al., 2021). Higher authorities can limit unplanned urban expansion and reduce future rises in urban surface temperature with the use of this study's preventative measures. One of the most effective tools for the management and mitigation of essential natural resources was soon identified as being LULC and LST fluctuations and forecast maps. The basic objective of study is to understand the impact on LULC on LST in Chalisgaon region from 1991 to 2021. Therefore, the sustainable development of the semi urban area of Chalisgaon Taluka in Jalgaon District would thus benefit greatly from this study.

DATA AND METHODOLOGY

Study Area

The study area considered for studying the relationship between LLUC, NDVI and LST, is Chalisgaon taluka situated in Maharashtra's Jalgaon district. This region lies 344 metres above mean sea level and is located between 20° 16' 12" N- 20° 43' 48" N and 74° 45' 36" E- 75° 10' 12" E (Toposheet No. 46 P/3). Since the Chalisgaon taluka is particularly developed in agriculture, numerous agro-based enterprises like the textile mills, Belganga sugar plant and some other factories have come up in the studied region. The old Patanadevi temple and forest are prominent tourist attractions in Chalisgaon. The administrative headquarters of the Chalisgaon taluka is located in Chalisgaon city. The Tittur river runs through the Chalisgaon taluka's heart. Taluka has a total area of 1284.18 square kilometres and a population of 404249, of which 306698 people live in rural areas and 97551 in urban ones. With the highest recorded temperature of around 48° C (118° F) and the lowest recorded temperature of roughly 12° C (53° F), the region is characterised by some of the most severe weather conditions. Rainfall on an average is around 109.3 mm (4.3 inches) every year. Figure 1 depicts map of the study area.

Satellite data

The research region was covered by four sets of Landsat images with a spatial resolution of 30 m each, collected in 1991, 2001, 2011, and 2021, and obtained from the USGS website (https://earthexplorer.usgs.gov/) (Table 1). Landsat Thematic Mapper (TM) and Enhanced Thematic Mapper (ETM+) images (with path/row 147/46) acquired on Landsat-5 TM data of 21 March 1991 and 12 February 2001, Landsat-7 ETM+ data of 20 March 2011, and Landsat-8 OLI data of 24 April 2021, were used for the identification of land use, land cover, Land surface temperature, and NDVI Changes. The LULC pattern is classified into six classes: agricultural land, built-up area, barren land, forest land, non-perennial river, and water bodies' area.

Image processing and classification

The initial move in Landsat analysis of imagery was pre-processing, which corrects imperfections in satellite pictures and prepares them for categorization. Landsat sensors, solar radiation, the atmosphere, and topographic characteristics, all have a role in satellite picture distortion. Pre-processing is required before further analysis of Landsat data (Mancino et al., 2014; Young et al., 2017). Arc GIS 10.4 software was used for band composition, gap filling, radiometric correction, atmospheric adjustments, and extraction of the research region. Following pre-processing, the supervised classification algorithm was used to temporal satellite datasets from 1991, 2001, 2011, and 2021. This depicts how the greatest likelihood approach was used to identify LULC changes identified in the research region. Using Arc GIS 10.4 software, 200 training sites were selected for each LULC type by creating polygons among multiple demonstration locations (Nayak and Fulekar, 2017).

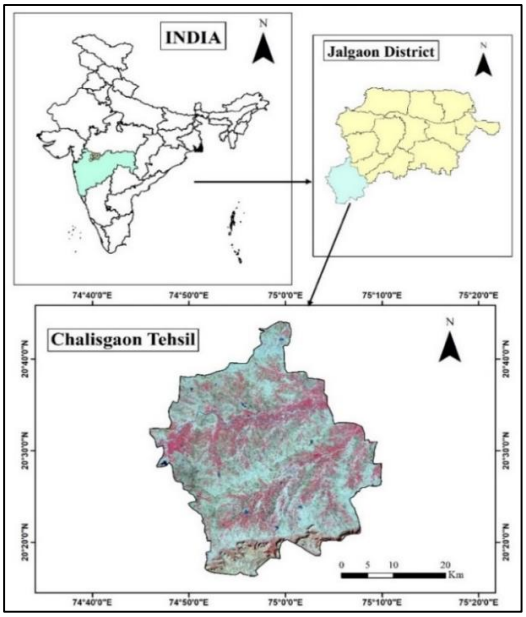

Figure 1. Location map of the study area

Table 1. Specification of Landsat data

Landsat image	Sensor	Date of acquisition	Path/Row	No. of bands	Resolution (m)	Source
Landsat 5	TM	21-03-1991	147/46	7	30	USGS
Landsat 5	TM	12-02-2001	147/46	8	30	USGS
Landsat 7	ETM+	20-03-2011	147/46	8	30	USGS
Landsat 8	OLI_TIRS	21-04-2021	147/46	11	30	USGS

Accuracy assessment

In order to compare categorized photos with ground truth data, this method is a crucial component of LULC classification. The error matrix is constructed to determine if categorised land use and land cover photographs are accurate. The matrix validated that the pixel had correctly recognized a particular feature type when associated with an identical location in the field, it was reported. For classed photos, an accurate result is produced by computing the Kappa coefficient, user accuracy (UA), producer accuracy (PA), and total accuracy. Through the use of the Google Earth engine and ground validation of GPS survey, we chose 300 sample points (reference data) at random from among the study's numerous locations.

Overall accuracy (OA) = Total number of correct sample points / total number of samples points (1)

$$\text{Kappa coefficient (K)} = \frac{N * \sum a - \sum ef}{N^2 - \sum ef} \quad (2)$$

where,

N = Quantity of ground points with the error matrix

a = Total numbers of diagonal segments

ef = summation of row and column

Estimation of Normalized Difference Vegetation Index (NDVI)

The NDVI is frequently applied in LST studies because it is less sensitive to atmospheric conditions changes than other indices. The NDVI is a numerical measure of healthy green vegetation. It derives from the electromagnetic spectrum's visible (red) and near-infrared bands. The range of NDVI values is between -1 to 1. The NDVI was used to depict the link between vegetation and LST in this investigation.

$$NDVI = \frac{NIR - Red}{NIR + Red} \quad (3)$$

In this study, the NIR and red bands from Landsat 5-7 {(Band 4 - Band 3) / (Band 4 – Band 3)} and Landsat 8 {(Band 5 - Band 4) / (Band 5 + Band 4)} were used. NDVI maps were created using the Arc GIS 10.4 software.

Estimation of Land Surface Temperature (LST)

LST is a common term concerning the combined temperature of complete objects existing on the terrestrial

surface. Several researchers applied specific measurements on Landsat data to calculate the LST. The LST values were computed from the Landsat images thermal band (band 6 of Landsat 5 TM and 7 ETM+, bands 10 and 11 of Landsat 8 OLI). The following steps were followed to generate LST from thermal bands.

Calculation of the proportion of vegetation Index (PV) was performed using following equation:

$$PV = \frac{NDVI - NDVI_{min}}{NDVI_{max} - NDVI_{min}} \quad (4)$$

Calculation of land surface emissivity

The following equation can be used to measure the land surface emissivity using the NDVI threshold (Zaharaddeen et al., 2016; Guha et al., 2020):

$$E = 0.004 * PV + 0.986 \quad (5)$$

The NDVI value varies between -1 and 1. The equivalent LSE value was applied when the NDVI value passed in the range -1 to 1 (Anandababu et al., 2018).

Thermal band's digital number (DN) to Radiance

The final task was converting the thermal band's digital number (DN) to the top of the atmosphere's (TOA) radiance ($L\lambda$). Satellite sensors measure the reflectance from the earth's surface using digital numbers (DN) believed to represent each pixel of the image. Due to this, the step is essential for subsequent activities. The following equation 6 and 7 were used to calculate spectral radiance from DN for Landsat 5/7 and Landsat 8.

Landsat 5/7

$$L\lambda = \frac{L_{max} - L_{min}}{Qcal_{max} - Qcal_{min}} * (Qcal - Qcal_{min}) + L_{min} \quad (6)$$

Landsat 8

$$L\lambda = ML*Qcal + AL \quad (7)$$

where,

$L\lambda$ = spectral radiance

L_{max} = maximum spectral radiance of the sensor

L_{min} = minimum spectral radiance of the sensor

Q_{max} = maximum DN value of pixels

Q_{min} = minimum DN value of pixels

Qcal = DN value of the pixel

ML = the band-specific multiplicative rescaling factor

AL = the band-specific additive rescaling factor

Computation of Land Surface Temperature (Kelvin)

The next step was alteration of the spectral radiance to the satellite brightness temperature (BT) using the subsequent calculation.

$$BT = \left[\frac{K2}{\left(\frac{K1}{L\lambda}\right)+1} \right] \quad (8)$$

where,

BT = At-satellite brightness temperature.

$L\lambda$ = TOA spectral radiance (Eq. 6)

Landsat 5 (TM) has K1 and K2 values of 607.76 and 1260.56, Landsat 7 (ETM+) has 666.09 and 1282.71, and Landsat 8 (OLI) has 772.88 and 1321.07, respectively. In the final step, the following equation was used to convert the temperature in kelvin to the temperature in Celsius.

$$T (^0C) = T (K) - 273.15 \quad (9)$$

RESULT AND DISCUSSION

Land Use Land Cover (LULC) Changes

The investigation of LULC variations using administered classification method from 1991 to 2021 presented that Chalisgaon Taluka situated in Maharashtra's Jalgaon district, was covered with different land features such as built-up area, barren land, river-non perennial, forest land,water bodies, and agriculture land. Total six parameters were examined to recognize the pattern of land use and land cover change in last four decades as shown in Table 2. In year 1991, 73.86% agriculture land, 4.26% barren land, 18.55% forest land, 1.58% river-non perennial, 0.84% water bodies and 0.91% built-up land was observed. In the year 2001, 72.81% agriculture land, 6.93% barren land, 17.15% forest land, 1.15% river-non perennial, 0.18% water bodies and 1.78% built-up land was witnessed. In comparison, in year 2011, 71.86% agriculture land, 4.62% barren land, 17.47% forest land, 1.15% river-non perennial, 0.96% water bodies and 3.94% built-up land was observed. Similarly, in year 2021, 71.22% was agriculture land, 5.51% barren land, 15.13% forest land, 1.20% river-non-perennial, 0.70% water bodies and 6.48% built-up land was observed (Figure 2). Nevertheless, the agriculture land as well as built-up land has witnessed the major and noticeable changes during this period compared to other parameters. Remote sensing technology advancements offer the foundation and data for LUCC's dynamic monitoring and quantitative analysis. However, there is currently no common standard for land use classification, which complicates the gathering and interpretation of land cover data.

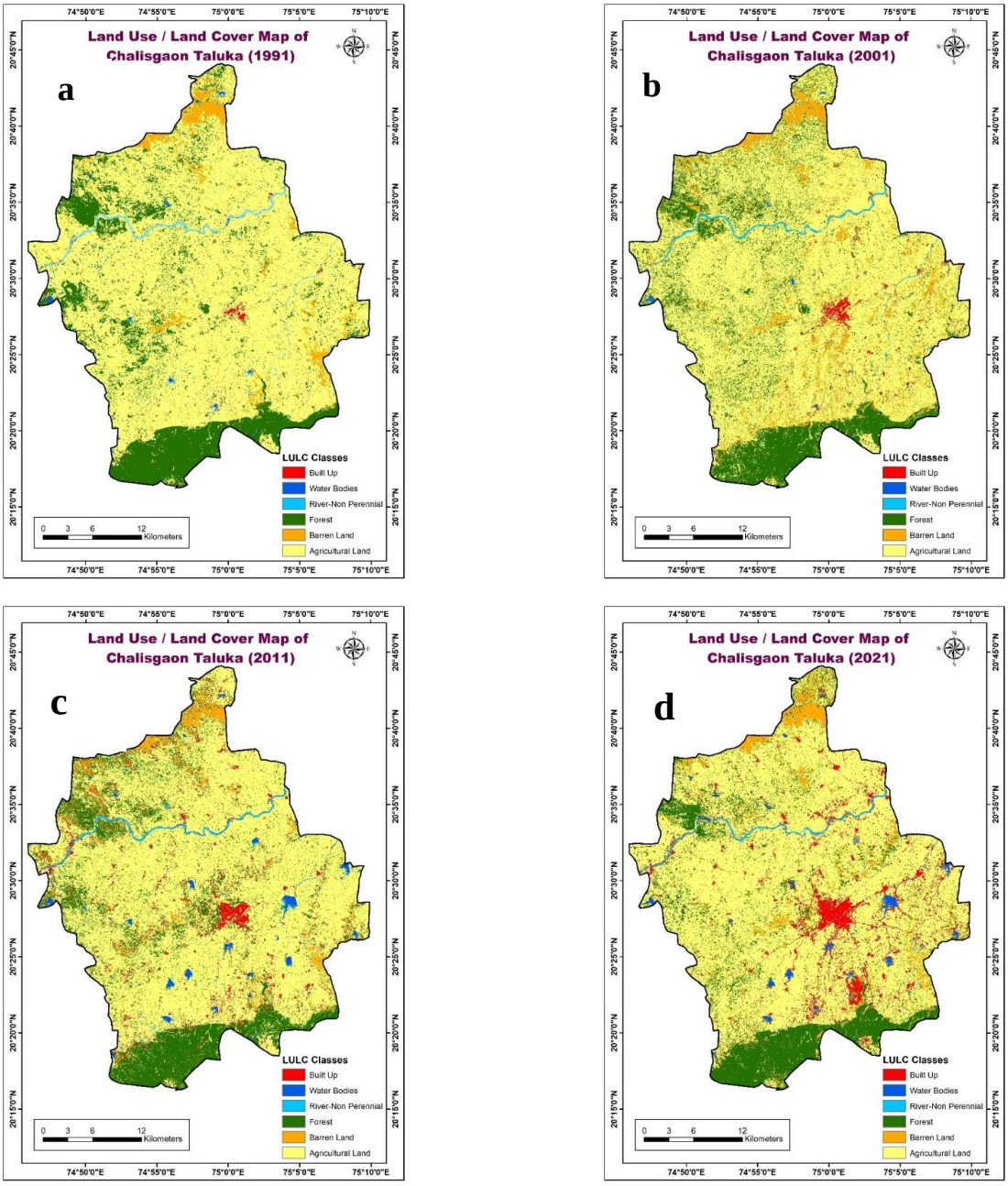

Figure 2. Land use/land cover map of Chalisgaon Taluka. **(a)** Year 1991, **(b)** 2001, **(c)** 2011 and **(d)** 2021

Table 2. Zone distribution of land use/land cover sorting from 1991 to 2021 in the Chalisgaon Taluka

LULC Classes	1991		2001		2011		2021	
	Sq.km	%	Sq.km	%	Sq.km	%	Sq.km	%
Built up land	11.00	0.91	21.51	1.78	47.60	3.94	78.23	6.48
Water bodies	10.11	0.84	2.17	0.18	11.63	0.96	8.41	0.70
River-Non perennial	19.11	1.58	13.89	1.15	13.88	1.15	14.47	1.20
Forest land	223.98	18.55	207.08	17.15	210.91	17.47	182.70	15.13
Barren land	51.46	4.26	83.70	6.93	55.78	4.62	66.59	5.51
Agriculture land	891.93	73.86	879.27	72.81	867.78	71.86	860.10	71.22
Total	1207.59	100.00	1207.59	100.00	1207.59	100.00	1207.59	100.00

Table 3. Result of the accuracy assessment of land use/land cover classification

LULC Classes	1991		2001		2011		2021	
	PA	UA	PA	UA	PA	UA	PA	UA
Built up	100%	80%	88.88%	80%	100%	80%	75%	90%
Water bodies	100%	81%	100%	100%	90.91%	100%	100%	90%
River non perennial	100%	80%	100%	80%	100%	81%	88.89%	80%
Forest	75%	83.33%	88.23%	83.33%	93.75%	83.33%	81.25%	81.25%
Barren land	81.81%	90%	72.73	80%	66.66%	80%	80%	80%
Agricultural land	91.02%	94.66%	88.89	92.75%	91.67%	92.96%	92.86%	92.86%
Overall accuracy	81.95%		88.98%		89.15%		88.89%	
Kappa coefficient	0.83		0.84		0.83		0.82	

Accuracy assessment

For several LULC classes for the years 1991, 2001, 2011, and 2021, the Table 3 provides information on user and fabricator accurateness as well as kappa (K) values. Average producer and user accuracy for 1991 was 91.3%, for 2001 it was 89.8%, for 2011 it was 90.5%, for 2021 86.3 and 85.6%. During the study years 1991, 2001, 2011 and 2021, respectively, the overall accuracy categorization for the analysed year was likewise satisfactory at 81.95%, 88.98%, 89.15% and 88.89%. The aggregated pictures' kappa coefficient values are 0.83, 0.84, 0.83, and 0.82, respectively. The scores between 0.4 and 0.55 suggest reasonable agreement, values between 0.55 and 0.7 indicate good agreement, values between 0.7 and 0.85 indicate very good agreement, and values over 0.85 show excellent agreement between the pictures. Values less than 0.4 denote poor or extremely poor agreement.

Land surface temperature (LST) changes

The remote sensing technology may be applied to measure and map the LST of any research region. Figure 3 depicts the aerial distribution and spatial pattern of LST in the Chalisgaon taluka for four years, namely 1991, 2001, 2011, and 2020. The LST spatial patterns chronological and concentration shift LST quickly reveal the changes in LULC classes. Mostly, LST estimated the range of 2.93° to 41.95° C during 1991, 19.28 to 4° 5.67° C during 2001, 4.43° to 48.84° C during 2011 and 28.80° to 53.6° 0 C during 2021. This rise seems simply geometric; nevertheless, more precise temperature growth was computed using the geographical average, and it shows that LST lifted by almost 13° C between 1991 and 2021. The land surface temperature was amplified due to growing the residential and constructional area in the study area from 1991 to 2021. The middle and southern part of the study area shows a minor temperature due to higher vegetation, water bodies and cultivated land. Contrarily, the central (eg. Chalisgaon city arena) and upper region shows an increase in LST as a result of growing urbanisation and decreasing a vegetative cover.

Normalized difference vegetation index (NDVI) changes

Examination of the normalized difference that showcases the landsat vegetation index, is based on the spectral properties of the vegetation, which absorb visible light on the plant, energy used in photosynthesis, and reflect near infrared (NIR) radiation. The Multi-Spectral Distant Sensing data approach is used by NDVI to analyse the distant sensed data and determine the vegetation index, land cover categorization, vegetation, water bodies, open regions, scrub areas, hilly areas, agricultural areas, heavy forests, and thin forests. In the studied region, the NDVI value ranges in 1991 were -0.77 to + 0.59, but in 2001, the values altered (minimum -0.54 and highest +0.65). The assessment of NDVI studies for last four decades indicate that LST has played the major role. The vegetation cover had been identified using Arc-GIS 10.8 software. The maximum and minimum NDVI value was noticed for year 2001 and 2021 respectively. In 2011, NDVI values changed (minimum −0.25 and maximum +0.60). On the other hand, year 2021 denoted NDVI values ranged from minimum −0.10 and maximum +0.57, as shown in Figure 4. This analysis indicates that vegetation and forest may be also noted as higher productive due to higher NDVI values. In the same way, lower values of NDVI denotes barren land, water bodies and residential areas. The urban expansion notably in the central part of area understudy indicated lower value NDVI; on the other hand, southern part shows higher NDVI values. Hence, the NDVI plot disclosed a major decline in the high productive part in the area understudy. By calculating their Normalized Difference Vegetation Index for Land Cover categorization, Land Resources may be perfectly defined. The simulation findings demonstrate that the NDVI

is quite effective at identifying surface characteristics in the accessible region, which is very helpful for policymakers in making decisions. Analysis of the vegetation can be useful in forecasting unpleasant natural catastrophes, urban expansion, cropping pattern, natural resources management so that aid can be provided, damage can be assessed, and new protective techniques can be developed.

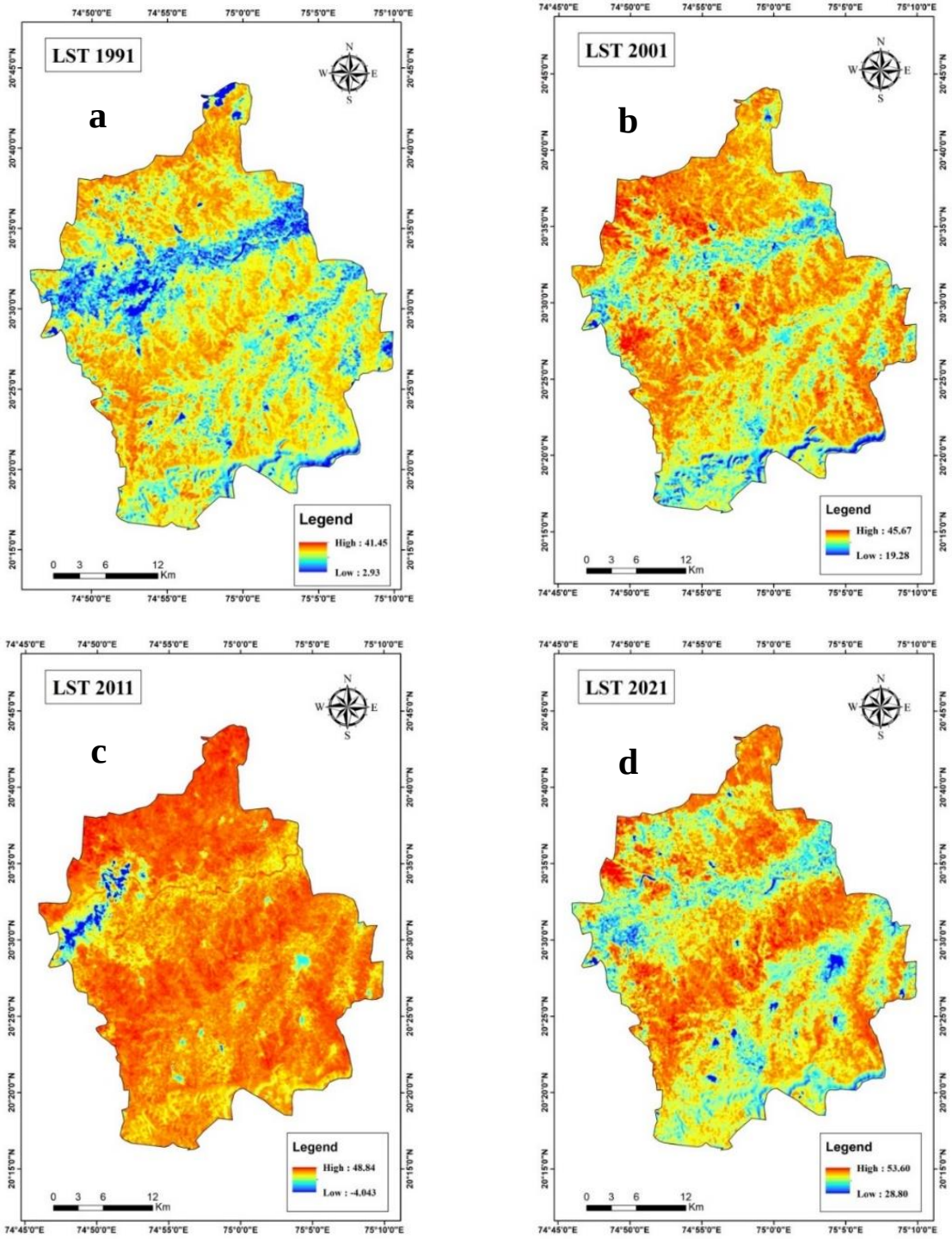

Figure 3. LST map of Chalisgaon Taluka. **(a)** Year 1991, **(b)** 2001, **(c)** 2011, **(d)** 2021

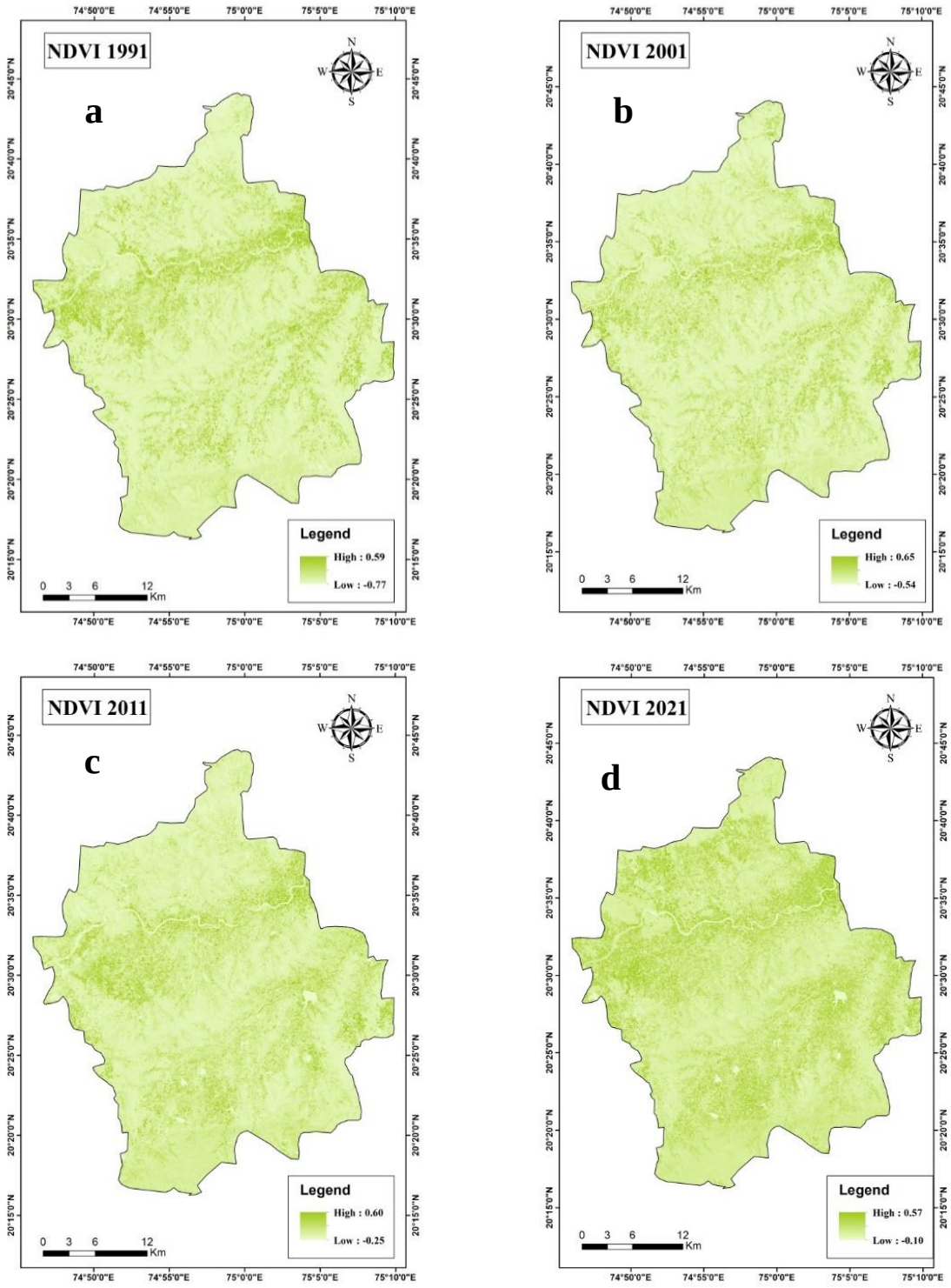

Figure 4. NDVI map of Chalisgaon Taluka. **(a)** Year 1991, **(b)** 2001, **(c)** 2011 and **(d)** 2021

Correlation between NDVI and LST

The maximum, minimum and average values of LST and NDVI is presented in the tabular form in Table 4. The link between NDVI and LST is seen in Figure 5. The regression line dramatically clarified the data, demonstrating a substantial inverse correlation between NDVI and LST. LST and NDVI are negatively connected to one another, with correlation coefficient (R) of 0.3417, 0.2566, 0.0687, and 0.3241 for the years 1991, 2001, 2011, and 2021,

respectively, according to the linear regression analysis (R) for 4 years of the analysis (Figure 5). These findings demonstrate that the impacts of LST might cause a decline in vegetation-covered regions. The negative correlation between NDVI and LST demonstrates that the lower LST is related to increasing plant biomass cover. The NDVI and LST have an immediate effect on LULC fluctuations. It also means that the territories with the lowest NDVI values have less vegetal spread due to urban expansion, whereas the territories with the highest NDVI values have thick vegetal spread, and so LST increases with lower vegetal density. There is a significant relationship between LST and NDVI, meaning that direct regression may be used to predict LST, if NDVI estimations are available in the research location.

The Figure 5 displays the connection between LST and NDVI in the Chalisgaon taluka of Maharashtra state, India, in 1991, 2001, 2011, and 2021. The NDVI values are estimated to have fallen between 1991 and 2021 because of increased urbanisation and decreasing vegetation area. The very high LST values correspond to the lowest NDVI, and vice versa. It also distinguishes between places with high LST that are bare soil and areas with low temperature that are shielded by more vegetation.

Table 4. Maximum, minimum and average values of LST and NDVI

Years	LST			NDVI		
	Min	Max	Mean	Min	Max	Mean
1991	2.93	41.45	35.05	-0.77	0.59	0.06
2001	19.28	45.67	35.08	-0.54	0.65	0.06
2011	4.04	48.84	42.10	-0.25	0.60	0.06
2021	28.80	53.60	46.22	-0.10	0.57	0.06

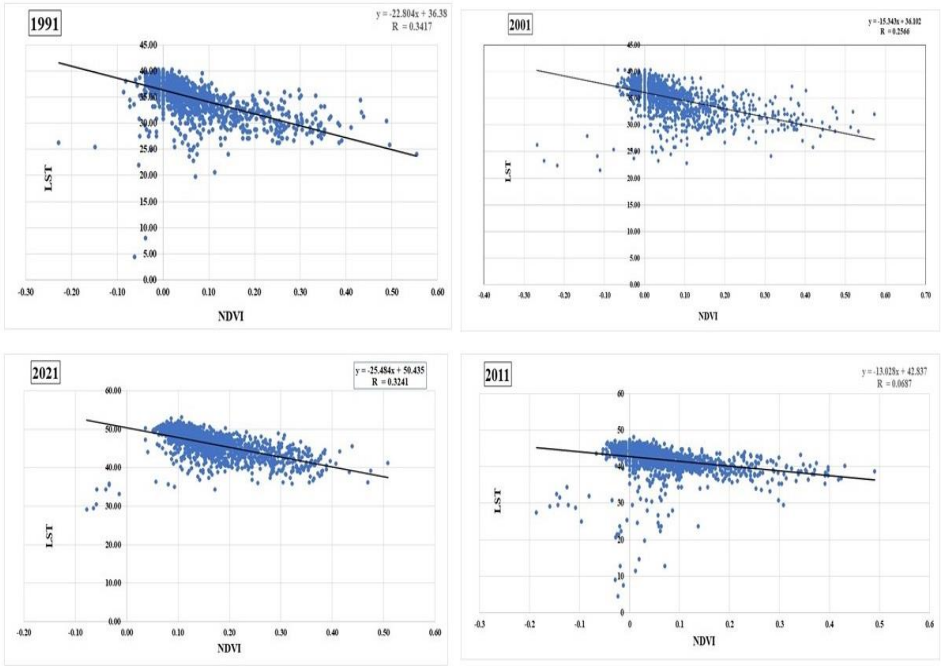

Figure 5. Corelation between NDVI and LST (Year 1991, 2001, 2011, 2021)

CONCLUSIONS

The LULC variations and their influence on LST are explored using geospatial approaches in Chalisgaon taluka of Maharashtra state. The Arc-GIS 10.8 program was used to accomplish numerous critical aspects such as correlation between NDVI and LST, Normalized difference vegetation index (NDVI) changes, Land surface temperature (LST) changes, and Land Use Land Cover (LULC) changes. Built-up area covered 0.91% in 1991, but grew to 6.48% in 2021. Between 1991 and 2021, the study region's vegetation and agricultural land area declined by 2.64%. It was discovered that there has been a quick transition from vegetation to built-up area. The mean LST ranges were amplified dramatically

from 35.05° C to 46.22° C from 1991 to 2021, largely due to the growing build-up zone and decrease in vegetation in study area. This study showed how the temperature of the study area was changed and its surface temperature rose as a result of an increase in unplanned urban development and a decrease in vegetation. Remote sensing methods are found to be effective, particularly in cutting down on the amount of time needed to analyse built-up growth, and they are helpful resources for assessing how urbanization is affecting LST. The study's findings made it clear that NDVI and LST had a very significant negative association, according to the regression analysis. The increasing population expansion and economic empowerment of social sectors have accelerated anthropological operations on the land. This research not only offered information on LULC changes, but it also recommended urban growth management strategies that, by integrating the environment friendly construction ideas through development stage planning, that may assist to minimize LST. Our findings show that there has been a reduction in agricultural and forest land. Further research is required because of the predicted growth of the urban environment, the corresponding rise in human activities, and the shifting cropping patterns, which are connected to changes in surface temperature and, consequently, to regional climate feedback across this region. The ability of the local and central governments in the study region to develop comprehensive land management strategies will be aided by the observations made in the present study.

ACKNOWLEDGMENTS

The authors (NSP) and (BDP) are thankful to CSMNRF 2021 Fellowship Scheme (CSMNRF-2021/2021-22/896) and KBC North Maharashtra University Jalgaon for Shri Gyanchand H. Raisoni Doctoral Fellowship Scheme (KBCNMU/11A/RF/237/2022) for providing fellowship.

Author Credit Statement

Nilesh S. Patil: Conceptualization, analysis, software and writing original draft; Bhavesh D. Patil: editing, data collection and software; V. J. Patil: editing, reviewing and supervision; S. N. Patil: reviewing and supervision; A. K. Kadam: analysis, software and diagrams; Mayuri A. Patil: data collection

Data Availability

All data generated or analysed during this study are included in this article.

Compliance with Ethical Standards

The authors declare that they have no conflict of interest and adhere to copy right norms.

REFERENCES

Aboelnour, M. and Engel, B.A., 2018. Application of remote sensing Techniques and geographic information system to analyse land Surface temperature in response to land use/ land cover change in greater Cairo region, Egypt. J. Geographic Inf. Syst., 10(1), 57-88.

Adeyeri, O. E., Folorunsho, A. H., Ayegbusi, I. K., Bobde, V., Adeliyi, T. E., Ndehedehe, C. E. and Akinsanola, A. A., 2023. Land surface dynamics and meteorological forcings modulate land surface temperature characteristics. Sustainable Cities and Society, 101, 105072, Doi: https://doi.org/10.1016/j.scs.2023.105072.

Ahmed, H. A., Singh, S. K., Kumar, M., Maina, M. S., Dzwairo, R. and Lal, D., 2020. Impact of urbanization and land cover change on urban climate: Case study of Nigeria. UrbanClimate, 32,100600, Doi: https://doi.org/10.1016/j.uclim.2020.100600.

Alavipanah, S. K., Komaki, C. B., karimpour, R. M., Sarajian, M., Savaghebi, F. G. R. and Moghimi, E., 2007. Land surface temperature in the Yardang region of Lut Desert (Iran) based on field measurements and Landsat thermal data. J. Agric. Sci. Technol., 9, 287-303.

Anandababu, D., Purushothaman, B. M. and Suresh, B. S., 2018. Estimation of land surface temperature using Landsat 8 data. Int. J. Advance Res., 4(2), 177-186.

Aredehey, G., Mezgebu, A. and Girma, A., 2018. Land-use land-cover classification analysis of Giba catchment using hyper temporal MODIS NDVI satellite images. Int. J. Remote Sensing, 39(3), 810-821.

Athick, A. M. A., Shankar, K. and Naqvi, H. R., 2019. Data on time series analysis of land surface temperature variation in response to vegetation indices in twelve Wereda of Ethiopia using mono window, split window algorithm and spectral radiance model. Data in Brief, 27, 104773.

Brema, J., Alsalmi, A. K., Mayilswami, C. and Thinakaran, J., 2023. Effect of Urbanism on Land Surface Temperature (LST) in a River Basin and an Urban Agglomeration. In: Pande, C.B., Moharir, K.N., Singh, S.K., Pham, Q.B., Elbeltagi, A, (eds) Climate Change Impacts on Natural Resources, Ecosystems and Agricultural Systems, Springer Int. Publishing, pp. 345-365, Doi: https://doi.org/10.1007/978-3-031-19059-9_13

Buyadi, S. N. A., Mohd, W. M. N. W. and Misni, A., 2013. Impact of land use changes on the surface temperature distribution of area surrounding the National Botanic Garden, Shah Alam. Procedia-Social and Behavioral Sci., 101, 516-525.

Cheema, M. J. M. and Bastiaanssen, W. G., 2010. Land use and land cover classification in the irrigated Indus Basin using growth phenology information from satellite data to support water management analysis. Agricultural Water Management, 97(10), 1541-1552.

Chu, X. L., Zhong, L. U., Dan, W. E. I. and Lei, G. P., 2022. Effects of land use/cover change (LUCC) on the spatiotemporal variability of precipitation and temperature in the Songnen Plain, China. J. Integrative Agriculture, 21(1), 235-248

Cristobal, J., Ninyerola, M. and Pons, X., 2008. Modeling air temperature through a combination of remote sensing and GIS data. J. Geophys. Res., 113, 1–13

Das, S. and Sarkar, R., 2019. Predicting the land use and land cover change using Markov model: A catchment level analysis of the Bhagirathi-Hugli River. Spatial Information Res., 27(4), 439-452.

Forkel, M., Carvalhais, N., Verbesselt, J., Mahecha, M. D., Neigh, C. S. and Reichstein, M., 2013. Trend change detection in NDVI time series: Effects of inter-annual variability and methodology. Remote Sensing, 5(5), 2113-2144.

Gadekar, K., Pande, C.B., Rajesh, J., Gorantiwar, S.D. and Atre, A.A., 2023. Estimation of land surface temperature and urban heat island by using google earth engine and remote sensing data. In: Pande, C.B., Moharir, K.N., Singh, S.K., Pham, Q.B., Elbeltagi, A, (eds) Climate Change Impacts on Natural Resources, Ecosystems and Agricultural Systems, Springer Int. Publishing, 367-389., Doi: https://doi.org/10.1007/978-3-031-19059-9_14

Gaur, S. and Singh, R., 2023. A comprehensive review on land use/land cover (LULC) change modeling for urban development: current status and future prospects. Sustainability, 15(2), 903, Doi: https://doi.org/10.3390/su15020903.

Gilani, H., Shrestha, H. L., Murthy, M. S. R., Phuntso, P., Pradhan, S., Bajracharya, B. and Shrestha, B., 2015. Decadal land cover change dynamics in Bhutan. J. Environ. Manag., 148, 91-100.

Guha, S., Govil, H., and Diwan, P., 2020. Monitoring LST-NDVI relationship using Premonsoon Landsat datasets. Advances in Meteorology, 2020, 1-15. Doi: https://doi.org/10.1155/2020/4539684

Hussain, S., 2018. Land use/land cover classification by using satellite NDVI tool for sustainable water and climate change in Southern Punjab. COMSATS Univ. Islamabad.

Kafy, A. A., Dey, N. N., Al Rakib, A., Rahaman, Z. A., Nasher, N. R., and Bhatt, A., 2021. Modeling the relationship between land use/land cover and land surface temperature in Dhaka, Bangladesh using CA-ANN algorithm. Environ. Challenges, 4, 100190.

Kayet, N. and Pathak, K., 2015. Remote sensing and GIS based land use/land cover change detection mapping in Saranda Forest, Jharkhand, India. Int. Res. J. Earth Sci., 3(10), 1-6.

Keerthi Naidu, B. N. and Chundeli, F. A., 2023. Assessing LULC changes and LST through NDVI and NDBI spatial indicators: a case of Bengaluru, India. Geo. J., 88, 1-16. Doi: https://doi.org/10.1007/s10708-023-10862-1

Khan, I., Javed, T., Khan, A., Lei, H., Muhammad, I., Ali, I. and Huo, X., 2019. Impact assessment of land use change on surface temperature and agricultural productivity in Peshawar-Pakistan. Environ. Sci. Pollution Res., 26(32), 33076-33085.

Kimuku, C. W. and Ngigi, M. M., 2017. Study of urban heat island trends to aid in urban planning in Nakuru County-Kenya. Doi: http://41.89.227.156:8080/xmlui/handle/123456789/590

Lambin, E.F., Geist, H.J. and Lepers, E., 2003. Dynamics of land-use and land-cover change in tropical regions. Annu. Rev. Environ. Resour., 28(1), 205–241

Li, Z.L., Tang, B.H., Wu, H., Ren, H., Yan, G., Wan, Z., Trigo, I.F. and Sobrino, J.A., 2013. Satellite-derived land surface temperature: current status and perspectives. Remote Sens. Environ., 131, 14–37

Malik, S. M., Arshad, S., Alam, K. and Bilal, O., 2020. Monitoring urban growth and land use changes using GIS and remote sensing: A case study of Taluka Burewala. J. Himalayan Earth Sci., 53(1), 140-152.

Mancino, G., Nolè, A., Ripullone, F. and Ferrara, A., 2014. Landsat TM imagery and NDVI differencing to detect vegetation change: assessing natural forest expansion in Basilicata, southern Italy. Forest-Biogeosciences and Forestry, 7(2), 75.

Mohammed, A. A. A. S., Shankar, K. and Hasan, R. N., 2019. Data on time series analysis of land surface temperature variation in response to vegetation indices in twelve Wereda of Ethiopia using mono window, split window algorithm, and spectral radiance model. Data in Brief, 27, 104773. doi: https://doi.org/10.1016/j.dib.2019.104773

Molnárová, Janečková,K., Sklenička, P., Bohnet, I.C., Fred Lowther-Harris et al., 2023. Impacts of land consolidation on land degradation: A systematic review., J. of Environmental Management, 329, 117026, Doi: https://doi.org/10.1016/j.jenvman.2022.117026

Naga Rajesh, A., Abinaya, S., Purna Durga, G., and Lakshmi Kumar, T. V., 2023. Long-term relationships of MODIS NDVI with rainfall, land surface temperature, surface soil moisture and groundwater storage over monsoon core region of India. Arid Land Res. Manag., 37(1), 51-70, Doi: https://doi.org/10.1080/15324982.2022.2106323.

Nayak, D. P. and Fulekar, M. H., 2017. Coastal geomorphological and land use and land cover study on some sites of Gulf of Kachchh, Gujarat, West Coast of India using multi-temporal remote sensing data. Int. J. Adv. Remote Sens. GIS, 6(1), 2192-2203.

Nilesh, P., Vilas, P., Sanjaykumar, P., Bhavesh, P., Arvind, S., Kavita, J. and Mahavidyalaya, A. G. B., 2022. Analysis of Urban Growth and Its Impact on Agriculture Land around the Chalisgaon City in Jalgaon District of Maharashtra, India: A Remote Sensing and GIS Based Approach. J. Geomatics, 16(2), 213-222. doi: https://doi.org/10.58825/jog.2022.16.2.51

Olmanson, L. G., Brezonik, P. L., Finlay, J. C. and Bauer, M. E., 2016. Comparison of Landsat 8 and Landsat 7 for regional measurements of CDOM and water clarity in lakes. Remote Sensing of Environment, 185, 119-128.

Pande, C. B., Moharir, K. N., Varade, A. M., Abdo, H. G., Mulla, S. and Yaseen, Z. M., 2023. Intertwined impacts of urbanization and land cover change on urban climate and agriculture in Aurangabad city (MS), India using google earth engine platform. J. Cleaner Production, 422, 138541, Doi: https://doi.org/10.1016/j.jclepro.2023.138541

Ragin, C. C., 2014. The comparative method: Moving beyond qualitative and quantitative strategies. Univ of California Press.

Rajesh, J. and Pande, C. B., 2023. Estimation of land surface temperature for rahuri taluka, Ahmednagar District (MS, India), Using remote sensing data and algorithm. In: Climate Change Impacts on Natural Resources, Ecosystems and Agricultural Systems. Cham: Springer Int. Publishing., 565-577, doi: https://doi.org/10.1007/978-3-031-19059-9_24

Ray, R., Das, A., Hasan, M. S. U., Aldrees, A., Islam, S., Khan, M. A. and Lama, G. F. C., 2023. Quantitative Analysis of Land Use and Land Cover Dynamics using Geoinformatics

Techniques: A Case Study on Kolkata Metropolitan Development Authority (KMDA) in West Bengal, India. Remote Sensing, 15(4), 959, Doi: https://doi.org/10.3390/rs15040959.

Rozenstein, O., Qin, Z., Derimian, Y. and Karnieli, A., 2014. Derivation of land surface temperature for Landsat-8 TIRS using a split window algorithm. Sensors, 14(4), 5768-5780.

Sahana, M., Ahmed, R. and Sajjad, H., 2016. Analyzing land surface temperature distribution in response to land use/land cover change using split window algorithm and spectral radiance model in Sundarban Biosphere Reserve, India. Modeling Earth Systems and Environment, 2(2), 1-11.

Shahfahad, Bindajam, A.A., Naikoo, M.W., Horo, J.P., Mallick, J., Rihan, M., et al., 2023. Response of soil moisture and vegetation conditions in seasonal variation of land surface temperature and surface urban heat island intensity in sub-tropical semi-arid cities. Theoretical and Appl. Climatology, 153, 1-29, Doi: https://doi.org/10.1007/s00704-023-04477-2.

Shang, G., Yuan, Q., Zhang, X., Sun, M., Liu, S., Hu, Y., Yan, Z., Gao, Y. and Zhang, C., 2023. Remote sensing inversion of land surface temperature for cloud coverage areas based on NDVI in the North China Plain. Int. J. of Remote Sensing, 1-16 Doi: https://doi.org/10.1080/01431161.2023.2216854.

Shimod, K. P., Prasad, T. K., Vineethkumar, V., Akhil, R. and Jayapal, G., 2023. Geospatial Technology for Analysing the Dynamics in Microclimate with Special Reference to Land Surface Temperature of Tropical Cities: A Case Study. In Urban Commons, Future Smart Cities and Sustainability, Cham: Springer Int. Publishing, 321-340, Doi: https://doi.org/10.1007/978-3-031-24767-5_15

Southworth, J., 2004. An assessment of Landsat TM band 6 thermal data for analysing land cover in tropical dry forest regions. Int. J. Remote Sensing, 25(4), 689-706.

Tan, J., Yu, D., Li, Q., Tan, X., and Zhou, W., 2020. The spatial relationship between land-use/land-cover changes and land surface temperature in the Dongting Lake area, China. Scientific Reports, 10(1), 1-9.

Tetali, S., Baird, N., and Klima, K., 2022. A multicity analysis of daytime Surface Urban Heat Islands in India and the US. Sustainable Cities and Society, 77, 103568.doi: https://doi.org/10.1016/j.scs.2021.103568

Thanabalan, P., Vidhya, R. and Kankara, R.S., 2023. Time-series analysis of MODIS (LST and NDVI) and TRMM rainfall for drought assessment over India. Appl. Geomatics, 15, 383–405. Doi: https://doi.org/10.1007/s12518-023-00505-y

Tyagi, A., Tiwari, R. K. and James, N., 2023. Mapping the landslide susceptibility considering future land-use land-cover scenario. Landslides, 20(1), 65-76, Doi: https://doi.org/10.1007/s10346-022-01968-7.

Ullah, S., Tahir, A. A., Akbar, T. A., Hassan, Q. K., Dewan, A., Khan, A. J. and Khan, M., 2019. Remote sensing-based quantification of the relationships between land use land cover changes and surface temperature over the Lower Himalayan Region. Sustainability, 11(19), 5492.

Ullah, W., Ahmad, K., Ullah, S., Tahir, A.A., Javed, M.F., Nazir, A., Abbasi, A.M., Aziz, M. and Mohamed, A., 2023. Analysis of the relationship among land surface temperature (LST), land use land cover (LULC), and normalized difference vegetation index (NDVI) with topographic elements in the lower Himalayan region. Heliyon 9, (2), 13322. Doi: https://doi.org/10.1016/j.heliyon.2023.e13322.

Xu, L., Li, B., Yuan, Y., Gao, X., Zhang, T. and Sun, Q., 2016. Detecting different types of directional land cover changes using MODIS NDVI time series dataset. Remote Sensing, 8(6), 495.

Young, N. E., Anderson, R. S., Chignell, S. M., Vorster, A. G., Lawrence, R. and Evangelista, P. H., 2017. A survival guide to Landsat preprocessing. Ecology, 98(4), 920-932.

Zaharaddeen, I., Baba, I. I., and Zachariah, A., 2016. Estimation of land surface temperature of Kaduna metropolis, Nigeria using Landsat images. Science World J., 11(3), 36-42.

Zaidi, S. M., Akbari, A., Abu Samah, A., Kong, N. S., Gisen, A. and Isabella, J., 2017. Landsat-5 Time Series Analysis for Land Use/Land Cover Change Detection Using NDVI and Semi-Supervised Classification Techniques. Polish J. of Environmental Studies, 26(6), 2833-2840. Doi: 10.15244/pjoes/ 68878

Received on: 23-10-2023 ; Revised on: 04-02-2024; Accepted on: 05-02-2024

J. Ind. Geophys. Union, 28(2) (2024), 131-142

Variation of Surface Latent Heat Flux (SLHF) observed during high-magnitude earthquakes

Pooja Sharma[1], Ananna Bardhan[1*], Raj kumari[2], D.K. Sharma[1] and Ashok Kumar Sharma[3]
[1]Department of Sciences, Manav Rachna University, Faridabad-121004, Haryana, India
[2]Department of Physics, DAV Centenary College, Faridabad-121001, Haryana, India
[3]School of Physics, Shri Mata Vaishno Devi University, Katra-182320, Jammu and Kashmir, India
*Corresponding author: ananna@mru.edu.in

ABSTRACT

Various precursory signatures are observed over the ocean-land-atmosphere due to seismic activities. Earthquakes create a lot of destruction to life and property. Therefore, understanding and monitoring various anomalies in geophysical parameters are required to understand the precursory signature for the early warning and the prediction of earthquakes. In the present work, the Surface Latent Heat Flux (SLHF) has been analysed for recent seven high-magnitude ($M \geq 6.0$) earthquakes. For this purpose, data on SLHF has been retrieved from the NCEP website. The climatological analysis for seismic precursor identification (CAPRI) methodology was adopted to study the SLHF before the earthquakes. A significant anomalies change in the SLHF was observed. Maximum increase in SLHF was found to be ∽20 days prior to the main earthquake events. The maximum and minimum anomalies in SLHF during all seven events were analysed. The variation in maximum and minimum anomaly is the least over the earthquakes events that occurred over land. This variation increases for the earthquakes that occurred over the ocean or near the vicinity of the ocean. The outgoing radiation trapped via accumulated water vapours results in increased heat over the surface of epicentres and nearby areas. This has contributed to the rise in surface latent heat flux before all the seven major earthquake events.

Keywords: Surface Latent Heat Flux (SLHF), EPZ, Lithosphere–Atmosphere–Ionosphere Model (LAIC), Seismic precursor identification, Earthquake magnitude.

INTRODUCTION

Unstable plate tectonic movements over the lithosphere are the major cause of increased seismicity. The increased seismicity results in the accumulation of stress which further causes crack. When a crack reaches a specific distortion that it can no longer tolerate, it breaks, releasing most of the energy that has developed over the years, and decades. The earthquake preparatory phase is often referred to as the final stage before the advent of an earthquake. The time scale of the preparatory phase ranges from months to years. Various phenomena associated with the preparatory phase of an earthquake, as well as the interaction of the solid ground with the atmosphere are widely discussed (Tanimoto, 2015). The metrological and ionospheric parameters vary during earthquake affected period (Bina, 1998; Chan and Wu, 2012; Chowdary et al., 2012; Beig et al., 2013; Sharma et al., 2013; González-Zamora et al., 2015; Aggarwal et al., 2016; Bardhan et al., 2017; Kumar, 2021). The process of an earthquake involves various phenomena in the earth's core and the magnetosphere. Therefore, understanding, monitoring, and prediction of earthquakes becomes complex and its monitoring remains difficult (Holliday et al., 2008; Sharma et al., 2013; Aggarwal et al., 2016; Bardhan et al., 2017). If we study the characteristics of atmospheric conditions, we might be capable of predicting when an earthquake will occur.

In recent years, several destructive earthquakes have occurred often along the earth-ocean surface (Kumar and Singh, 2014; Huang et al., 2015; Kumar, 2016; Ruiz-Pinilla et al., 2016; Chauhan et al., 2018). The lithosphere–atmosphere–ionosphere model (LAIC) couples the transportation of energy and particles from the earth's crust to the atmosphere and then to the ionosphere as studied by Pulinets and Ouzounov (2011). They analysed various anomalous changes in meteorological and atmospheric variables and integrated the results to predict the forthcoming earthquakes. Further, they observed anomalous behaviour such as thermal infrared radiation (TIR), air temperature, humidity, radon/ion activities, electromagnetic (EM) variations, and electron density (Ne) in the ionosphere. Even though the LAIC model has not been fully proven, it predicts TIR in the Earth's atmosphere that is also confirmed by satellite detection from the above. Thermal abnormalities are observed within a few days to two months before the earthquakes, which can last for up to a week thereafter (Piscini et al., 2017). The anomalies extend from a few kilometres to hundreds of kilometres. Subjected to tectonic and continental stress, the convective fluid beneath the earth's surface separates into water liquid and water vapor. The heat, vapor, and liquid accumulated in this process oyez out through various faults, cracks, and fissures. The increased rate of this preparatory stress finally results in a major fault rupture. The heat transfer in this process changes the surface temperature and, henceforth moisture content of the soil and its physical and chemical properties. Furthermore, according to Pullinets and Ouzounov (2011), the latent heat released during the water vapor condensation on the ion due to air ionization by the radon, results in an increase in air temperature. It is also observed by them that the relative humidity drops and the air temperature increases before major earthquakes.

Similarly, Dey and Singh (2003) analysed multi-sensor data and observed anomalies in atmospheric water vapor content prior to the Gujarat earthquake on January 26, 2001. Singh et al. (2001) also reported significant changes in the land/surface/subsurface parameters. Although earthquake detection remains a difficult

task, anomalies in several meteorological characteristics have been strongly associated as precursory signatures before earthquakes (Knopoff, 1996). Many pre-earthquake meteorological and ionospheric factors related to earthquakes that have happened all over the world, have been reported by several authors (Merzer and Klemperer, 1997; Ohta et al., 2001; Biagi et al., 2001; Molchanov et al., 2001; Uyeda et al., 2001). This earthquakes with low epicentre near the ground surface have caused significant changes in land and ocean characteristics (Kumar et al., 2011; Kumar and Singh, 2013, 2014) leading us to investigate the influence. A 42-year anomaly of SLHF from the epicentre and maximum surge was discovered 10–15 days before the main earthquake events (Kumar, 2021). Potirakis et al. (2021) focused on fracto-electromagnetic emissions in the MHz band, ultra-low frequency (ULF) magnetic field changes (3 Hz), and sub-ionospheric very low frequency (VLF) propagation anomalies. Sasmal et al. (2021) analysed pre-seismic abnormalities in the stratosphere, ionosphere, and magnetosphere and observed a significant enhancement in the electron density pre-seismic anomaly from ten days to one day, before the earthquakes. Conti et al. (2021) provided a summary of the observations made on the ground to discover earthquake precursors by identifying them from a broad background consisting of both natural and artificial non-seismic sources. The large and short-scale ionospheric anomalies occurring a few hours to a few days before the seismic events, may be connected to the upcoming occurrence (Oikonomou et al., 2020). Ghosh et al. (2021) had shown a spatio-temporal variability in the SLHF within a week before the each main shock.

The heat emitted during the phase transitions such as solidification, melting, or evaporation is known as surface latent heat flux (SLHF). The energy losses due to radiation processes observed in the atmosphere are compensated for via energy transport within the earth-ocean-atmosphere (Schulz et al., 1997). The SLHF is strongly influenced by the seasonal changes; for example, the speed of the wind, levels of humidity, ocean height, and proximity to the ocean. The water vapor and heat exchange with the atmosphere is much higher at the ocean surface than over the land, and hence SLHF is observed to drop as it gets away from the land-ocean interface and nearer to the land. The energy exchange rate between the land surface and the atmosphere increases the SLHF. Freund and Ouzounov (2001) reported the accumulation of stress due to increased thermal infrared emission before the earthquake, resulting in the enhancement of the above set of the exchange rate. Further, Tronin (2000) reported that the change in surface temperature (ST) is one of the probable parameters for variability in SLHF as a precursory parameter. Tronin et al. (2002) also reported anomaly ST and increased ST as a precursor prior to Kobe (Japan) and China earthquakes on January 17, 1995, and January 10, 1998 respectively. These earthquakes created lot of havoc to the mankind and the property. Earthquake prediction still remains daunting and a difficult task. Many destructive earthquakes have happened repeatedly in recent years. Thus, we are motivated to analyse precursory behaviour of SLHF during seven high magnitude recent earthquakes (M≥6.0) over the decades. A lot more comprehensive work involving analysis of various land and surface parameters is required.

DATA USED AND METHODOLOGY

The SLHF data of the seven recent earthquakes have been taken from the National Centre for Environmental Prediction/National Centre for Atmospheric Research (NCEP- NCAR) obtained across the Oceans, spanning the epicentre of the earthquakes (NCEP) (http://iridl.ldeo.columbia.edu/SOURCES/.NOAA/.NCEP-NCAR/.CDAS-1/.DAILY/.Diagnostic/.surface/.latent/.heat_flux/dataselection.html). The details of these earthquakes are given in Table 1, which have been taken from United States Geological Survey (USGS) (http://earthquake.usgs.gov/activity/world.html). The event locations, date and time, epicentre of the events, as well as the focal depths, are detailed in Table 1. We take into account earthquakes in Biak, Papua, Ternate, Padang, Assam, and Kathmandu. These datasets are built by integrating data from satellites with measured values from various sites throughout the world. A worldwide dataset of various climatological and surface variables is maintained by NCEP. The fluxes considered in functional meteorological forecasting techniques contain in-situ data. The NCEP-NCAR (National Centers for Environmental Prediction/National Center for Atmospheric Research) integrates the data from remote sensing, aircraft, pibal, rawinsonde, ship, ground instruments etc. Thus, provides assimilated global reanalysed data with an accuracy limit of 10-30 W/m^2 (Zhang et al., 2013). The daily SLHF values have a spatial resolution of 1.87×1.90 degrees with a global longitude and latitude during 1 Jan 1948 to current time respectively.

DATA SELECTION AND ANALYSIS FOR SURFACE LATENT HEAT FLUX

To understand the anomalies registered in SLHF before all the seven earthquakes, the Climatological Analysis for seismic Precursor Identification (CAPRI) method has been employed. The mathematical algorithm of CAPRI method (Piscini et al., 2017, 2019) is briefly discussed here. Dobrovolsky et al. (1979) suggested an observational association between the predicted circular area of mechanical, thermal, electromagnetic precursors and the magnitude of the future earthquake since seismic precursors generally develop on huge areas surrounding forthcoming faults as,

$$r = 10^{0.43M}$$

Where r is the "strain radius", which is the radius of the afflicted region in km and M is the magnitude of the upcoming

earthquake. Using $r = 10^{0.43M}$ the earthquake preparation zone (EPZ) is calculated. The anomalies of the surface latent heat flux have been evaluated over the EPZ. The CAPRI method is supposed to look for anomalies in climatological variable time series using statistical analysis. It is used for the examined parameter, which is the SLHF. The data is spatially averaged before being analysed above epicentral region. SLHF $(d)_y$ the mean value of SLHF data for the day d (=2 months/60 days) that year y (i.e. 38 years of dataset) is SLHF (d)y. The CAPRI methodology eliminates the long-term trends across the entire day-by-day information. Its approach is primarily proposed to minimize a probable "global warming".

To eliminate these trends, details across a 38-year period, individual time sequences with the same day are analysed separately, with a linear fit of the examined variables for every single day of the year over the whole time period (Piscini et al., 2017, 2019). The fit slope m (d) (i.e., SLHF variation on the same day d, for every year) is then used to eliminate the variable's long-term variations. Given the short time period studied (about 40 years) relative to climate change, a linear fit is a good trend (Brohan et al., 2006).

Now the first year of the time-series data, y_o, has been used as a 'reference', and the expansion in the variable is calculated by multiplying the slope of the fit by the successive numbers of years from the first, which is eliminated for subsequent years,

$$SLHF'(d)_y = SLHF(d)_y - m(d) \times (y - y_o) \quad (1)$$

This method is used for each of the days under consideration. The benefit of doing a new fit for each day is that it allows you to account for the possibility of a variable seasonal local influence over time (Piscini et al., 2017, 2019). For every year studied, the information obtained is the daily spatially average SLHF, day by day. Ignoring the fact that the year 2021 did not relate to the estimates of the consistent pattern, the detected pattern was also eliminated in that year. The variables from the time-series data are then aggregated across all years with each day d, providing the mean, $SLHF_h(d)$, for that day in the previous 37 years (i.e. 1984-2020, for the reason that the year of the studied earthquake series is now excluded),

$$SLHF_h(d) = \frac{1}{Ny} \sum_{y=\alpha}^{\beta} SLHF'(d)_y \quad (2)$$

Where N_y is the total number of years that have been aggregated and α is the initial year and β is the 37th year. In particular, the programme estimates the standard deviation σ for each day. The subsequent year's factor behaviour 'ỹ' is then compared to the historical series 'Eq. (1)'. To make this comparison possible, we set the overall average in the studied period to correspond with the average of the historical time series to make this comparison possible,

$$SLHF(d)_{\tilde{y}} = SLHF'(d)_{\tilde{y}} - [(SLHF'_{\tilde{y}})_d - (SLHF_h)_d] \quad (3)$$

This analysis helps us to distinguish between the short-time anomalies we're searching. This is attributed to the reason that heat caused by lithospheric seismic events is just predicted to last a few days. Therefore, individual anomalous days are defined as days where the value of the studied variable is above its mean by at least two standard deviations. We then look for the at least 2σ above and below surge anomaly to continue for longer than a day. There are also some spatial concerns regarding the distribution patterns of the variables examined on an anomalous day.

RESULTS AND DISCUSSION

In this study, we have examined seven recent high-magnitude ($M \geq 6.0$) earthquakes that occurred between years 2015 and 2022. In all the events, behaviour of SLHF as a precursor has been analysed. As mentioned earlier, the details of all the earthquake events are taken from the website of the National Earthquake Information Centre (NEIC), United States Geological Survey (USGS), which includes location, date & time, epicentre, magnitude, focal depth, and distance from the ocean given (Table 1).

The earthquake that occurred on September 10, 2022, had a magnitude of 6.2 and a depth of 21.0 km (epicentre 2.23° S and 138.17° E) in Biak, Indonesia. The variation in SLHF has been analysed for the purpose of identifying precursory signatures during the earthquake event. Figure 1 compares the earthquake year 2022 vs. the mean historical time series in 1985–2021 during the earthquake events that occurred. In Figure 1, the red line with a circle and the black line with a diamond, denote the earthquake year and a historical time series of 37 years, respectively. Coloured lines represent 1.0 (green), 1.5 (pink), and 2.0 (blue) standard deviations from the mean historical time series, respectively. The SLHF values were studied over a period of 59 days before an earthquake event. The 60th day is marked with (an orange line) the day of the earthquake event. It is observed that SLHF varies differently from the historical time series, and there are observable instances when the magnitude of SLHF is greater than 2 standard deviations as compared with the historical time series. We have considered the variation of SLHF as an anomaly only when its value is above 2 standard deviations from the historical time series. Figure 1 shows many instances where the SLHF is higher than the historical time series. There is an increase in the SLHF on the 53rd, 54th, and 57th days, with a value of 125.167 W/m^2, 123.4 W/m^2, and 83.36 W/m^2, respectively, greater than 2σ from the mean historical time series. Again, it was found that the SLHF values rise from the 39th to the 42nd and the 46th to the 48th days, with the average values of SLHF being ~134.55 W/m^2, and ~141.033 W/m^2, respectively. It is clearly observed that the maximum numbers of anomalies in SLHF as precursory signatures are present before the ∽20 days from the earthquake day.

Table 1. Details on the earthquakes considered in the present study

Sr. No.	Location	Event date and time (UTC)	Epicentre (Lat. Long.)	Magnitude	Focal depth (Km)
1	Biak, Indonesia	10.09.2022 (00:05:12)	2.23° S, 138.17° E	6.2	21
2	Papua, Indonesia	09.09.2022 (23:31:47)	2.24° S, 138.19° E	6.2	18
3	Ternate, Indonesia	03.06.2021 (10:09:58)	0.31° N, 126.29° E	6.2	26
4	Padang, Indonesia	17.11.2020 (01:44:11)	2.67° S, 99.32° E	6.0	19
5	Ternate, Indonesia	14.11.2019 (16:17:40)	1.62° N, 126.41° E	7.1	33
6	Assam, India	28.04.2021 (02:21:26)	26.78° N, 92.45° E	6.0	34
7	Kathmandu, Nepal	12.05.2015 (07:05:19)	27.8 ° N, 86.06° E	7.3	15

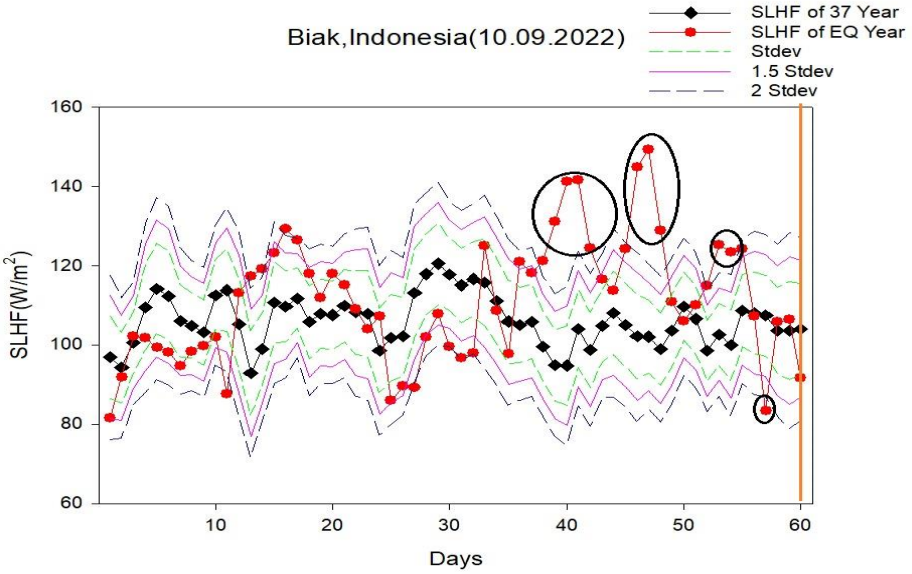

Figure 1. Representation of surface latent heat flux during the earthquake year 2022 (red circle) vs. mean historical time series 1985-2021 (black diamond) during the earthquake events that occurred in Biak, Indonesia (10.09.2022), epicentre (2.23° S, 138.17° E). Coloured lines indicate 1.0 (green), 1.5 (pink), and 2.0 (blue) standard deviation from the mean- historical time series, respectively. The orange line shows earthquake day.

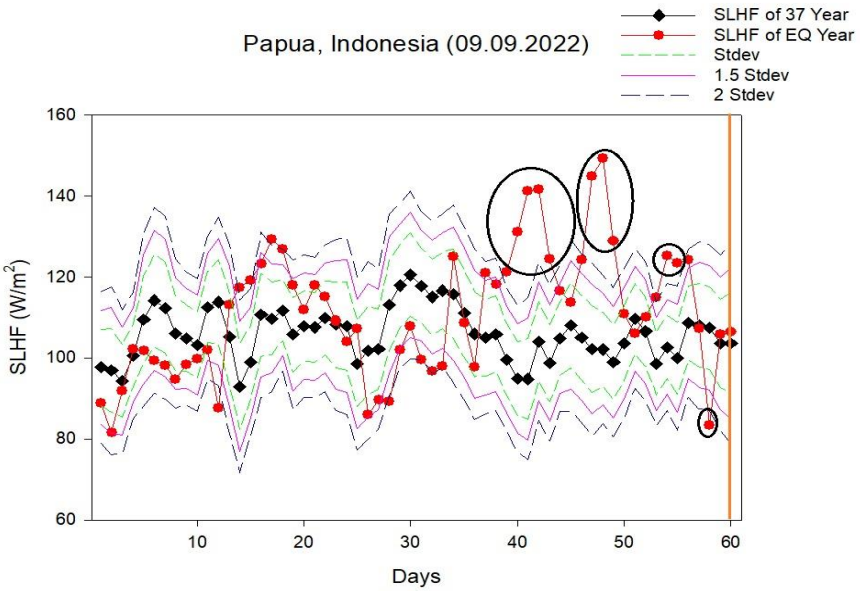

Figure 2. Representation of surface latent heat flux during the earthquake year 2022 (red circle) vs. mean historical time series 1985-2021 (black diamond) during the earthquake events that occurred in Papua, Indonesia (09.09.2022), epicentre (2.24° S, 138.19° E). Coloured lines indicate 1.0 (green), 1.5 (pink) and 2.0 (blue) standard deviation from the mean- historical time series, respectively. The orange line shows earthquake day.

The earthquake that occurred on 9 September 2022, had a magnitude of 6.2 with a depth of 18.0 km (epicentre 2.24° S and 138.19° E) in Papua, Indonesia. The variation in SLHF has been analysed for the purpose of identifying precursory signatures during the earthquake event. Figure 2 compares the earthquake year 2022 vs. mean historical time series in 1985–2021 during the earthquake events that occurred. From Figure 2, one can observe many instances where the SLHF is higher than the historical time series. There is an increase in the SLHF on the 54th, 55th, and 58th, days with a value of SLHF being 125.167 W/m^2, 123.4 W/m^2, and 83.36 W/m^2, respectively of greater than 2σ from the mean historical time series. Again, it was found that the SLHF values rise from the 40th to 43rd days, and from the 47th to the 49th, with the average values of SLHF being ~134.55 W/m^2, and ~141.033 W/m^2, respectively. It is clearly observed that the maximum numbers of anomalies in SLHF as precursory signatures are present before ~20 days from the earthquake day.

The earthquake that occurred on 3 June 2021, had a magnitude of 6.2 with a depth of 26.0 km (epicentre 0.31° S and 126.29° E) in Ternate, Indonesia. Figure 3 compares the earthquake year 2021 vs. mean historical time series in 1984–2020 during the earthquake events that occurred. The 37-year historical time series and the earthquake year are indicated in Figure 3 by the black line with a diamond and the red line with a circle, respectively. Figure 3 shows many instances in which the SLHF exceeds the historical time series. There is an increase in the SLHF on the 1st, 8th to 15th, 46th, 48th, 50th, 57th, 59th and 60th, days with a value of SLHF being 107.02 W/m^2, 125.89 W/m^2, 69.96 W/m^2, 81.33 W/m^2, 74.73 W/m^2, 82.7 W/m^2, 84.53 W/m^2 and 76.82 W/m^2, respectively of greater than 2σ from the mean historical time series. Several days show the anomalous behaviour of SLHF during the pre-earthquake period. It is clear that from Figure 3 before ~60 days from the earthquake day, the highest numbers of anomalies in SLHF as precursory signatures are observed.

The earthquake occurred on 17 Nov 2020, of magnitude 6.0 (epicentre 2.67° S, 99.32° E), and a depth of 19.0 km in Padang, Indonesia. Figure 4 shows a comparison the earthquake year 2021 vs. mean historical time series in 1984–2020 during the earthquake events that occurred. In Figure 4, the red line with a circle and the black line with a diamond denote the earthquake year and a historical time series of 37 years, respectively. SLHF is greater than 2σ on the 33rd and 56th to 59th day, with average SLHF values of ~124.381 W/m^2 and ~70.84 W/m^2, respectively from the mean historical time series. It is clear to see that before ~20 days from the earthquake day, the highest numbers of anomalies in SLHF as precursory signatures are observed.

On 14 November 2019, a magnitude 7.1 (epicentre 1.62° N, 126.41° E), earthquake occurred in Ternate, Indonesia, at a depth of 33.0 km. Figure 5 shows a comparison the earthquake year 2019 vs. mean historical time series in 1982–2018 during the earthquake events that occurred. In Figure 5, the red line with a circle and the black line with a diamond denote the earthquake year and a historical time series of 37 years, respectively. This figure shows that SLHF is greater than 2σ on the 43rd, and 58th day with the average values of SLHF being ~77.81 W/m^2, and ~115.803 W/m^2, respectively of the mean historical time series. It was found that the SLHF values rise from the days of the 38th to 41st, and the 50th to 53rd, days with the average values of SLHF being ~84.21 W/m^2, and ~129.09 W/m^2, respectively. It is clearly observed that the maximum numbers of anomalies in SLHF as precursory signatures are present before ~20 days from the earthquake day.

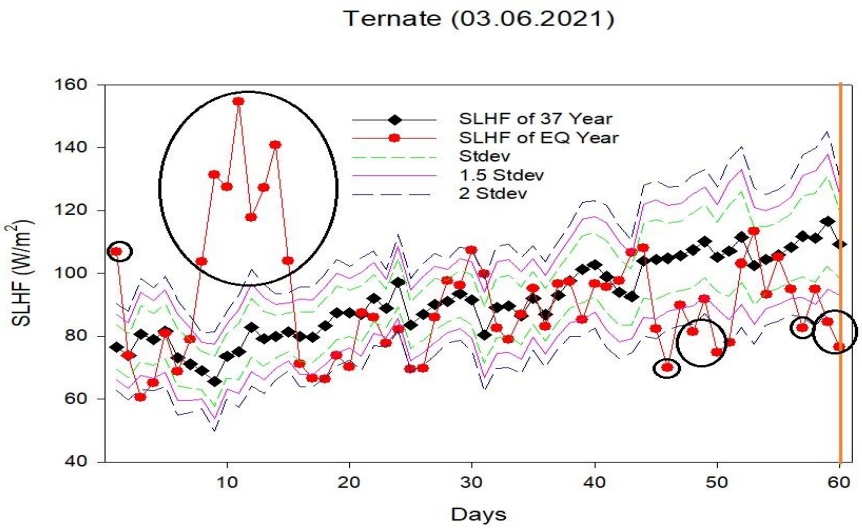

Figure 3. Representation of surface latent heat flux during the earthquake year 2021 (red circle) vs. mean historical time series 1984-2020 (black diamond) during the earthquake events that occurred in Ternate, Indonesia (03.06.2021), epicentre (0.31° S, 126.29° E). Coloured lines indicate 1.0 (green), 1.5 (pink) and 2.0 (blue) standard deviation from the mean- historical time series, respectively. The orange line shows earthquake day.

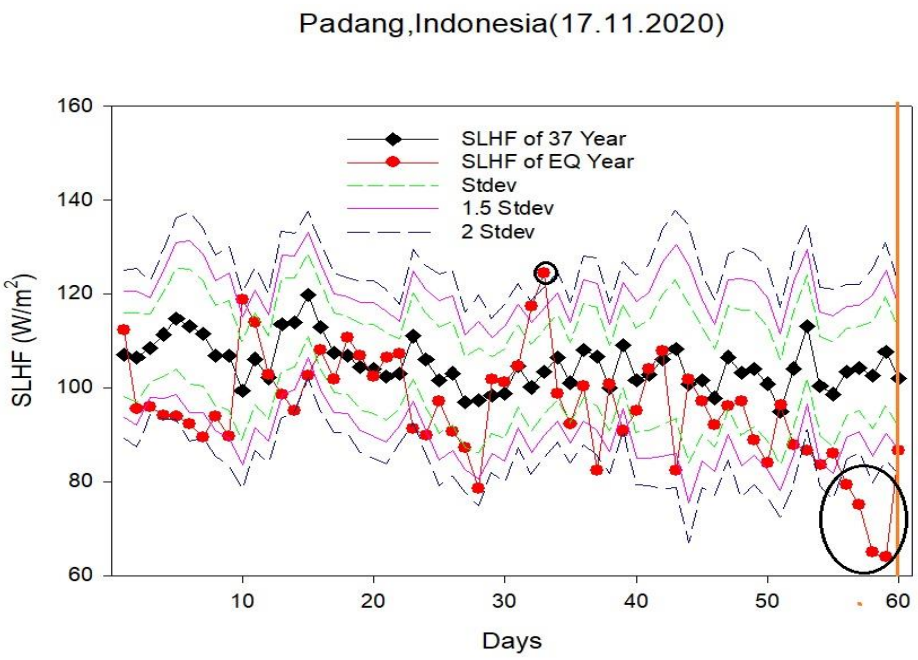

Figure 4. Representation of surface latent heat flux (SLHF) during the earthquake year (red circle) -2020 vs. mean historical time series 1983-2019 (black diamond) during the earthquake events that occurred in Padang, Indonesia (17.11.2020), epicentre (2.67° S, 99.32° E). Coloured lines indicate 1.0 (green), 1.5 (pink) and 2.0 (blue) standard deviation from the mean- historical time series, respectively. The orange line shows earthquake day.

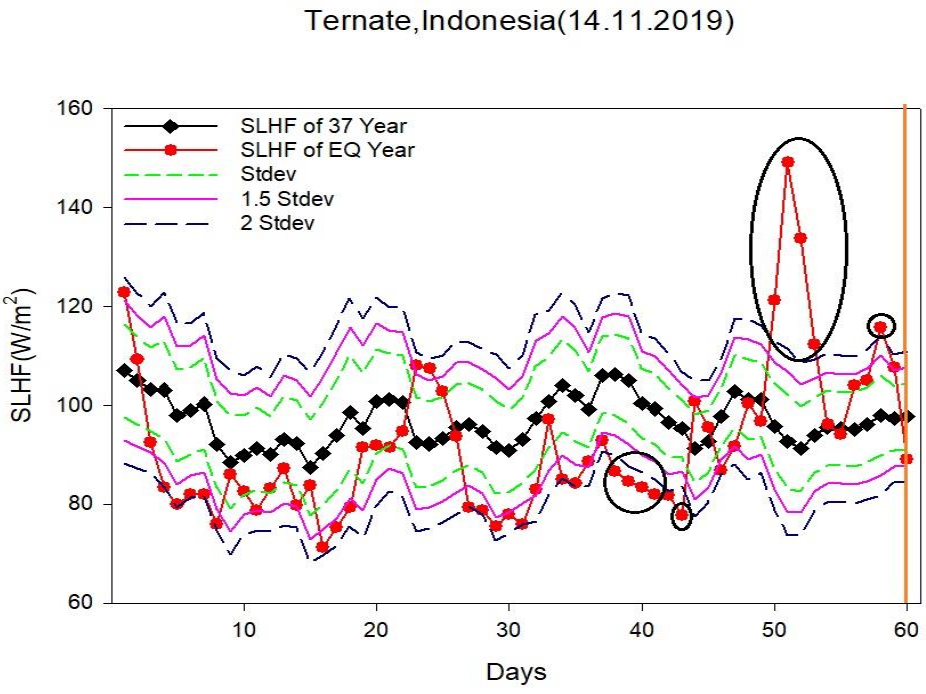

Figure 5. Representation of surface latent heat flux during the earthquake year 2019 (red circle) vs. mean historical time series 1982-2018 (black diamond) during the earthquake events that occurred in Ternate, Indonesia (14.11.2019), epicentre (1.62° N, 126.41° E). Coloured lines indicate 1.0 (green), 1.5 (pink) and 2.0 (blue) standard deviation from the mean- historical time series, respectively. The orange line shows earthquake day.

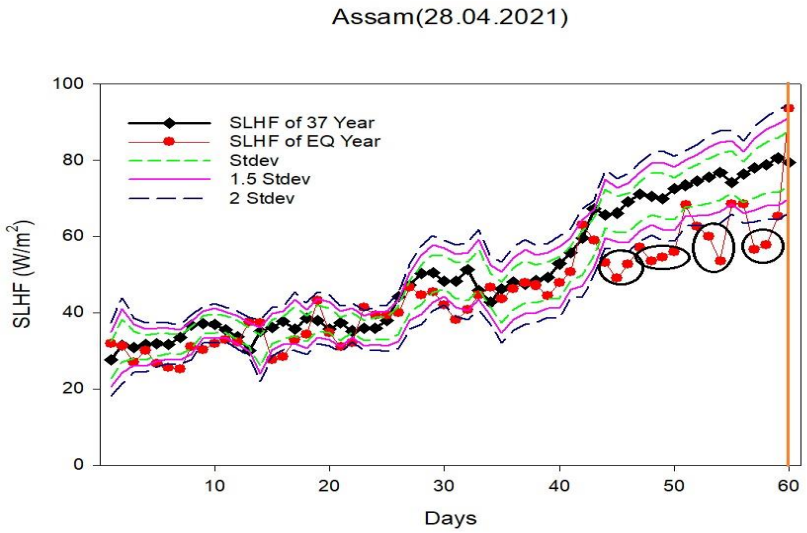

Figure 6. Representation of surface latent heat flux during the earthquake year 2021 (red circle) vs. mean historical time series 1984-2020 (black diamond) during the earthquake events that occurred in Assam (28.04.2021), epicentre (26.78° N, 92.45° E). Coloured lines indicate 1.0 (green), 1.5 (pink) and 2.0 (blue) standard deviation from the mean- historical time series, respectively. The orange line shows earthquake day.

The next earthquake considered is Dhekiajuli, Assam, India, on 28 April 2021, with magnitude 6.0 (epicentre 26.78° N, 92.45° E), and a depth of 34.0 km. Figure 6 shows a comparison the earthquake year 2021 vs. mean historical time series in 1984–2020 during the earthquake events that occurred. In Figure 6, the red line with a circle and the black line with a diamond denote the earthquake year and a historical time series of 37 years, respectively. From Figure 6, one can observe many instances where the SLHF is higher than the historical time series. The variation in the SLHF on the 53rd, 54th, 57th, and 58th days with a value of SLHF being 60 W/m^2, 53.52 W/m^2, 56.6 W/m^2, and 57.76 W/m^2, respectively of greater than 2σ from the mean historical time series. Again, it was found that the SLHF values rise from the 44th to 46th and 48th to 50th days, with the average values of SLHF being ~51.56 W/m^2 and ~54.64 W/m^2 respectively. It is clearly observed that the maximum number of anomalies in SLHF as precursory signatures is present before ~20 days from the earthquake day.

The earthquake occurred on 12 May 2015, of magnitude 7.3 (epicentre 27.80° S, 88.06° E), and at a depth of 15.0 km in Kathmandu, Nepal. This earthquake experienced lot of destruction and havoc owing to high magnitude and low depth. Figure 7 shows a comparison of the time series for the year 2015 with the historical time series years 1978-2014 of SLHF. It also shows a comparison with the earthquake year 2021 vs. mean historical time series in 1984–2020 during the earthquake events that occurred. In this figure, the red line with a circle and the black line with a diamond denote the earthquake year and a historical time series of 37 years, respectively. Initially, SLHF is greater than 2σ on the 6th to 8th, 10th, 11th, 15th, 16th, 26th, 34th, 38th, and 39th day from the mean historical time series. Several times during the two months preceding the earthquake, the SLHF was greater than two standard deviations. However, the frequency of the aforementioned events is greatest on the 18th to 24th, 28th to 32nd, 41st to 48th and 52nd to 54th day, with average SLHF values of ~50.37 W/m^2, ~59.228 W/m^2, 60.806 W/m^2 and 67.57 W/m^2, respectively. It is clear to see that before ~50 days from the earthquake day, the highest numbers of anomalies in SLHF as precursory signatures are observed. It is further interesting to note that the anomalies during Ternate, Indonesia (03.06.2021) and Kathmandu, Nepal (12.05.2015) were observed ∽60 days and ∽50 days, respectively before the earthquake events. This behaviour was quite different from previously discussed earthquake events.

In all the earthquake events, anomalies behaviour of SLHF as precursory signature was observed. There were many days when the values of SLHF was greater than 2 standard deviation from the historical time series. In all the events, the SLHF increased ∽20 days before the earthquake day except the ternate, Indonesia (03.06.2021) and Kathmandu, Nepal (12.05.2015). During Ternate, Indonesia (03.06.2021) earthquake events the values of SLHF 107.02 W/m^2, 125.89 W/m^2, 69.96 W/m^2, 81.33 W/m^2, 74.73 W/m^2, 82.7 W/m^2, 84.53 W/m^2 and 76.82 W/m^2, respectively observed ∽60 days before the earthquake day. During Kathmandu, Nepal events with average SLHF values of ~50.37 W/m^2, ~59.228 W/m^2, 60.806 W/m^2 and 67.57 W/m^2, respectively observed ∽50 days before the earthquake day. The thermal infrared (IR) around the epicentre and nearby regions may have contributed to the rise in SLHF before the major seismic event. From the figures, one can notice that the anomalous SLHF behaviour during all the events.

In the present work, we have also analysed the maximum anomaly and minimum anomaly in SLHF during all the earthquake events.

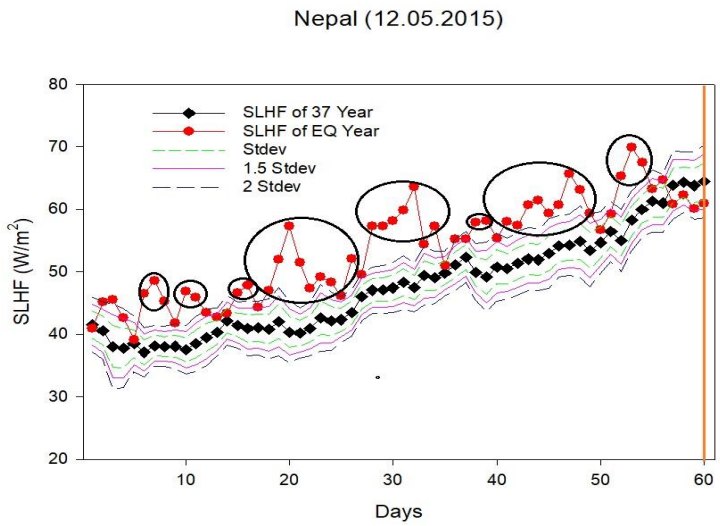

Figure 7. Representation of surface latent heat flux during the earthquake year 2015 (red circle) - vs. mean historical time series 1978-2014 (black diamond) during the earthquake events that occurred in Kathmandu, Nepal (12.05.2015), epicentre (27.80° S, 88.06° E). Coloured lines indicate 1.0 (green), 1.5 (pink) and 2.0 (blue) standard deviation from the mean- historical time series, respectively. The orange line shows earthquake day.

Table 2A. Details of maximum anomaly in SLHF during all the earthquake events

Events	Locations & epicentre (lat., long.)	Event date & time (UTC)	Maximum anomaly day (*D*)	Value of SLHF during earthquake year (*X*)	Value of SLHF corresponding day of historical time series (*Y*)	*X/Y*
1	Biak, Indonesia (2.23° S, 138.17° E)	10.09.2022 (00:05:12)	47th	149.33	102.10	1.46
2	Papua, Indonesia (2.24° S, 138.19° E)	09.09.2022 (23:31:47)	48th	149.33	102.10	1.46
3	Ternate, Indonesia (0.3° N, 126.29° E)	03.06.2021 (10:09:58)	11th	154.56	75.16	2.05
4	Padang, Indonesia (2.67° S, 99.32° E)	17.11.2020 (01:44:11)	33rd	124.28	103.37	1.20
5	Ternate, Indonesia (1.62° N, 126.41° E)	14.11.2019 (16:17:40)	51st	149.08	92.67	1.60
6	Assam, India (26.78° N, 92.45° E)	28.04.2021 (02:21:26)	53rd	60	75.59	0.79
7	Kathmandu, Nepal (27.80° N, 86.0° E)	12.05.2015 (07:05:19)	53rd	69.92	58.25	1.20

Table 2B. Details of minimum anomaly in SLHF during all the earthquake events

Events	Locations & Epicentre (lat., long.)	Event date & time (UTC)	Minimum anomaly day (*D′*)	Value of SLHF during earthquake year (*X′*)	Value of SLHF corresponding day of historical time series (*Y′*)	*X′/Y′*
1	Biak, Indonesia (2.23° S, 138.17° E)	10.09.2022 (00:05:12)	57th	83.36	107.4	0.77
2	Papua, Indonesia (2.24° S, 138.19° E)	09.09.2022 (23:31:47)	58th	83.36	107.4	0.77
3	Ternate, Indonesia (0.31° N, 126.29° E)	03.06.2021 (10:09:58)	46th	69.96	104.80	0.66
4	Padang, Indonesia (2.67° S, 99.32° E)	17.11.2020 (01:44:11)	59th	64	107.68	0.59
5	Ternate, Indonesia (1.62° N, 126.41° E)	14.11.2019 (16:17:40)	43rd	77.81	95.31	0.81
6	Assam, India (26.78° N, 92.45° E)	28.04.2021 (02:21:26)	45th	48.96	66.11	0.74
7	Kathmandu, Nepal (27.80° N, 86.06° E)	12.05.2015 (07:05:19)	8th	45.26	38.07	1.18

Table 2A provides the details of the maximum anomaly in SLHF during all the earthquake events. Parameter *D* (Table 2A) represents the day when the maximum anomaly in SHLF during the EQ year was observed compared to the historical time series. *X* and *Y* represent the magnitude values of SLHF corresponding to *D* during the EQ year and historical time series respectively. *X/Y* gives the extent of maximum anomaly of SLHF during EQ year compared to the historical time series corresponding to day *D*.

During the first earthquake event (Table 2A) (date: 10.09.2022, epicentre: 2.23^{0} S, 138.17^{0} E), the value of *X* (highest value of anomaly in SLHF during the earthquake year), is 149.33 W/m^2 (47th day), and the value of SLHF during the 47th day of the mean historical time series Y is 102.107 W/m^2. Therefore, the maximum anomaly in SLHF is 1.46 times greater than the historical time series. During the second earthquake event (date: 09.09.2022), the value of *X* (highest value of anomaly in SLHF during the earthquake year), is 149.33 W/m^2 (48th day), and the value of SLHF during the 48th day of the mean historical time series *Y* is 102.107 W/m^2. In the third earthquake event (date: 03.06.2021), the value of *X* is 154.56 W/m^2 (11th day), and the value of SLHF during the 11th day of the mean historical time series *Y* is 75.16 W/m^2. During the fourth earthquake event (date: 17.11.2020), the value of *X* is 124.28W/m^2 (33rd day), and the value of SLHF during the 33rd day of the mean historical time series *Y* is 103.37 W/m^2. In comparison, in the fifth earthquake event (date: 14.11.2019), the values of *X* is 149.08 W/m^2 (51st day) and the value of SLHF during the 51st day of the mean historical time series *Y* is 92.67 W/m^2. In the sixth earthquake event (date: 28.04.2021), the value of *X* (highest value of anomaly in SLHF during the earthquake year), is 60 W/m^2 (53rd day), and the value of SLHF during the 53rd day of the mean historical time series *Y* is 75.59 W/m^2. Similarly, in the seventh event (date: 12.05.2015), the value of *X* is 69.92 W/m^2 (53rd day), and the corresponding 53rd day of the mean historical time series *Y* is 58.25 W/m^2. Therefore, we find that the maximum anomaly in SLHF is 1.46, 2.05, 1.20, 1.60, 0.79, and 1.20 times greater during the earthquake year compared to the historical time series during 2nd, 3rd, 4th, 5th, 6th, and 7th earthquake events in consideration respectively. Figure 8, represents the extant of maximum anomalies during all the seven earthquake events (black bars).

In comparison to the above, Table 2B provides the details of the minimum anomaly in SHLF during all the earthquake events. Parameter *D′* represents the day when the maximum anomaly in SLHF during the EQ year was observed compared to the historical time series. *X′* and *Y′* represent the magnitude values of SLHF corresponding to *D′* during the EQ year and historical time series respectively. *X′/Y′* gives the extent of minimum anomaly of SLHF during EQ year compared to the historical time series corresponding to day *D′*. During the first earthquake event (Table 2B) (date: 10.09.2022), the lowest value of the anomaly in the SLHF during the earthquake year is 83.36 W/m^2 (57th day), and the value of the SLHF on the 57th day of the mean historical time series *Y′* is 107.4 W/m^2. On the second earthquake event (date: 09.09.2022), 58th day of the mean historical time series *Y′*, the value of SLHF is 107.4 W/m^2, while the value of *X′* (lowest value of anomaly in SLHF throughout the earthquake year), is 83.36 W/m^2. In the third (date: 03.06.2021), the value of *X′* (lowest value of anomaly in SLHF during the earthquake year), is 69.96 W/m^2 (46th day), and the value of SLHF on the 46th day of the mean historical time series *Y′* is 104.80 W/m^2. In the fourth earthquake event (date: 17.11.2020), the value of SLHF on the 59th day of the mean historical time series *Y′* is 107.68 W/m^2, while the value of *X′* (lowest value of anomaly in SLHF during the earthquake year), is 64 W/m^2 (59th day). Similarly, in the fifth earthquake event (date: 14.11.2019), the value of SLHF on day 43rd of the mean historical time series *Y′* is 95.31 W/m^2, while *X′* (lowest value of anomaly in SLHF during the earthquake year), is 77.81 W/m^2. In comparison, during sixth earthquake event (date: 28.04.2021), the value of *Y′* is 66.11 W/m^2, while *X′* is 48.96 W/m^2. During the seventh event also (date: 12.05.2015), the *Y′* is 38.07 W/m^2, and the value of *X′* (lowest value of anomaly in SLHF during the earthquake year), is 45.26 W/m^2. Therefore, the minimum anomaly in SLHF is 0.77, 0.77, 0.66, 0.59, 0.81, 0.74, and 1.18 times greater during the earthquake year compared to the historical time series during 1st, 2nd, 3rd, 4th, 5th, 6th, and 7th earthquake events in consideration respectively. Figure 8, represents the extant of minimum anomalies during all the seven earthquake events (red bars).

Table 2C and Figure 8 provide a comprehensive overview of the maximum and minimum anomalous increase of SLHF during all the earthquakes. The observed maximum and minimum anomalous increase in SLHF spanned from 0.79 to 2.05 and 0.59 to 1.18 times greater during the earthquake years respectively, compared to historical time series during all the seven earthquake events. From the above analysis, it can be inferred that the range of deviation of anomaly of SLHF is the least on the earthquake events that occurred on land. However, this range of deviation is much more for the earthquake events that lie near the vicinity of the ocean/ocean.

The SLHF is widely known to be affected by a variety of meteorological characteristics such as temperature, humidity, moisture levels, geographical region of observation, period of the year, the season under discussion, monsoon, winds in the region, and floods (Dey and Singh, 2003). The surface temperature and humidity-derived SLHF represent the latent heat process, which is particularly related to water evaporation. The earthquakes under discussion had distinct origins; 2 of the epicentres were on land, and others near the ocean or in the ocean. It is observed that SLHF showed anomalous precursory signatures during all events. They did, however, exhibit distinct behavioural traits. This might be attributed to differences in geographical locations, as well as differences in metrological factors.

Table 2C. Maximum/minimum anomaly in SLHF during all the earthquake events

Events	Locations & epicentre (lat., long.)	Event date & time (UTC)	*X/Y*	*X′/Y′*
1	Biak, Indonesia (2.23° S, 138.17° E)	10.09.2022 (00:05:12)	1.46	0.77
2	Papua, Indonesia (2.24° S, 138.19° E)	09.09.2022 (23:31:47)	1.46	0.77
3	Ternate, Indonesia (0.31° N, 126.29° E)	03.06.2021 (10:09:58)	2.05	0.66
4	Padang, Indonesia (2.67° S, 99.32° E)	17.11.2020 (01:44:11)	1.20	0.59
5	Ternate, Indonesia (1.62° N, 126.41° E)	14.11.2019 (16:17:40)	1.60	0.81
6	Assam, India (26.78° N, 92.45° E)	28.04.2021 (02:21:26)	0.79	0.74
7	Kathmandu, Nepal (27.80° N, 86.06° E)	12.05.2015 (07:05:19)	1.20	1.18

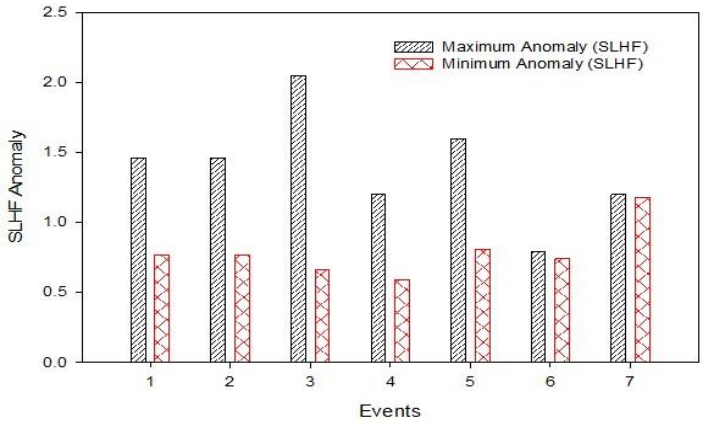

Figure 8. Representation of maximum (black bars) and minimum (red bars) deviation in anomalies of SLHF during all the seven earthquake events (EQs)

The heat transfer rate through the ocean, as well as through the fluid present in the soil pores, is the quickest way to attribute the transfer of major SLHF contrast zones all throughout the ocean and in epicentral locations. Because ocean water allows for faster heat conduction, the SLHF contrast is more likely to extend throughout the sea, whereas limited heat conduction through pore fluid in rocks and soils causes the SLHF contrast to be observed over smaller land regions. The SLHF anomaly, on the other hand, appears to indicate increased values following the major earthquakes. The magnitude of the SLHF changes associated with these seven earthquakes is likely related to the earthquake location, and epicentre proximity to the ocean, earthquake seasons, and the strong interaction between the land, ocean, and atmosphere. The nature of such a correlation, as well as the underlying physical processes, remains uncertain. Before the earthquake, a rise in infrared heat (IR) across the epicentral area caused intense land-ocean atmospheric interactions, resulting in anomalous SLHF. The increase in infrared temperature just before the earthquake is thought to be mostly due to the accumulation of stress days before the earthquake in the epicentral area. In short, the focal depth earthquakes and the manifestation of stress accumulation, is due to surface temperature and SLHF is distinct. The variance in SLHF is most likely due to non-equilibrium in the geochemical transition caused by stress accumulation (Bina, 1998). The significant anomalous changes in the SLHF were observed during all the events in consideration. Further, the anomalies are observed within the span of ∽20 days before the earthquake day. Tronin et al. (2002) observed increase in SLHF 2-7 days before an earthquake owing to fluids present in the Earth's crust and increased interaction between land, ocean and atmosphere.

The unusual accumulation of water vapour concentrations in the atmosphere before earthquake events occurs due to increased interactions between land, ocean and atmosphere is reported by Dey and Singh (2003). Earth's outgoing infrared radiation further increases the heat near the surface (Tronin et al., 2002) that results in increased SLHF values before the earthquakes. Just after the main seismic activity, the built-up stress is released, and SLHF falls rapidly. The transfer of energy to the atmosphere is enhanced by the greater moisture levels in the surrounding environment.

CONCLUSIONS

In the present work the surface thermal parameter - SLHF has been analysed for recent seven high magnitudes (M≥6.0) earthquakes as a precursory signature of earthquakes. The following conclusions may be drawn from the present study.

(i) SLHF values during all the seven earthquake events show anomalous increase during earthquake affected period.

(ii) Generally, the anomalies in SLHF values are observed within a span of ∽20 days prior to earthquakes.

(iii) The maximum anomalous increase in SLHF is 0.79 to 2.05 times greater during the earthquake years compared to historical time series during all the seven earthquake events.

(iv) The minimum anomalous increase in SLHF is 0.59 to 1.18 times greater during the earthquake years compared to historical time series during all the seven earthquake events.

(v) The variation of maximum and minimum anomaly of SLHF is highest for the earthquake that occurred over the ocean/near the ocean. This variation is almost negligible for the earthquakes that occurred over the land.

(vi) The outgoing radiation trapped via accumulated water vapours, results in the increased heat over the surface of epicentres and nearby areas. This further, contributes to the rise in surface latent heat flux before all the major earthquake events.

Acknowledgements

The authors are grateful to NCEP-NCAR website for providing the data of Surface Latent Heat Flux (SLHF). The authors also thank the United States Geological Survey (USGS) team site for sharing earthquake information.

Author Credit Statement

Pooja Sharma, Ananna Bardhan and D.K. Sharma: Problem identification and data analysis. All the authors jointly wrote the paper

Data Availability

The availability of data and the website information are given in the paper

Compliance with Ethical standards

The authors declare no conflict of interest and adhere to copy right norms

References

Aggarwal, M., Sharma, D.K. and Bardhan, A., 2016. Preliminary studies of ionospheric behavior during a seismic event of Mw~ 6.9 at Qinghai station (geog. 33.19 N, 96.75 E). J. Ind. Geophys. Union, 2, 127-132.

Bardhan, A., Khurana, M.S., Bahal, B.M., Aggarwal, M. and Sharma, D.K., 2017. Ion density and temperature variations at altitude of 500 km during moderate seismic activity. Adv. Space Res., 59, 1023-1032.

Beig, G., Chate, D.M., Ghude, S.D., Ali, K., Satpute, T., Sahu, S.K., Parkhi, N. and Trimbake, H.K., 2013. Evaluating population exposure to environmental pollutants during Deepavali fireworks displays using air quality measurements of the SAFAR network. Chemosphere, 92(1), 116-124.

Biagi, P.F., Piccolo, R., Ermini, A., Martellucci, S., Bellecci, C., Hayakawa, M., Capozzi, V.I.T.O. and Kingsley, S.P., 2001. Possible earthquake precursors revealed by LF radio signals. Natural Hazards and Earth Sys. Sci., 1(1/2), 99-104.

Bina, C.R., 1998. A note on latent heat release from disequilibrium phase transformations and deep seismogenesis. Earth planets and space, 50, 1029-1034.

Brohan, P., Kennedy, J.J., Harris, I., Tett, S.F. and Jones, P.D., 2006. Uncertainty estimates in regional and global observed temperature changes: A new data set from 1850. J. Geophys. Res., Atmospheres, 111, D12106, doi:10.1029/2005JD006548,

Chan, C.H. and Wu, Y.M., 2012. A seismicity burst following the 2010 M 6.4 Jiashian earthquake–implications for short-term seismic hazards in southern Taiwan. J. Asian Earth Sci., 59, 231-239.

Chauhan, A., Kumar, R. and Singh, R.P., 2018. Coupling between land–ocean–atmosphere and pronounced changes in atmospheric/meteorological parameters associated with the Hudhud Cyclone of October 2014. Int. J. Environ. Res. Public Health, 15(12), 2759.

Chowdary, J.S., Xie, S.P., Tokinaga, H., Okumura, Y.M., Kubota, H., Johnson, N. and Zheng, X.T., 2012. Interdecadal variations in ENSO teleconnection to the Indo–western Pacific for 1870–2007. J. Climate, 25(5), 1722-1744.

Conti, L., Picozza, P. and Sotgiu, A., 2021. A critical review of ground based observations of earthquake precursors. Frontiers in Earth Sci., 9, 676766.

Dey, S. and Singh, R.P., 2003. Surface latent heat flux as an earthquake precursor. Natural Hazards and Earth Sys. Sci., 3(6), 749-755.

Dobrovolsky, I.P., Zubkov, S.I. and Miachkin, V.I., 1979. Estimation of the size of earthquake preparation zones. Pure App. Geophys., 117(5), 1025-1044.

Freund, F. and Ouzounov, D.: EOS Trans. AGU, Fall Meet. Suppl. Abstract, 82(47), 2001.

Ghosh, S., Chowdhury, S., Kundu, S., Sasmal, S., Politis, D.Z., Potirakis, S.M., Hayakawa, M., Chakraborty, S. and Chakrabarti, S.K., 2021. Unusual surface latent heat flux variations and their critical dynamics revealed before strong earthquakes. Entropy, 24(1), 23. https://doi.org/10.3390/e24010023

González-Zamora, Á., Sánchez, N., Martínez-Fernández, J., Gumuzzio, Á., Piles, M. and Olmedo, E., 2015. Long-term SMOS soil moisture products: A comprehensive evaluation across scales and methods in the Duero Basin (Spain). Phys. Chem. Earth, Parts A/B/C, 83, 123-136.

Holliday, J.R., Turcotte, D.L. and Rundle, J.B., 2008. Self-similar branching of aftershock sequences. Physica A: Statistical Mechanics and its Applications, 387(4), 933-943.

Huang, J., Niu, F., Gordon, R.G. and Cui, C., 2015. Accurate focal depth determination of oceanic earthquakes using water-column reverberation and some implications for the shrinking plate hypothesis. Earth Planet. Sci. Lett., 432, 133-141.

Knopoff, L., 1996. Earthquake prediction: the scientific challenge. Proc. National Academy of Sciences, 93(9),

3719-3720.

Kumar, A., 2016. Spatio-temporal synoptic variability of aerosol optical depth and cloud properties over the Central North region of India through MODIS collection V satellite sensors. Indian J. Physics, 90, 613-625.

Kumar, A., 2021. Long term (1975-2016) anomaly of surface latent heat flux (SLHF) over Indian subcontinent: Signatures of early warning of earthquake disasters. Indian J. Radio & Space Physics (IJRSP), 49(1-2), 19-27.

Kumar, A. and Singh, H.P., 2013. Impact of high energy cosmic rays on global atmospheric electrical parameters over different orographically important places of India. Int. Scholarly Res. Notices, Article ID 831431, https://doi.org/10.1155/2013/831431

Kumar, A. and Singh, D., 2014. A comparative study on orographic and latitudinal features of global atmospheric electrical parameters over different places at three Asian countries. Indian J. Physics, 88, 225-235.

Kumar, A., Saxena, D. and Yadav, R., 2011. Measurements of atmospheric aerosol concentration of various sizes during monsoon season at Roorkee, India. Atmospheric Sci. Lett., 12(4), 345-350.

Merzer, M.O.S.H.E. and Klemperer, S.L., 1997. Modeling low-frequency magnetic-field precursors to the Loma Prieta earthquake with a precursory increase in fault-zone conductivity. Pure App. Geophys., 150, 217-248.

Molchanov, O., Kulchitsky, A. and Hayakawa, M., 2001. Inductive seismo-electromagnetic effect in relation to seismogenic ULF emission. Natural Hazards and Earth Sys. Sci., 1(1/2), 61-67.

Ohta, K., Umeda, K., Watanabe, N. and Hayakawa, M., 2001. ULF/ELF emissions observed in Japan, possibly associated with the Chi-Chi earthquake in Taiwan. Natural Hazards and Earth Sys. Sci., 1(1/2), 37-42.

Oikonomou, C., Haralambous, H., Pulinets, S., Khadka, A., Paudel, S.R., Barta, V., Muslim, B., Kourtidis, K., Karagioras, A. and İnyurt, S., 2020. Investigation of pre-earthquake ionospheric and atmospheric disturbances for three large earthquakes in Mexico. Geosciences, 11(1), 16.

Piscini, A., De Santis, A., Marchetti, D. and Cianchini, G., 2017. A Multi-parametric climatological approach to study the 2016 Amatrice–Norcia (Central Italy) earthquake preparatory phase. Pure Appl. Geophys., 174, 3673-3688.

Piscini, A., Marchetti, D. and De Santis, A., 2019. Multi-parametric climatological analysis associated with global significant volcanic eruptions during 2002–2017. Pure App. Geophys., 176, 3629-364.

Potirakis, S.M., Contoyiannis, Y., Schekotov, A., Eftaxias, K. and Hayakawa, M., 2021. Evidence of critical dynamics in various electromagnetic precursors. The European Physical Journal Special Topics, 230, 151-177.

Pulinets, S. and Ouzounov, D., 2011. Lithosphere–Atmosphere–Ionosphere Coupling (LAIC) model–An unified concept for earthquake precursors validation. J. Asian Earth Sci., 41(4-5), 371-382.

Ruiz-Pinilla, J.G., Adam, J.M., Pérez-Cárcel, R., Yuste, J. and Moragues, J.J., 2016. Learning from RC building structures damaged by the earthquake in Lorca, Spain, in 2011. Engineering Failure Analysis, 68, 76-86.

Sasmal, S., Chowdhury, S., Kundu, S., Politis, D.Z., Potirakis, S.M., Balasis, G., Hayakawa, M. and Chakrabarti, S.K., 2021. Pre-seismic irregularities during the 2020 Samos (Greece) earthquake (M= 6.9) as investigated from multi-parameter approach by ground and space-based techniques. Atmosphere, 12(8), 1059.

Schulz, J., Meywerk, J., Ewald, S. and Schlüssel, P., 1997. Evaluation of satellite-derived latent heat fluxes. J. Climate, 10(11), 2782-2795.

Sharma, D.K., Bardhan, A. and Rai, J., 2013. Ionospheric electron and ion temperatures response to seismic activity. Ind. J. of Radio & Space Phy. 42, 18-26.

Singh, R.P., Sahoo, A.K., Bhoi, S., Kumar, M.G. and Bhuiyan, C., 2001. Ground deformation of the Gujarat earthquake of 26 January 2001. J. Geol.l Society India, 58(3), 209-214.

Tanimoto, T. and Heki, K., 2015. 4.16- Interaction of Solid Earth, Atmosphere and Ionosphere. Treatise on geophys., 421-443.

Tronin, A.A., 2000. Thermal IR satellite sensor data application for earthquake research in China. Int. J. Remote Sensing, 21(16), 3169-3177.

Tronin, A.A., Hayakawa, M. and Molchanov, O.A., 2002. Thermal IR satellite data application for earthquake research in Japan and China. J. Geodynamics, 33(4-5), 519-534.

Uyeda, S., Nagao, T., Hattori, K., Hayakawa, M., Miyaki, K., Molchanov, O., Gladychev, V., Baransky, L., Chtchekotov, A., Fedorov, E. and Pokhotelov, O., 2001. Geophysical Observatory in Kamchatka region for monitoring of phenomena connected with seismic activity. Natural Hazards and Earth Sys. Sci., 1(1/2), 3-7.

Zhang, W., Zhao, J., Wang, W., Ren, H., Chen, L. and Yan, G., 2013. A preliminary evaluation of surface latent heat flux as an earthquake precursor. Natural Hazards and Earth Sys. Sci., 13(10), 2639-2647.

Received on: 14-08-2023 ; Revised on: 06-03-2024; Accepted on: 13-03-2024

J. Ind. Geophys. Union, 28(2) (2024), 143-154

Impacts of tsunami on environment along the Indian coastlines: A comprehensive assessment

Babita Dani[1], Vaibhava Srivastava[1], A. P. Singh[2] and R. Bhatla[3,4*]
[1]Department of Geology, Institute of Science, Banaras Hindu University, Varanasi-221005, India.
[2]National Centre for Seismology, Ministry of Earth Sciences (MoES), New Delhi-110003, India.
[3]Department of Geophysics, Institute of Science, Banaras Hindu University, Varanasi-221005, India.
[4]DST-Mahamana Centre of Excellence in Climate Change Research, Institute of Environment and Sustainable Development, Banaras Hindu University, Varanasi-221005, India.
*Corresponding author: rbhatla@bhu.ac.in

ABSTRACT

An attempt is made to study the trends in research focusing mainly on the post-tsunami effects on the environment and their mitigation strategies thereof. These impacts are associated with both natural as well as anthropogenic aspects of the environment. Very few literatures are available online on the impacts on the physical or biological parameters of the environment over the Indian coast and there are very few baselines which are defined for environmental assessments. Assessment of the key impacts on the environment due to tsunami are found to be intrusion of salt water which may pose threats to the soil, vegetation, and salinization of freshwater resources. Solid waste and disaster debris (hazardous materials and toxic substances) are also the utmost critical environmental issue. There are many post-tsunami anthropogenic threats also, such as coastal pollution, excess resource use, erosion of beaches and changes in landscapes. The aim of the study is to bring out to the understanding of impacts on the environment that have not been reported sufficiently in the existing literature, hence it is needed to study specifically. Also trying to find out ways that might be useful for rehabilitation of coastal environmental habitats. To quantify such environmental impacts, there is a need for a more pronounced understanding of impacts of the tsunami on the coastal belts. A better understanding of such environmental impacts is very crucial in defining coastal environmental management and further mitigation plans.

Keywords: Tsunami, Indian coasts, Environmental impacts, Mitigation strategies, Earthquake.

INTRODUCTION

Several observations have been reported on the impacts of the tsunami on the environment in many research studies. Tsunamis are a severe threat to coastal environment, even though they do not occur very frequently and mostly with little or no damage. But, the areas closest to the tsunami's origin, typically experience the most extensive destruction and loss of life. Flooding, wave impacts, erosion, powerful currents, and floating debris (e.g., automobiles, trees, structures, etc.) causes majority of the damage and the destruction. Those impacts are associated with both natural and anthropogenic aspects of the environment. Some of these impacts are loss of life, property damage, and biodiversity loss, as well as potential environmental risks such as seawater flooding into the land causing salinization issues in soil and fresh water resources, sediment deposition, and salt injuries to crops. Large-scale damage to infrastructure (houses and industrial sites), buildings, electric poles, towers, and roads etc. have been reported by UNEP (2005).

An earthquake that occurred on December 26, 2004, led to the deadliest tsunami ever recorded. According to the moment magnitude scale, the earthquake's magnitude was 9.3. During last few decades, many studies have been done to understand the impact of tsunamigenic earthquake along different coastal belts namely Iran, western coast of India, Sultanate of Oman and Makran coast of Pakistan etc. Generally, tsunamis do not arrive as ocean waves but rather as a huge, powerful and rapid rise in water levels that leads to an intense flooding (Shukla et al., 2010; Singh et al., 2012). The impacts of a tsunami on a shoreline might range from insignificant to catastrophic. Some of these impacts after the Indian Ocean tsunami (2004) on the features/structures near coastal areas with possible reasons are shown in the Table 1. The extent of these impacts depends on various factors, including the magnitude of the earthquake, the coastal geomorphology, and the proximity of human settlements. Tsunami may also have its direct and indirect impacts on the environment. Some of the significant impacts are mentioned in Table 1.

Direct Impacts

When tsunami waves reach extremely high, they continue to strike coastlines, resulting in severe destruction of properties, biodiversity loss, and fatalities. Direct impacts of tsunami on the environment are intrusion of salt water which may pose threats to the soil (affecting fertility of soil of agricultural lands), vegetation (salinization and contamination due to debris, can impact on the production in the medium and long term) and salinization of freshwater resources (rivers, wells, lakes, and fresh water resources) (Shukla et al., 2010; Singh et al., 2012). The loss of human lives which is one of the major and worst consequence of a tsunami. Tsunamis kill hundreds of thousands of people. More than 4 lakh people died as a result of tsunamis since 1850 alone. The violent intensity of tsunami causes immediate deaths mostly from drowning.

Table 1. Changes occurred in different features/structures at various locations after the 2004 Indian Ocean Tsunami.

Features/Structures	*Changes due to impacts of the 2004 Indian Ocean tsunami*	*Possible reasons*
Coastal vegetation	(i) Few frontal trees, herbs and shrubs were bent and uprooted (ii) Vegetation and crops near coastal areas got injured and died due to salt accumulation in the crop field.	They act as a barrier against tsunami wave and has protected natural impacts of extreme events. Hence, gets destroyed vastly.
Infrastructures/ buildings/ roads	(i) Not only houses and shops, but at many places, some villages also got destroyed completely and vanished (ii) Roads were covered with sand transported during the tsunami (iii) Towers and electric poles were crashed and distorted (iv) Some bridges and roads near coastal areas were dislocated	Improper and poor urban planning of the cities with narrow roads, smaller distance of electric poles and towers from the coasts may lead to rapid unregulated growth. Thus, making the area more vulnerable to various catastrophic natural hazards like Tsunami.
Sand and sediment debris	(i) Sand dunes were washed away and eroded (ii) Sand (black), gravel and shells were exposed (iii) Soils at various locations were salinized	Act as natural defence against wave and various sediment deposits were over-washed due to wave run-up
Water resources	(i) Contamination of water resources due to intrusion of saline water (ii) New inlets and water bodies were formed.	As they are fresh water natural resources, can't be avoided from the mixing of saline water into it

Another cause of fatalities includes collapsed structures, electric shocks, gas explosions, broken tanks, and floating debris. (Bernard and Meinig, 2011). The changes that may occurs include,

(i) Coastal alteration: Tsunamis can erode coastlines, remove sediments and alter the shape of the coastline. This erosion can affect habitats such as beaches, dunes, and coastal forests.

(ii) Habitat destruction: Coastal ecosystems, including mangroves, coral reefs and estuaries, can be severely damaged or destroyed by the force of a tsunami.

(iii) Salinity intrusion: Tsunamis can introduce saltwater into freshwater ecosystems, impacting rivers, lakes, and groundwater.

(iv) Soil contamination: Tsunamis can carry debris and pollutants inland, contaminating soils with saltwater and other substances. This can affect the fertility of agricultural lands, making it challenging for vegetation to grow.

(v) Loss of biodiversity: The destruction of habitats and ecosystems can lead to a loss of biodiversity. Many plants and animals may be unable to survive the sudden changes in their environment, and the disruption can have long-term consequences for the balance of local ecosystems.

(vi) Ocean pollution: Tsunamis can transport large amounts of debris, including hazardous materials, into the ocean. This can contribute to marine pollution and pose risks to marine life. The remains of buildings, infrastructure, and vehicles can introduce various pollutants to the land and ocean as well.

Indirect Impacts

The indirect impacts include water logging and contamination of drinking water leading to the spreading of various diseases in the tsunami-affected areas. Whenever water is stagnant and contaminated, infections and illnesses can spread quickly, increasing the number of fatalities. Sanitation systems (such as sewage, septic tanks, and toilets) as well as sites for disposing of solid waste and waste treatment services, especially in cities are also reported to have suffered significant damages. The most serious environmental issue is solid waste and disaster debris, which includes toxic and hazardous materials. Disposal and recycling of these wastes have been found critically important and that to in an environmentally appropriate manner. Immediate cleaning of the affected areas has also impacted environment because of inappropriate disposal approaches which includes exposed dumping and air burning (Srinivas, 2015).

PARAMETERS FOR ENVIRONMENTAL IMPACT ASSESSMENT

Geomorphic/landscape alteration

The strength of hills, cliffs, and elevated roads can also be weakened by the tremendous velocity of tsunami waves. Even though these buildings may not fall down instantly,

they can still become unsafe and fragile that risks the areas surrounding them. The long period of the tsunami, allows it to pass across barriers like gulfs, bays, and islands. Violent flooding arises from the sudden and rapid rise in water levels. A tsunami alters the terrain and can smash the shorelines. On land, erosion happens. Landforms can also have an impact on weather patterns. It influences the environment by affecting the rate of evaporation and wind, resulting in variations in precipitation, humidity, and temperature in a given location. Moreover, landforms cause rocks to erode away. Water penetrates rock fissures during a tsunami and freezes in cold weather. During warmer weather, it warms up before contracting and expanding, causing forces strong enough to crush rocks. Weathered rock can also be eroded. The base of a tsunami wave changes the morphology of the seabed. It sweeps away seabed sediments, destroying the seafloor environment. Generally, the invertebrates such as worms, snails and crustaceans that burrow into and mix seabed sediments. Sometimes a big piece of the sea floor is ripped up. The 2011 Japan tsunami deposited bottom sediments that were washed away in various locations, forming massive seafloor sand dunes.

Soil and sediment

A tsunami can contaminate the soil in coastal areas with the saline water. Sediments of different sizes can also be deposited to inland coastal areas after a tsunami.

Surface and ground water

Flooding and pollution of fresh water might lead to the spread of illness in impacted areas. For example, malaria may develop due to water logging and pollution after a tsunami event. Furthermore, it is difficult for people to remain safe and healthy under these circumstances and diseases to be cured efficiently. This allows for the easy transmission of such diseases and infections. Tsunami waves and retreating water destroys structures in the inundated area. The seawater wipes away the places closer to the beach. This affects infrastructure, such as sewerage, and contaminates drinking water. Seawater deposited salts into reservoirs, aquifers, lakes and streams after a tsunami event.

Natural vegetation

The tsunami may have a disastrous impact on coral reefs. The power of the tsunami wave alone can demolish the coral reefs. As the wave returns to the sea, it will carry a large amounts of debris like trees, automobiles, furniture, other households, concrete containers, dirt, muds and so on. These huge materials would strike the reefs again, killing the fragile coral reefs.

Agriculture

Tsunamis can cause salt injuries to crops. The accumulated salts harm the crop by reducing their ability to absorb the nutrients and water. As a result, farmlands cannot be utilized to cultivate crops for an extended period of time, causing long-term environmental damage. Food production is critical to humanity's existence in the environment, and tsunami-caused landforms can have an impact on food production. Furthermore, topography alter sunlight, water, and soil, making agriculture challenging.

Wildlife

Tsunamis not only claim human lives, but also have a terrible impact on animals. Tsunamis uproot trees, resulting in many animals dying tragically under fallen trees. It also disrupts animal habitats by uprooting trees in forests. Drowning kills land species, but pollution from harmful materials or chemicals dumped into the sea hence, poisoning the marine environment.

Human resource

One of the most devastating consequences of a tsunami is death, as escaping is nearly impossible. Tsunamis provide little or no notice before striking the land. As the flood move towards the shore, man has less time to escape. Persons living in coastal areas like towns, villages do not have time to devise an escape strategy. The enormous power of the tsunami causes quick death, most commonly by drowning. Other causes of mortality include structures collapse, gas explosions, electrocution, floating debris, and ruptured tanks. A tsunami can create radioactivity by destroying nuclear reactors, for example in March 2011, Japan's Fukushima nuclear plant got washed away, causing a significant environmental risk. The catastrophe polluted a vast area with radioactive substance, necessitating widespread long-lasting evacuations. Because radiation may survive for a long period, it has the potential to cause destruction on everything exposed to it. Furthermore, it is more hazardous to people and animals since the loss of electrons by molecules changes DNA structure causing birth abnormalities and cancer or even death.

Infrastructures

During tsunamis, the destruction of bridges, buildings, and other structures generate a significant amount of garbage. These wastes contain a huge amount of minerals, toxic compounds, and building materials. These poisonous compounds and dangerous materials may accidently combine with regular debris. These includes petroleum fuels, asbestos,

chemicals and industrial raw materials. Fast cleanup of impacted areas might result in improper disposal practices such as open dumping and air burning in turn producing air pollution. Chemical containers, and pipes, can be destroyed by tsunamis contaminating the surrounding with oil, asbestos, raw sewage, dioxides, and other poisonous substances. Also, when these poisonous substances are washed away into the oceans, they kill a large number of marine species, destroying the aquatic life.

REGIONAL AND GLOBAL ENVIRONMENTAL IMPACTS

Southeast Asia

Huge tsunami devastation is observed in Sri Lanka, Southeast Asia and East Africa in December 2004 that killed approximately 31,000 people and 23,000 people were injured (Bernard and Meinig, 2011). Seawater inundated coastal communities, damaged buildings, including drinking water supplies and sewage systems. Ghobaraha et al. (2006) undertook field research over Thailand and Indonesian districts, where large damage is reported due to the earthquake, followed by tsunami that struck Southeast Asia on December 26, 2004. They assessed how this incidence affected the buildings, bridges, and infrastructure. Critical infrastructure failures hampered the rescue operations and relief process, including those in hospitals, bridges, docks in harbors and communication systems adding to the suffering of the survivors. Necessity to build vital infrastructures that can withstand the impacts of a tsunami was inferred. Ghobaraha et al. (2006) came to the conclusion that many designed structures in Banda Aceh, Indonesia, suffered major damage and collapse as a result of earthquake based on the primary evaluation of the effects of the earthquake and tsunami on infrastructure and buildings.

Over 200 kilometres of the Sumatra coast in Aceh were submerged by the tsunami wave in 2004 and almost all constructed areas up to 3 km inland were destroyed in few areas. Along the east coast of mainland India and the Andaman Islands, the inundation ranged from 1 to 2 km. The tsunami waves were able to go farther inland due to co-seismic subsidence along the Sumatra coastline. This resulted in more destruction and flooding. Local uplift during the earthquake reduced the intensity of tsunami inundation on the outlying islands (Narayana, 2011). The morphometry and dispersal of offshore boulders are studied using side-scan sonar data from the close-shore areas. Findings indicates that the waves of tsunami increase bed shear velocities over threshold levels which is required for the continental shelf's coarse sands to entrain. The majority of the sediments (fine sands to coral boulders) that were deposited on land came from offshore regions. The tsunami damaged all offshore rocky outcrops (Paris et al., 2007).

Cochard et al. (2008) studied catastrophic damages in South East Asia. The impact on coastal vegetation in badly devastated areas of Banda Aceh and Thailand was highlighted. It is challenging to assess the function of ecosystems in different places because the significant variations in the energy and speed of tsunami waves over various coastal sections have not been well studied. Mangroves and other vegetation possibly gave some protection against the 2004 Indian ocean tsunami in a few areas (particularly far from the source of the tsunami); in several other areas, however, vegetation offered no protection or may even have exacerbated the risk in some cases (either by directing water flows or by adding to flow debris). At Neill Island, extensive hydrogeological researches were conducted by Singh (2008). The findings were compared with previous observations. It was observed that the shell limestone aquifers in few locations have formed cracks as a result of the earthquake, and these gaps permitted speedy passage of seawater into the aquifer, resulting in a decrease of groundwater quality. The tsunami waves have brought seawater intrusion into the areas where the aquifer is at sea level. The majority of the portion in island has hard mudstone base, where the aquifers are located much above sea level, did not exhibit any changes in groundwater regime (Singh, 2008).

Eastern coast of India

Many studies have focused mainly on the loss of human life, damages to infrastructure (buildings, electric poles, roads, bridges, towers etc.) and inland inundation due to 2004 tsunami along some of the Indian east coast (Table 2). Based on satellite imagery taken before and after the tsunami, the damage on Car Nicobar Island was evaluated by Kumar et al. (2007). Study focused on the island's south-eastern regions where waves reached a maximum height of 15 m and a minimum of 0.7m at distances of 400 m and 368.58 m from the coast respectively. On the island, the distance up to which inundation occurred along the coast ranged from 295.87 m to 1202.57 m, while the run-up levels ranged from 2 m to 19 m. The majority of the residential, business, and infrastructure facilities have suffered a significant damage. 2.5 m and 1m sand has been deposited at the beaches of Arong and Aukchung, respectively. There have been reports of 0.75 m to 1.25 m of coastal subsidence close to Malacca Beach. The coasts of several other islands, including Car Nicobar, Aukchung, Kimus, and Malacca, were also altered and eroded.

Mukherjee et al. (2010) provided a broader perspective on coastal ecological study in other tsunami-affected nations of Asia including Sri Lanka, Indonesia, Thailand and the Maldives. They identified the gaps in the field of ecological research in India and highlighted the lessons learned from studies conducted in other tsunami-affected nations with offering of advice on the connections between science and politics needed for efficient management of the coastal zone.

Direct field research revealed that the majority of the plants in the tsunami-affected area had withered. Nearly all of the water bodies in the tsunami-affected area show severe contamination from salt water intrusion, according to a recent UNEP (2005) survey report. Significant salinity was present in surface and underground waters in the tsunami-inundated zones. The majority of the tsunami sediments are made up of fine to medium grain sands, and contain higher salt concentrations [Na^{+}, K^{+}, Ca^{+2}, Mg^{+2}, Cl^{-} and $(SO4)_2$] in the water-soluble fractions as well as Cd, Cu, Zn, and Pb within the bioavailable and exchangeable fractions. Contaminants have marine, litho-, and anthropogenic origins. High correlations between the salts Pb, Zn, and Cu are also found for the average particle size (pore size and porosity). Due to the morphology of the area, there is a risk of severe environmental hazards of toxins which can migrate into both ground waters and the food chain (Szczuciński et al., 2005). Senani (2004) in his study found that 12.1% of the Andaman Islands' land area is at high risk from a tsunami and the associated flood conditions. Although, this number may not seem concerning, but it is important to understand that over 300,000 people live on these islands and they are dependent only on the limited agricultural fields (majority of which are located in the areas prone to hazards). In addition to this, 86% of the islands entire geographic area is thought to be covered by forests, leaving only about 14% of them usable for agriculture and other human activities. Since the entire population is dependent on these small agricultural areas, there is a critical need to safeguard them and be well-prepared for any environmental consequences.

Szczucinski et al. (2006) have investigated the immediate and long-term environmental and geological effects of the tsunami that struck coast of Thailand on December 26, 2004. They discovered that the tsunami flooded the coastal region >1.5 km inland and >10 m above sea level causing coastal erosion mostly in the areas immediately adjacent to the shore, on beaches, at river mouths and on the peninsulas. Up to 0.5 m of silty and tsunami-deposited sand covered nearly the whole inundation zone, burying the prior soil. The inland waters were salinated and the tsunami deposits were richer in salts, bioavailable heavy metals and arsenic. Kain et al. (2015) used a worldwide data of tsunami deposit sites and textures gathered from published literature and freely available data to demonstrate an inverse relationship among the size of particles and sediment density, climatic parameters, and the distance to the source. Hansom et al. (2015) studied and suggested that high waves can have a significant effect on both sedimentary and rocky beaches, causing sediments or rocky boulders removed from the coast line to be carried and deposited some distant inland.

Large amounts of sediment are transported by Tsunamis and may leave signatures in the landscape that can be seen. Wave dynamics, sediment accessibility, and local environmental features all influence the shape and composition of inland tsunami deposits; the latter also affects deposit restoration (Szczuciński et al., 2006). Before the 2004 tsunami, nearly the whole inundated zone was surrounded by a layer of silt that is a few to up to tens of centimeters thick on top of the soils. High concentrations of salts and hazardous elements including As, Pb, Zn and Cu, Cd in traces are present in the sediments. Increased concentrations of these elements have been found in the rapidly soluble fraction. Under appropriate physicochemical conditions, these fractions are readily accessible to the eco-biological cycle and may go into the food chain (Szczuciński et al., 2005). When a tsunami strikes, sediments from various coastal regions with various grain sizes can be sorted and mixed in different ways, leaving behind a depositional impression (Bryant et al., 1991). The coastal habitats of India's southwest coast that have been impacted by tsunamis, have similar depositional characteristics and variances in particle size.

According to Smith et al. (2004), the tsunami deposits are essentially uniform and consist of a sheet of fine to medium grain sand that lays on top of a relatively coarser deposition at the bottom of the tsunami sedimentary sequences. Significant amounts of sediment deposits from the mid- to inner-shelf sections of the Indian southwest coast were carried landward by the 2004 tsunami. Additionally, it was shown that the sediments form sub-populations in a variety of sizes. The tsunami sediments that washed up on the beach and in the estuary is easily distinguishable from the sub-populations in the sand range. The bimodal features of tsunami deposits implies that sedimentation occurred quickly and the particles of various sizes settled down with each other with different rates.

Table 2. Loss of life and inland inundation due to Tsunami of December 2004 along some regions of the Indian east coast.

Year	*Place*	*Inland inundation (in meter)*	*Damage to infrastructure/buildings (up to distance from the dune line in meter)*	*Loss of human life*
2004	Pondicherry	240	22-33	107
	Karaikal	200	~200	484
	Cuddalore	370	-	606
	Nagore	860	132	~6629
	Samanthanpettai	150	9-51	-
	Nagapattinam	800	49	-
	Velankanni	320	75	~900

Kumea et al. (2009) assessed the electrical conductivity (EC) and soil pH before and after the 2004 tsunami in the Nagapattinam (Tamil Nadu, India). The groundwater EC was relatively high due to sea water intrusion. Rise in soil EC between 2004 and 2005 was comparable to the decline in soil EC between 2005 and 2006. The largest decrease in soil EC was 13.3 dSm^{-1}, with an average decrease of 4.58 dSm^{-1}. The mean soil EC was 0.98 dSm^{-1} prior to the tsunami. The mean soil EC was 5.6 dSm^{-1} post-tsunami. The pH of the soil varies from 6.9 to 8.6 before the tsunami, with a mean value of 7.6. After that it fluctuated between 7.0 to 8.4, with a mean value of 8.0 and then dropped to 7.7 in 2006. The pH of soil in 2007 ranged from 6.9 to 8.7 with an average of 7.8. These findings clearly demonstrated the tsunami's significant impact on soil pH and large-scale rise in EC.

The coast of Kerala experienced a topographically directed tsunami on the day of 2004 tsunami. The entire water column was subjected to extreme turbulent mixing, which suspended the sediments from the continental shelf and brought it to the estuary and seashore. As a result, the geomorphology and sediment properties of the beach and nearshore regions underwent significant modifications. These involved the erosion of canals and holes on the backshore and the creation of deposits of black sand along the whole coastal zone. Estuarine sediments were slightly separated upstream, but nearshore sediments were mostly poorly separated. The characteristics of the sediment shows that a tsunami caused a significant interchange of constituents from shelves and shoreline areas to beaches and estuaries. (Narayana et al., 2007).

As the tsunami wave inundate and retreat an area, the effect it had on the quality of the groundwater was unforeseen. There is proof that the inundation after a tsunami contaminated groundwater resource by locally increasing salinity from acceptable levels up to 13,000 mS/cm (nearly ¼ of the salinity of seawater). And within a month, the salinity reached at its peak as the saline water infiltrates. Salinization remained in the affected coastal areas which was defined by the half-run-up distance of the tsunami, for more than ten months. A second salinity surge was then noticed during the succeeding monsoon season. Recharge from the semi-annual monsoons has a significant effect on the amount and frequency of natural attenuation of the saline groundwater. The consequences of the tsunami destruction indicate the vulnerability of the water resources in this subsistence population, which is concentrated within 500 meters of the coast (Violette et al., 2009). Violette et al. (2009) has also reported that the groundwater regime, which is the only source of fresh water, has been degraded at many places on the Andaman and Nicobar Islands.

By examining salinity and sodicity indices, Chandrasekharan et al. (2008) found that the tsunami had a detrimental effect on the soil and groundwater quality in the agricultural areas around the coastal Tamil Nadu. The pre-Tsunami EC and pH data of the soil and groundwater were compared to the post-Tsunami period EC and pH data. This finding indicates that the soil quality was approaching that of the pre-tsunami condition (EC-1.5 dSm-1; pH-8), six months after the tsunami, while the groundwater quality continued to be extremely saline and unsuitable for irrigation and drinking purpose. The groundwater salinity returned to its pre-tsunami levels by year 2006. The results suggest that rainfall quickly removed the salt accumulated by ocean water and the vegetation recovered quickly after the tsunami since it damaged the marine habitats during both its initial surge and its following backwash, which must have transported the deposits and other remains from land. Assuming this as a significant impact, Satheesh and Wesley (2009) evaluated tsunami-induced impacts to coastal ecosystems. The objective was to assess the effects of the tsunami on a few parameters of hydrobiology along the coast of Kudankulam using data taken before and after the tsunami. Salinity, sea surface temperature (SST), dissolved oxygen concentrations, pH, phosphate, nitrite, nitrate and the density of zooplankton and phytoplankton are the parameters of

hydrobiology which were used. Sedimentation through runoff and the mixing of beach silt, sand and organic matter are two important indirect effects of the tsunami on coastal ecosystems. According to Reddy et al. (2005), a significant increase in the amount of nutrients in the seashore waters of Dakshin Kannada (on India's western coast) were observed after the tsunami. The concentration of nitrates and nitrites also reached a record high value after a tsunami. Enhanced nutrient influx may promote algal bloom thar lowers the visibility of light underwater, which can deplete oxygen. The evaluation of the quality of water revealed that the tsunami had a significant impact on the nutrient concentrations and phytoplankton population. The concentrations of the above-mentioned nutrients (phosphate, nitrite and nitrate) with the zooplankton and phytoplankton were observed to have variations which is statistically significant. Biodiversity of a region may be affected by a change in the physico-chemical characteristics of the nearshore waters. Because of the fluctuations in their concentration, nutrients (phosphate, nitrite and nitrate) play a crucial role in the coastal environment through various inputs and biogeochemical processes. Laluraj et al. (2007) also noted a considerable rise in the concentration of phosphate and nitrate in the Cochin Estuary along western coast of India. The refill of nitrate from the surficial biogenic silt may be the cause of the elevated levels of nitrite and nitrate post-tsunami. The turbulence due to waves may encourage the quick mixing of surface and subsurface waters, which may be associated with the elevated levels of nitrate and nitrite. Ramachandran et al. (2005) observed that the concentrations of suspended silt have significantly increased along the Andhra and Tamil Nadu coasts in addition to the Andaman Nicobar Islands in post-tsunami scenarios. Another cause for the elevated levels of nutrients may be because the sediments and debris remain were carried back by the tsunami waves. Altaff et al. (2005) observed a higher amount of dissolved oxygen in coastal waters of Chennai (along eastern coast of India) after the tsunami. And then the dissolved oxygen levels declined gradually. Dissolved oxygen levels in coastal waters were primarily influenced by wind-induced turbulence, sewage addition and phytoplankton blooms. It is possible that the microbial oxygen demand for the breakdown of suspended biological and other inorganic debris is the cause of lower values of dissolved oxygen.

Western coast of India

Numerous scientific investigations have been conducted throughout India's west coast in relation to the Makran tsunami case in 1945. These include numerical modeling, tsunami wave parameters, mechanisms involved and effects along the Indian coast. Nayak (2002) explained how the coastal zone is dynamic and continues to be altered by both natural and man-made processes. The difficulties in coastal management must deal with habitat degradation, coastal erosion, and proper site selection. The presence of accurate and up-to-date data on coastal ecosystems, coastline processes, and quality of water is amongst the key criteria for coastal zone management. Recent developments in numerical modeling, GIS techniques, and remote sensing have been proved to be significant enough that any relevant interpretation is possible if employed consistently and sensibly (Tsunami Warning Centre Reference Guide, 2011). There are a number of recent studies that effectively incorporated several factors to determine maximum hazard and to find counter measures using geospatial techniques (Senani, 2004). The remote sensing data can be very useful information while dealing with, land use and changes near coastal areas, deposition at coasts, erosion of coastal areas, coral reefs, mangroves, state of wetlands, delimitation of high and low tide and developments like building constructions etc. The majority of structural collapses and failures may be due to poor construction, non-ductile details and inappropriate design. Buildings that were well-designed and built properly faced little or less structural damage even in the case when wave heights of tsunami go up to 12 meters. Infrastructure and buildings can be carefully planned and designed to safely withstand the forceful impacts produced by a tsunami.

Makran Subduction Zone (MSZ) can create great earthquake like that in 1945 Makran tsunami affecting the coast of Makran, Pakistan (Mokhtari and Farahbod, 2005; Pararas-Carayannis, 2005, 2006). This earthquake generated a huge catastrophic tsunami in the Northern Arabian Sea severely damaging the entire India's western coastline also along with Iran and Oman. The tsunami waves in Makran region (Pakistan) peaked at a height of around 13 meters. Its waves devastated fishing communities and severely damaged port infrastructures at various locations. The impact of the earthquake and the tsunami collectively claimed above 4,000 lives; however, the tsunami was mostly responsible (Patel et al., 2010, 2013). Karachi was also struck by waves of about 6.5 feet in height. The waves destroyed and killed all the people at Khudi, Pakistan (Shahid, 2005). A tsunami wave of height of 11.0 to 11.5 m struck the Kachchh region of Gujarat along the west coast of India. Since, Gujarat state alone has the longest coastline in India of about 1600 km, it is highly vulnerable to many catastrophic oceans related natural hazards and disasters including the earthquake and tsunami which have a long historical record. A large-scale destruction and loss of human lives were observed. The tsunami reached

near Mumbai at Bombay Harbor, Versova (Andheri, Mumbai), Haji Ali (Mahalaxmi, Mumbai), Juhu (Ville Parle) and Danda (Khar). The height of the tsunami wave was around 2 meters. No damage was reported at Bombay Harbor. Around 15 people died collectively at Versova, Haji Ali, Danda and Juhu (Pararas-Carayannis, 2005).

LEGISLATIONS AND REGULATIONS RELATED TO TSUNAMI IN INDIA

Disaster Management Act, 2005

The Disaster Management Act provides a comprehensive lawful framework for disaster management in India. It creates the National Disaster Management Authority (NDMA) countrywide, State Disaster Management Authorities (SDMAs) at the state level, and District Disaster Management Authorities (DDMAs) at the regional/district level. These authorities are responsible for formulating guidelines, plans and policies related to disaster management, including tsunamis. Promoting an anticipatory strategy to disaster management with a focus on readiness, prevention, mitigation, response, and recovery are the main goals. The Act defines the responsibilities and duties of different stakeholders, such as government and non-governmental organizations (NGOs), local governments, and community-based organizations (CBOs) in disaster management activities

National Disaster Management Plan (NDMP)

Under the Disaster Management Act, the NDMA is mandated to formulate the National Disaster Management Plan. The NDMP includes guidelines and strategies for managing various types of disasters, including tsunamis. It outlines the duties and responsibilities of different stakeholders, preparedness measures, early warning systems, evacuation plans, preparedness, response and post-disaster recovery efforts before, during, and after disasters. It incorporates inputs from relevant ministries, departments, agencies, and stakeholders involved in disaster management. For tsunamis, the NDMP may include provisions for establishing and maintaining early warning systems, such as the National Tsunami Early Warning Centre (NTEWC) under the Indian National Centre for Ocean Information Services (INCOIS) with following objectives:

(i) Conducting risk assessments to identify tsunami-prone areas, vulnerable communities, critical infrastructure and lifeline systems.

(ii) Developing and implementing evacuation plans, including the identification of safe shelters, evacuation routes and communication strategies.

(iii) Strengthening coastal resilience by using strategies including ecosystem-based methods, land use planning, and coastal zone management.

(iv) Enhancing community awareness, preparedness, and capacity-building initiatives through education, training and public outreach programs.

Coastal Regulation Zone (CRZ) Notification

The Coastal Regulation Zone Notification, issued under the Environmental Protection Act (1986), regulates activities along the coastal areas of India to protect the coastal environment and minimize risks from natural hazards including tsunamis. It specifies restrictions on construction, development and industrial activities within designated coastal zones. The Coastal Regulation Zone (CRZ) Notification, first issued in 1991 under the Environmental Protection Act (1986), regulates activities along the coastal areas of India to protect the coastal environment, promote sustainable development and minimize risks from natural hazards including tsunamis. The CRZ Notification categorizes coastal areas into different zones based on their ecological sensitivity and vulnerability to hazards. It specifies restrictions on developmental activities within each zone to prevent environmental degradation and reduce vulnerability to coastal hazards. Development projects within the CRZ require prior clearance from the Coastal Zone Management Authority (CZMA) or the National Coastal Zone Management Authority (NCZMA), depending on the extent of the project's impact on coastal areas. The CRZ Notification aims to balance developmental interests with environmental conservation and risk reduction objectives, thereby contributing to the resilience of coastal communities to tsunamis and other natural hazards.

National Tsunami Early Warning Centre (NTEWC)

India has established the NTEWC under the Indian National Centre for Ocean Information Services (INCOIS). While there may not be specific legislation governing the NTEWC, its operations are guided by government policies and funding allocations for tsunami monitoring, early warning dissemination and public awareness programs. NTEWC was constituted to monitor and provide timely warnings for tsunamis covering the Indian Ocean region. The NTEWC utilizes real-time data from a network of seismic sensors, sea level gauges and oceanographic buoys to detect and analyses tsunami-generating earthquakes and sea level anomalies. Upon detecting a potential tsunami threat the NTEWC issues warnings to relevant authorities, coastal communities and other stakeholders through various communication channels

including mass media, sirens and mobile phone alerts. The NTEWC also collaborates with regional and international tsunami warning systems, such as the Pacific Tsunami Warning Centre (PTWC) and the Indonesian Tsunami Early Warning System (InaTEWS) in order to enhance coordination and information sharing for effective tsunami risk management.

In addition to national-level legislation and regulations, some coastal states in India may have their own specific laws, policies or guidelines addressing tsunamis and coastal hazards. These state-specific regulations may fit with the principal outlines given by the Disaster Management Act and other national policies taking into account local context, vulnerabilities and priorities. State governments may enact legislation or issue executive orders related to land use planning, construction standards for coastal infrastructure, evacuation procedures and community-based disaster risk reduction initiatives tailored to the needs of coastal communities. For example, states like Tamil Nadu, Andhra Pradesh and Kerala, which are highly vulnerable to tsunamis may have specific guidelines for coastal zone management, disaster preparedness and response measures.

Damage recovery

Kumea et al. (2009) discussed the implications of tsunami on soil, groundwater, and vegetation as well as their post-event recovery. It was observed that the soil and groundwater of coastal areas became salinized as a result of sea water inundation, also caused salt injury to crops. Satellite images revealed the retrieval of rice fields at Nagapattinam district which is around 60% of the total agricultural crop after the tsunami event. Even though some studies in Thailand, Sri Lanka, and Neill Island identified qualitative impact to crops and land use, none of these studies took into account the quantitative recovery of vegetation. As a result, it's crucial to keep an eye on both the recovery of the soil and groundwater as well as the vegetation from salinization. The vegetation destroyed by the 2004 tsunami, returned to its earlier condition by the next 2-3 months which is evident from the NDVI readings taken before and after the disaster. It is possible that the cumulative impact of the death of crops, ocean water invasion and sediment deposits were the primary causes of the initial decline of vegetation. Satellite data collected before and after the 2004 tsunami event were studied to understand recovery. Many other researchers also studied the same pattern in order to assess the impact of salinity on vegetative development and its association with monsoonal rainfalls. 16-day composites of NDVI data with a 250 m spatial resolution (MODQ13 V004) taken from January 2004 to December 2006, were examined by Kumea et al. (2009). They reported that the small increase (which can be seen in Figure 1) was noticed in January 2005 that was possibly because of the retreating of seawater and the clean-up of the tsunami sediments. Moreover, other studies have shown that there is no relationship between vegetation cover and inundation (FERAL/WWF/Green coast project, unpublished data, 2005). The tsunami not only had a significant impact on the environment, but it also demonstrated the need to strengthen the capacity of national and state environmental authorities to respond to emergencies during disasters and the environmental damage they cause. Integrated environmental management, systematic environmental assessment, and coastal zone planning are a few domains that call for significant capacity building. The added duties associated with disaster recovery and relief planning and evaluation, along with the loss of employees, buildings, and equipment as a result of the tsunami, made the above-mentioned need evident. Many strategies, including public awareness campaigns, understanding of risks and vulnerabilities, community preparedness initiatives, early warning systems, evacuation plans, future land use planning, environmental preservation, and construction regulations, can be used to reduce the potential future risk of disasters. Governments and communities may assist individuals become more resilient to risks, reducing the risk of catastrophes.

FUTURE RISK PREPAREDNESS

Although there is no way to stop tsunamis, their consequences can be mitigated by public awareness campaigns, early warning systems, effective time frames for response, community and emergency preparation. Perhaps the first best or only sign that a tsunami is approaching is a natural tsunami warning. Strong or continuous earthquakes, an audible roar from the water (like a train or an aircraft) and unusual oceanic activity are examples of such natural tsunami warnings. The ocean may seem like a wall of water or a fast-approaching water wave. On the other hand, it might drain suddenly showing ocean floor, fishes and coral reefs as an extremely low tide. Even one of these alerts suggests that a tsunami may arrive in a few minutes. Additional strategies for mitigating the potential effects of a tsunami can include, (i) improving the paths for evacuation, (ii) constructing buildings for tsunami evacuation, (iii) restricting new building in places at a high risk of tsunamis. (iv) developing, placing, and building structures to lessen the damage caused by tsunamis, (v) developing rules for construction to mitigate the impact of tsunamis, (vi) maintaining and strengthening current infrastructure and buildings that might seriously impair response and recovery if damaged,

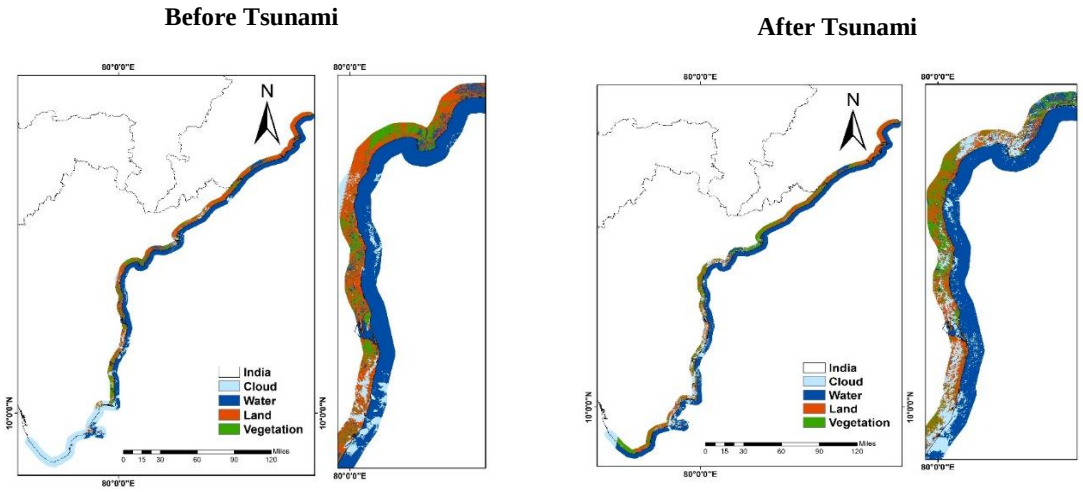

Figure 1. A view of the classification of coastal ecosystems along eastern coast inland buffer from the coastline before and after the 2004 Indian Ocean Tsunami.

(vii) relocating vulnerable individuals and vital community assets from tsunami-prone locations and (viii) making Post-Tsunami Recovery Plans.

Effective control of natural disasters demands worldwide collaboration across boundaries. There are few governmental efforts also which accounts for preparedness. Such as ITEWC has organized frequent workshops, trainings, and seminars to raise tsunami awareness among stakeholders. To evaluate the efficiency of communication links and the preparedness to handle emergency situations ITEWC, INCOIS frequently conducts communication trials and mock simulations. The Intergovernmental Oceanographic Commission (IOC) of UNESCO created the community performance-based initiative known as "Tsunami Ready" to improve preparedness by active engagement of the general public, leaders in the community and national and local disaster management agencies/authorities. The principal objectives of this program are to enhance the resilience of coastal communities to deal with tsunami calamities, minimize the loss of lives and assets and maintain a systematic and organized approach to community preparedness. This is accomplished by meeting the best-practice indicators set by UNESCO's Intergovernmental Coordination Group for the Indian Ocean Tsunami Warning and Mitigation System (ICG/IOTWMS) [ITEWS-INCOIS(https://tsunami.incois.gov.in/TEWS/abouttsunamiready)]. According to regional rules, every community must meet 11 key markers to be considered Tsunami Ready listed below:

(i) The Community Tsunami Risk Reduction Plan should be ready.

(ii) Tsunami inundation zones have been designated and plotted.

(iii) Provide a public display of tsunami information.

(iv) Create simply understandable tsunami maps for evacuation as defined by local authorities in consultation with local publics.

(v) Produce and distribute materials for public education and outreach programs.

(vi) Every year, conduct three or more outreach or educational programs.

(vii) Organize a yearly tsunami rehearsal in your local area.

(viii) In the community's Emergency Operations Plan (EOP), address concerns regarding earthquakes and tsunamis.

(ix) Design an Emergency Operations Center (EOC) during the aftermath of a tsunami.

(x) Support and assist the Emergency Operations Centre (EOC) during a tsunami disaster, if it is open and operational.

(xi) Establish a reliable method for a 24-hour warning point and/or EOC to send official tsunami alerts to the public.

To run and regulate the Tsunami Ready and IOWave activities in India, the Ministry of Earth Sciences constructed a National Board chaired by the Director of INCOIS, with members selected from the Ministry of Earth Sciences (MoES), National Disaster Management Authority (NDMA), Ministry of Home Affairs (MHA), Odisha State Disaster Management Authority (OSDMA), Andaman and Nicobar Islands Directorate of Disaster Management (DDM), and INCOIS.

CONCLUSIONS

Based on the available literatures, it can be concluded that few work has been done so far focusing especially on the impacts of tsunami on the environment and on the understanding of vulnerability of the coastal regions of India for the impacts of tsunami (due to tsunamigenic sources). Some studies on the eastern coast of India are available after December 2004 Indian Ocean tsunami while very few studies have been done regarding environmental impacts due to tsunami along the west coast of India. Therefore, it is needed to study various aspects of impacts on the environment due to tsunami along coastal and near coastal areas extensively. The present study brought out to the gap in the studies, thereof to the importance and scope of future works that can be done related with the tsunami and its impacts on environment due to tsunamigenic sources along coasts of India. As evident from the previous sections of the paper, natural hazards like tsunami can be a source of serious to devastating threats to various features of the environment. Very few information is available online on physical or biological parameters of the environment on the Indian coast and very few baselines for environmental or ecological assessments. There are many anthropogenic threats after a tsunami such as coastal pollution, resource overuse, beach erosion and landscape transformation. Study also found an important need for a more pronounced understanding of impacts of the tsunami, which tend to be extremely variable depending on the currency used to assess it, as well as the measures used to quantify such impact. A better understanding of impact will play a major role in determining coastal management and strategic policy.

Acknowledgments

Rajeev Bhatla acknowledges the receipt of the IOE grant under Dev. Scheme No. 6031(A). Babita Dani would like to thank funding support from the University Grants Commission, New Delhi, in the form of Senior Research Fellowship.

Author Credit Statement

Babita Dani: Conceptualization, design and writing paper; Rajeev Bhatla: Conceptualization and supervision; Vaibhava Srivastava: Supervision and improvements in the draft manuscript; A. P. Singh: Improvements in the draft manuscript. All authors read and approved the final manuscript

Data Availability

The dataset analyzed during the present study is available in the data repository of NASA (LANDSAT 5-USGS). All other data used, appear and discussed in the submitted manuscript

Compliance with Ethical Standards

The authors declare no conflict of interest and adhere to copyright norms

References

Altaff, K., Sugumaran, J. and Naveed, S., 2005. Impact of tsunami on meiofauna of Marina beach, Chennai, India. Curr. Sci., 89, 34–38.

Bernard, E. N. and Meinig, C., 2011. History and Future of Deep-Ocean Tsunami Measurements. DOI: 10.23919/OCEANS.2011.6106894.

Bryant, E. A.1991. Natural Hazards:Melbourne, Cambridge U niversity Press, 294 p.

Chandrasekharan, H., Sarangi, A., Nagarajan, M., Singh, V. P., Rao, D. U. M., Stalinc, P., Natarajan, K., Chandrasekharan, B. and Anbazhagan, S., 2008. Variability of soil-water quality due to Tsunami-2004 in the coastal belt of Nagapattinam district, Tamilnadu. J. Environ. Manag., 89, 63-72.

Cochard, R., Ranamukhaarachchi, S. L., Shivakoti, G. P., Shipin, O. V., Edwards, P. J. and Seeland, K. T., 2008. The 2004 tsunami in Aceh and Southern Thailand: a review on coastal ecosystems, wave hazards and vulnerability. Perspectives in Plant Ecol. Evol. Systematics, 10(1), 3-40.

Ghobaraha, A., Saatcioglu, M. and Nistor, I., 2006. The impact of the 26 December 2004 earthquake and tsunami on structures and infrastructure. Engineering structures, 28(2), 312-326.

Hansom, J. D., Switzer, A. D. and Pile, J., 2015. Extreme waves: causes, characteristics, and impact on coastal environments and society. In: Coastal and marine hazards, risks, and disasters, pp. 307-334. Elsevier.

Kain, C. L., Gomez, C., Hart, D. E., Chagué-Goff, C. and Goff, J., 2015. Analysis of environmental controls on tsunami deposit texture. Marine Geol., 368, 1–14.

Kumar, A., Chingkhei, R. K. and Dolendro, T. H., 2007. Tsunami damage assessment: a case study in Car Nicobar Island, India. Int. J. Remote Sensing, 28(13–14), 2937–2959.

Kumea, T., Umetsu, C. and Palanisami K., 2009. Impact of the December 2004 tsunami on soil, groundwater and vegetation in the Nagapattinam district, India. J. Environ. Manag., 90, 3147-3154.

Laluraj, C. M., Kesavadas, V., Balachandran, K. K., Gerson, V. J., Martin, G. D., Shaiju, P. et al., 2007. Recovery of an estuary in the southwest coast of India from tsunami impacts. Environ. Monit. Assessment, 125(1–3), 41–45. doi:10.1007/s10661-006-9237-2.

Mokhtari, M. and Farahbod, A. M., 2005. Tsunami Occurrence in the Makran Region. Tsunami Seminar, Tehran, Vol. 26.

Mukherjee, N., Dahdouh-Guebas, F., Kapoor, V., Arthur, R., Koedam, N., Sridhar, A. and Shanker, K., 2010. From bathymetry to bioshields: a review of post-tsunami ecological research in India and its implications for policy. Environ. Manag., 46(3), 329-339.

Narayana, A. C., 2011. Tectonic geomorphology, tsunamis and environmental hazards: reference to Andaman-Nicobar

Islands. Nat. Hazards., 57, 65-82. doi: 10.1007/s11069-010-9647-x.

Narayana, A. C., Tatavarti, R., Shinu, N. and Subeer, A., 2007. Tsunami of December 26, 2004 on the southwest coast of India: Post-tsunami geomorphic and sediment characteristics. Marine Geol., 242, 155-168.

Nayak, S. 2002. Use of satellite data in coastal mapping. Indian Cartographer, CMMC-01, 147-157.

Pararas-Carayannis, G., 2005. The Great Earthquake and Tsunami of 26 December 2004 in Southeast Asia and the Indian Ocean. http://drgeorgepc.com/Tsunami2004 Indonesia.html.

Pararas-Carayannis, G. 2006. The potential of tsunami generation along the Makran Subduction Zone in the northern Arabian Sea: Case study: The earthquake and tsunami of November 28, 1945. Sci. Tsunami Hazards., 24(5), 358-384.

Paris, R., Lavigne, F., Wassmer, P. and Sartohadi, J., 2007. Coastal sedimentation associated with the December 26, 2004 tsunami in lhok nga, west banda aceh (sumatra, indonesia). Marine Geol., 238(1-4), 93-106.

Patel, V. M., Patel, H. S. and Singh, A. P., 2010. Tsunami propagation in Arabian Sea and its effect on Porbandar, Gujarat, India. J. Eng. Res., 1(2), 206-217.

Patel, V. M., Dholakia, M. B. and Singh, A.P., 2013. Tsunami Risk 3D Visualizations of Okha Coast, Gujarat (India). Int. J. Engineering Sci. Innovative Technology (IJESIT), 2(2),2319-5967.

Ramachandran, S., Anitha, S., Balamurugan, V., Dharanirajan, K., Vendhan, K. E., Divien, M. I. P., Vel, A. S., Hussain, I. S. and Udayaraj, A., 2005. Ecological impact of tsunami on Nicobar Islands (Camorta, Katchal, Nancowry and Trinkat). Curr. Sci., 89(1), 195-200.

Reddy, H. R. V., Katti, R. J., Raveesha, K. P., Vikas, S. J. and Nagendra Babu, K. S., 2005. Coastal water quality off Dakshina Kannada before and after tsunami. Curr. Sci., 88(7), 1027–1029.

Satheesh, S. and Wesley, S. G., 2009. Impact of December 26, 2004 tsunami on the hydrobiology of Kudankulam coast, Gulf of Mannar, India. Environ. Monit. Assess., 156(1), 131-139.

Senani, S., 2004. Analysis of land use, crop productivity in Andaman and Nicobar Islands, Central Agri-cultural Research Institute. Geospatial World, Map Asia.

Shahid, S., 2005. Tsunami disaster in South Asia. Pakistan J. Meteorol., 2(3), 3-9.

Shukla, S. B., Prizomwala, S. P., Ukey, V., Bhatt, N. and Chamyal, L. S., 2010. Coastal geomorphology and tsunami hazard scenario along the Kachchh coast, western India. Indian J. Geo-Marine Sci., 39 (4), 549-556.

Singh, V. S., 2008. Impact of the Earthquake and Tsunami of December 26, 2004, on the groundwater regime at Neill Island (south Andaman). J. Environ. Manag., 89, 58-62.

Singh, A. P., Murty, T. S., Rastogi, B. K. and Yadav, R. B. S., 2012. Earthquake Generated Tsunami in the Indian Ocean and Probable Vulnerability Assessment for the East Coast of India. Mar. Geod., 35, 49-65.

Smith, D. E., Shi, S., Cullingford, R. A., Dawson, A. G., Dawson, S., Firth, C. R. et al., 2004. The holocene storegga slide tsunami in the United Kingdom. Quat. Sci. Rev., 23(23-24), 2291-2321.

Srinivas, H., 2015. The Indian Ocean Tsunami and its Environmental Impacts. GDRC Research Output E-023. Kobe, Japan: Global Development Research Center. Retrieved from https://www.gdrc.org/uem/disasters/disenvi/tsunami.html.

Szczuciński, W., Chaimanee, N., Niedzielski, P., Rachlewicz, G., Saisuttichai, D., Tepsuwan, T., Lorenc, S. and Siepak, J., 2006. Environmental and Geological impacts of the 26 December 2004 Tsunami in Coastal Zone of Thailand-Overview of short and long-term effects. Polish J. of Environ. Stud., 15(5), 793-810.

Szczuciński, W., Niedzielski, P., Rachlewicz, G., Sobczyński, T., Zioła, A., Kowalski, A. et al., 2005. Contamination of tsunami sediments in a coastal zone inundated by the 26 December 2004 tsunami in Thailand. Environ. Geol., 49(2), 321-331.

Tsunami Warning Centre Reference Guide, Indian National Centre for Ocean Information Services (2011).

UNEP, 2005. United Nations Environment Programme 2005

Violette, S., Boulicot, G. and Gorelick, S. M., 2009. Tsunami-induced groundwater salinization in southeastern India. Comptes Rendus Geoscience., 341(4), 339-346

Received on: 01-09-2023 ; Revised on: 13-03-2024; Accepted on: 15-03-2024

OBITUARY

Prof. Bimla Buti (1933 – 2024)

With profound sadness, I wish to inform the Plasma Physics community that Prof. Bimla Buti, an internationally renowned plasma physicist and a face of Indian women scientists passed away on 24 February 2024 after a brief illness. For the past 4 years or so she was living with her niece Veena and Venkat (Veena's husband) Ramani in Ahmedabad. Both Veena and Venkat were not only taking good care of Prof. Buti but also helping her in the Buti Foundation activities. I met Prof. Buti last year in Ahmedabad and very excitedly she explained to me the new initiatives she was planning for the young scientists under Buti Foundation. Her death is a great loss not only to the family and friends but to the entire plasma physics community!

Bimla was born on 19 September 1933 in Multan, undivided India. Her parents were Bodh Raj and Jamuna Devi Buti. She had her education in Delhi, obtaining a Bachelor of Science (Honors) and a Master of Science degree in Physics from the University of Delhi. She got admission to the University of Chicago for doctoral studies and obtained a Ph.D. degree in plasma physics in 1962 under the supervision of Prof. S. Chandrasekhar, a noble laureate. She joined University of Delhi as a teaching faculty and taught for about 2 years. She went back to USA to work at Goddard Space Flight Center. She came back to India in 1968 and joined the Indian Institute of Technology Delhi (IIT Delhi). I was doing my Master in Physics at IIT Delhi at that time. Prof. Buti gave us one course on plasma physics. The whole class was impressed with her way of teaching and explaining the fundamentals of plasmas. This was my first interaction with Prof. Buti. I was fortunate to get my Ph.D. degree from IIT Delhi in 1972 under the supervision of Prof. Buti. She was not only an excellent guide, but an idol to whom I have

always looked up to for inspiration and motivation or when in despair! During the student era, I had a fair amount of despair, so much so that I even seriously thought of giving up PhD. At that crucial stage, Prof. Buti's sound and practical advise could bring me out of this and put me on track! My association with Prof. Buti is more than 50 years old. During this period, we have published more than 30 peer-reviewed papers either jointly or with other authors/coauthors.

Prof. Bimla Buti joined the Physical Research Laboratory (PRL) Ahmedabad as Associate Professor in 1971 at the invitation of Dr. Vikram Sarabhai, the then Director of PRL. She retired from PRL as Dean of Faculty in 1993. During her tenure at PRL, she established herself as a world leader in space plasma physics in the area of nonlinear plasma waves, solitons and chaos and plasma turbulence. After her retirement, she continued to carryout research in India and abroad. She spent four year at the Jet Propulsion Laboratory (JPL), Pasadena, CA after her retirement. Slowly her interest shifted to social and philanthropic work, and she founded Buti Foundation in 2003 to help the young scientists in their careers, and to promote awareness about healthcare and computer education among the young people and senior citizen. More details about the activities of Buti Foundation can be found at https://www.butifoundation.org/

Prof. Bimla Buti was a dedicated scientist and an excellent teacher. The research work done by her is of highest quality and brought her not only the worldwide recognition but many awards also. Prof. Buti was elected as the first Indian woman Physicist Fellow of the Indian National Science Academy (INSA) in 1981. She was Fellow of The Academy of Sciences of the Developing World (TWAS), The National Academy of Sciences (India) (NASI), and the American Physical Society (APS). She played a leading role in the formation of Plasma Science Society of India (PSSI) and served as its President during 1992-1993. She conducted several Spring Colleges on Plasma Physics at the Abdus Salam International Center for Theoretical Physics, Triest, as the course Director of Plasma Physics, during 1985-2003. These Spring Colleges helped the scientists from the developing countries to interact and establish contacts with the experts from the developing countries. To mention a few awards bestowed upon Prof. Bimla Buti: Vikram Sarabhai Award for Planetary Sciences (1977), INSA-Vainu Bappu Award for Astrophysics, 1994, US Medal for Fundamental Contributions in the Physics of Nonlinear Waves and Chaos (2010), NASI Prof. Megh Nad Saha Memorial Award (2013), NASI A.C. Banerji Memorial Award (2017) and IPA R.D. Birla Award (2020).

Prof. Bimla Buti did not marry but dedicated her entire life to science and social work. She inculcated the values of hard work, perseverance, and commitment to science in all her students. She was very independent in thoughts and actions. Even after her retirement, she lived alone in New Delhi and carried out Buti Foundation's activity. She moved to Ahmedabad during Corona virus epidemic.

Prof. Bimla Buti will be remembered not only as a great plasma scientist but also as a wonderful human being! Her scientific and social work will be a source of inspiration to the present young generation. We pray to God to grant peace to her soul!

Gurbax Singh Lakhina
Former Director, Indian Institute of Geomagnetism, Navi Mumbai

GUIDE FOR AUTHORS

The Journal of Indian Geophysical Union (JIGU), published bimonthly by the Indian Geophysical Union (IGU), is an inter disciplinary journal from India that publishes high-quality research in earth sciences with special emphasis on the topics pertaining to the Indian subcontinent and the surrounding Indian Ocean region. The journal covers several scientific disciplines related to the Earth sciences such as solid Earth geophysics, geology and geochemistry, apart from marine, atmosphere space and planetary sciences. J-IGU welcomes contributions under the following categories:

*Research articles, short notes and students section reporting new findings, results, etc.

*Review articles providing comprehensive overview of a significant research field.

In addition, JIGU also welcomes short communications, after communications and report on scientific activity, book reviews, news and views, etc.

The manuscript should be submitted electronically as a single word format (.doc file) including the main text, figures, tables, and any other supplementary information along with the signed "Declaration Letter". The manuscript should be submitted by email (jigul1963@ gmail.com) to the Chief Editor.

After acceptance of the manuscript the corresponding author would be required to submit all source files (text and Tables in word format) and figure in high resolution standard (*.jpg, *.tiff, *.bmp) format. These files may be submitted to JIGU as a single *.zip file along with the "Copyright Transfer Statement".

IMPORTANT INFORMATION

Ethics in publishing; J-IGU is committed to ensuring ethics in publication and takes a serious view of plagiarism including self-plagiarism in manuscripts submitted to the journal, Authors are advised to ensure ethical values by submitting only their original work and due acknowledgement to the work of others used in the manuscript. Authors must also refrain from submitting the same manuscript to more than one journal concurrently, or publish the same piece of research work in more than one journal, which is unethical and unacceptable. Editor of JIGU is committed to make every reasonable effort to investigate any allegations of plagiarism brought to his attention, as well as instances that come up during the peer review process and has full authority to retract any plagiarized publication from the journal and take appropriate action against such authors if it is proven that such a misconduct was intentional.

Similarly, Editor and Reviewers are also expected to follow ethical norms of publishing by ensuring that they don't use any unpublished information, communicated to them for editorial or review purpose, in their own research without the explicit written consent of the author. They are also expected to keep manuscript' data/ observations/ any other information related to the peer review confidential to protect the interest of the authors. Reviewers should refrain from reviewing the manuscripts in which they have conflicts of interest resulting from competitive, collaborative, or other relationships or connections with any of the authors, companies, or institutions connected to the manuscript.

Conflict of interest

All authors are requested to disclose any actual or potential conflict of interest including any financial, personal or other relationships with other people or organizations within three years of beginning the submitted nor that could inappropriately influence, or be perceived to influence, their work.

Submission declaration

Submission of a manuscript implies that the work has not been published previously and it is not under consideration for publication elsewhere, and that if accepted it will not be published elsewhere in the same or any other form, in English or in any other language, without the written consent of the publishers. It also implies that the authors have taken necessary approval from the competent authority of the institute/organization where the work was carried out.

Copyright

After acceptance of the manuscript the corresponding author would be required to sign and submit the "Copyright Transfer Statement".

MANUSCRIPT PREPARATION

The corresponding author should be identified (include E-mail address, Phone/Mobile number). Full affiliation and postal address must be given for all co-authors.

Abstract:

An abstract of not more than 300 words must be included.

Text:

The manuscript should be structured to include a front page containing the title, Author(s) name, affiliation and address of the institute, where the work was carried out, and 5-to-6 Key words. Author(s) present address, if different from the above mentioned address, may be given in the footnote. The corresponding author should be identified with an asterisk and his/her email ID should be provided. This page should be followed by the main text consisting of Abstract, Introduction, Methods/ Techniques/ Area description, Results, Discussion, Conclusions, Acknowledgements, and References. Tables and Figures with captions should be inserted at the end of main text. It should not be inserted in the body of the text.

Figures/ Illustrations:

figures should be provided in camera-ready form, suitable for reproduction (which may include reduction) without retouching. Figures in high-resolution (at least 300 dpi) standard formats (*.jpg, * tiff, *.bmp) are acceptable. Figures should be numbered according to their sequence in the text. References should be made in the text to each figure. Each figure should have a suitable caption.

Tables:

Authors should take note of the limitations set by the size and layout of the journal. Table should not exceed the printed area of the page. They should be typed on separate sheets and details about the tables should be given in the text. Heading should be brief. Large tables should be avoided and may be provided as supplementary information, if required.

Equations:

Equations should be numbered sequentially with Arabic numerals and cited in the text. Subscripts and Superscripts should be set off clearly.

Equation writing software that presents each equation as an object in MS Word will be accepted. Style and convention adopted for the equations should be uniform throughout the paper.

References:

All references to publications cited in the main text should be presented as a list of references in order following the text and all references in the list must be cited in the text. References should be arranged chronologically, in the text. The list of references should be arranged alphabetically at the end of the paper.

References should be given in the following form:

Kaila, K.L., Reddy PR., Mall D.M., Venkateswarlu, N., Krishna V.G. and Prasad, A.S.S.S.R.S., 1992, Crustal structure of the west Bengal el eon deep seismic sounding investigations. Geophys. J. Int., 1,45-66.

REVIEW PROCESS:

All manuscripts submitted to the journal are peer-reviewed. It is advisable to send the contact details of 4 potential reviewers along with the manuscript to expedite the review process. Editor has the option to select reviewers from the list or choose different reviewers. The review process usually takes about 3 months. All enquiries regarding the manuscript may be addressed to the Chief Editor.

GALLEY PROOF:

Technical editing of manuscripts is performed by the editorial board. The author is asked to check the galley proof for typographical errors and to answer queries from the editor. Authors are requested to return the corrected proof within two days of its receipt to ensure uninterrupted proceedings The editor will not accept new material in proof unless permission from the editorial board has been obtained for the addition of a "note added in proof". Authors are liable to be charged for excessive alterations to galley proof.

PUBLICATION CHARGES:

There are no page charges for publication. The corresponding author will receive a soft copy (pdf format) of his/her published article. Should the author desire to purchase reprints of his/her publication, he/she must send the duly signed Reprint Order Form (accompanies the galley proof and contains price details) along with the corrected galley proof to the Editor. The reprint charges must be paid within one month of sending the Reprint Order Form.

Any payment related to printing or purchase of reprints should be made in the form of a Demand Draft in the name of Treasurer, Indian Geophysical Union, payable at Hyderabad.

You may download the pdf file from:
http://iguonline.in/journal/instructions.php